# MECHANICS AND MECHANISMS OF CREEP AND DUCTILE FRACTURE

Ankit Srivastava, B.Tech., M.S.

Dissertation Prepared for the Degree of

DOCTOR OF PHILOSOPHY

UNIVERSITY OF NORTH TEXAS

August 2013

APPROVED:

Alan Needleman, Major Professor
Srinivasan G. Srivilliputhur, Committee Member
Thomas Scharf, Committee Member
Zhenhai Xia, Committee Member
Zhiqiang Wang, Committee Member
Narendra Dahotre, Chair of the Department of Materials Science and Engineering
Costas Tsatsoulis, Dean of the College of Engineering
Mark Wardell, Dean of the Toulouse Graduate School

Srivastava, Ankit, Mechanics and mechanisms of creep and ductile fracture. Doctor of Philosophy (Materials Science and Engineering), August 2013, 154 pp., 3 tables, 72 figures, bibliography, 147 titles.

The main aim of this dissertation is to relate measurable and hopefully controllable features of a material's microstructure to its observed failure modes to provide a basis for designing better materials. The understanding of creep in materials used at high temperatures is of prime engineering importance. Single crystal Ni-based superalloys used in turbine aerofoils of jet engines are exposed to long dwell times at very high temperatures. In contrast to current theories, creep tests on Ni-based superalloy specimens have shown size dependent creep response termed as the thickness debit effect. To investigate the mechanism of the thickness debit effect, isothermal creep tests were performed on uncoated Ni-based single crystal superalloy sheet specimens with two thicknesses and under two test conditions: a low temperature high stress condition and a high temperature low stress condition. At the high temperature, surface oxidation induced microstructural changes near the free surface forming a layered microstructure. Finite element calculations showed that this layered microstructure gave rise to local changes in the stress state. The specimens also contained nonuniform distribution of initial voids formed during the solidification and homogenization processes. The experiments showed that porosity evolution could play a significant role in the thickness debit effect. This motivated a basic mechanics study of porosity evolution in single crystals subjected to creep for a range of stress states. The study was performed using three-dimensional finite deformation finite element analysis of unit cells containing a single initially spherical void in a single crystal matrix. The materials are

characterized by a rate-dependent crystal plasticity constitutive relation accounting for both primary and secondary creep. The effect of initial void spacing and creep exponent was also explored. Based on the experimental observations and results of finite element calculations a quantitative mechanistic model is proposed that can account for both bulk and surface damage effects and assess their relative roles in the observed thickness debit effect. Another set of calculations aim at relating the crack growth resistance and fracture surface morphology to material microstructure for ductile structural metals. The process that governs the ductile fracture of structural materials at room temperature is one of nucleation, growth and coalescence of micron scale voids, and involves large plastic deformations. Experimental studies have shown that fracture surfaces in a wide variety of materials and under a wide variety of loading conditions have remarkable scaling properties. For thirty years, the hope to relate the statistical characterization of fracture surfaces to a measure of a material's crack growth resistance has remained unfulfilled. Only recently has the capability been developed to calculate sufficient amounts of three dimensional ductile crack growth in heterogeneous microstructures to obtain a statistical characterization of the predicted fracture surfaces. This development has enabled the exploration of the relation of both fracture toughness and fracture surface statistics to material properties and microstructure when the fracture mechanism is one of void nucleation, growth and coalescence. The relation of both toughness and the statistical properties of fracture surfaces in calculations of heterogeneous microstructures to various microstructural features is discussed and a remarkable correlation between fracture surface roughness and fracture toughness is shown for the first time.

ACKNOWLEDGMENTS

I would like to express my sincere gratitude to Prof. Alan Needleman for providing me the opportunity to work with him, its a dream come true for me. His approach towards research has always inspired me and motivated me to learn more. The freedom that he gave me in pursuing my ideas during the course of my research work has helped me become a true student. His discourses on various aspects of mechanics and mathematics during our personal interactions will always help me think critically.

I would also like to thank Dr. Srinivasan G. Srivilliputhur who is a dynamic and caring teacher. I learned a lot about philosophy of life and research during our interactions. I am again thankful to Dr. Srinivasan G. Srivilliputhur together with Dr. Zhiqiang Wang, Dr. Thomas Scharf and Dr. Zhenhai Xia for serving on my committee.

In addition, a thank you to S. Gopagoni (a former UNT student now at Johns Manville, USA); Dr. V. Seetharaman and Dr. A. Staroselsky (Pratt & Whitney, USA); Dr. L. Ponson (CNRS, France); Dr. E. Bouchaud (ESPCI, France); Dr. V. Tvergaard (DTU, Denmark); Dr. R. Banerjee (UNT); and Dr. S. Osovski (UNT) for their invaluable help and support while carrying out some part of the work reported in this dissertation.

I would also take this opportunity to thank Dr. K.M. Prabhakaran and Mr. S.K. Sinha, from Bhabha Atomic Research Centre , Mumbai, India, for all their supports, encouragements and advices during my stay at BARC.

Furthermore I would also like to acknowledge with much appreciation the crucial role of the MTSE staffs Wendy Agnes and Joan Jolly in making my graduate student life easy by taking care of all the paper works.

I am also grateful for all the love, support and encouragement that I received from my family. I am deeply indebted to my parents who have always believed in me and encouraged me to put my best effort into all my endeavors. And last but not the least, I would like to thank all my friends without whom I would never have come so far in my life.

CONTENTS

LIST OF TABLES

LIST OF FIGURES

# CHAPTER 1

# INTRODUCTION

Engineers carefully optimize a design such that the device, plan or creation should perform its function without fail. Everything, however, eventually fails in some way to perform its given function. Failure of most of the engineering components especially the structural components can be well related to material failure. The optimistic solution to this problem is to choose a material that is resistant to all failure modes in all environmental conditions. Unfortunately such a material has not been discovered yet. Hence, the engineer must struggle to design in such a way as to avoid failure. As Leonardo da Vinci said that although nature commences with reason and ends in experience it is necessary for us to do the opposite, that is to commence with experience and from this to proceed to investigate the reason. Following this the main aim of this dissertation is to relate measurable and hopefully controllable features of a material's microstructure to its observed failure modes to provide a basis for designing better materials.

The failure of engineering materials can be attributed to many known and unknown factors. Furthermore there are a number of mechanisms and combinations of mechanisms that can cause failure. The specific failure mechanism or mechanisms indeed depend on material or microstructural defects, damage induced during manufacturing and assembly, and on conditions during storage and in use. In this dissertation the focus is confined on creep and ductile fracture of materials used for structural applications. Using both the methods of mechanics and material science few specific problems related to creep and ductile fracture of engineering materials are addressed. The topics addressed in this dissertation are briefly summarized in the following paragraphs. A detail introduction and background of the topic is provided in the beginning of each chapter.

The understanding of creep in materials used at high temperatures is of prime engineering importance. Single crystal Ni-based superalloys used in turbine aerofoils of jet engines are exposed to long dwell times at very high temperatures. Creep tests on Ni-based

single-crystal superalloy sheet specimens typically show greater creep strain rates and/or reduced strain or time to creep rupture for thinner specimens than predicted by current theories, which predict a size-independent creep strain rate and creep rupture strain. This size-dependent creep response is termed the thickness debit effect. To investigate the mechanism of the thickness debit effect, isothermal, constant nominal stress creep tests were performed on uncoated PWA1484 Ni-based single-crystal superalloy sheet specimens of thicknesses 3.18 and 0.51 mm under two test conditions: 760°C/758MPa and 982°C/248MPa. The microscopic analysis revealed that the specimens contained initial microvoids formed during the solidification and homogenization processes. For the specimens tested at 760°C/758MPa microscopic analyses revealed that the thick specimens exhibited a mixed failure mode of void growth and cleavage-like fracture while the predominant failure mode for the thin specimens is cleavage-like fracture. The creep specimens tested at 982°C/248MPa in air showed the development of surface oxides and a near-surface precipitate-free zone. Finite-element analysis revealed that the presence of the alumina layer at the free surface imposes a constraint that locally increases the stress triaxiality and changes the value of the Lode parameter (a measure of the third stress invariant). The surface cracks formed in the oxide layers are arrested by further oxidation; for a thickness of 3.18 mm the failure mode is void nucleation, growth and coalescence, whereas for a thickness of 0.51 mm there is a mixed mode of ductile and cleavage-like fracture.

In order to quantify the role of void growth in single crystals under creep loading conditions, three dimensional finite deformation finite element analyses of unit cells containing a single initially spherical void was carried out. The materials were characterized by a rate dependent crystal plasticity constitutive relation accounting for both primary and secondary creep. Two types of imposed loading were considered: an applied true stress (force/current area) that is time independent; and an applied nominal stress (force/initial area) that is time independent. Isothermal conditions were assumed. The evolution of porosity was calculated for various values of the stress triaxiality and of the Lode parameter. The evolution of porosity with time is sensitive to whether constant true stress or constant nominal stress loading

is applied. However, the evolution of porosity with the overall unit cell strain is insensitive to the mode of loading. At high values of stress triaxiality, the response is essentially independent of the value of the Lode parameter. At sufficiently low values of the stress triaxiality, the porosity evolution depends on the value of the Lode parameter and void collapse can occur. Also, rather large stress concentrations can develop which could play a role in the observed thickness dependence.

Following the observation that depending on the stress state the voids can either grow and coalesce or collapse and close up. A further investigation of the possible transition between void collapse for well separated voids to coalescence for sufficiently close voids in a nonlinearly viscous single crystal subject to creep loading is warranted. For a fixed value of stress triaxiality of 1/3 and three values of the Lode parameter 1, 0 and 1 three dimensional unit cell calculations were carried out for two initial void volume fractions and, for each initial void volume fraction, a range of void spacings. The materials were characterized by a rate power law viscous crystal plasticity constitutive relation and three values of the power law creep exponent were considered. The results show that, for sufficiently closely spaced voids, void coalescence occurs while for widely spaced voids void collapse can occur. Whether void coalescence, void collapse or neither occurs mainly depends on the value of the Lode parameter. The calculations also showed that as the void coalesces or collapses, a stress concentration develops which can then trigger cracking as seen in the experiments

Based on the experimental observations and detailed finite element calculations a mechanistic model for the observed thickness debit effect in the creep response of Ni-based single crystal super alloys is proposed. The phenomenological model is a nonlinear parallel spring model for uniaxial creep with springs representing the bulk and possible surface damage layers. The nonlinear spring constitutive relations model both material creep and evolving damage. The number of springs and the spring creep and damage parameters are based, as much as possible, on the experimental observations of thickness debit effect. The bulk damage mechanisms accounted for are the nucleation of cleavage-like cracks from preexisting voids and, at the higher temperature, void nucleation. The surface damage mech-

anisms modeled at the higher temperature are an oxidation layer, a $\gamma'$-precipitate free layer and a $\gamma'$-precipitate reduced layer. Model results for the creep response and for the thickness debit effect are in close quantitative agreement with the experimental results. In addition, the model predicts qualitative features of the failure process that are in good agreement with experimental observations. The simplicity of the model also allows parameter studies to be undertaken to explore the relative roles of bulk and surface damage as well as the relative roles of cleavage-like cracking and void nucleation in the bulk.

Another part of this dissertation aim at correlating the crack growth resistance and fracture surface morphology to material microstructure for ductile structural metals. The process that governs the ductile fracture of structural materials at room temperature is one of nucleation, growth and coalescence of micron scale voids, and involves large plastic deformations. The morphology of fracture surfaces reveals how microstructural features affect crack growth. Experimental studies have shown that fracture surfaces in a wide variety of materials and under a wide variety of loading conditions have remarkable scaling properties. For thirty years, the hope to relate the statistical characterization of fracture surfaces to a measure of a materials crack growth resistance has remained unfulfilled. Recent work suggests that analyses based on a damage constitutive relation for ductile fracture provide a promising tool for exploring this relation. Here, finite element, finite deformation calculations were carried out using a constitutive framework for progressively cavitating ductile solids. The matrix material was modeled as an isotropic hardening viscoplastic solid. The large inclusions, which nucleate voids at an early stage, were modeled as a three dimensional distribution of islands of the amplitude of the void nucleation function. Their size and spacing introduce a microstructurally based characteristic length into the formulation. The smaller second-phase particles, which require large strains for void nucleation, were uniformly distributed, and so did not introduce any physically based length scale. The calculations were carried out for small scale yielding conditions under remote Mode I loading. These simulations led to the exploration of the relation of both fracture toughness and fracture surface statistics to material properties and microstructure when the fracture mechanism

is one of void nucleation, growth and coalescence. The relation of both toughness and the statistical properties of fracture surfaces in calculations of heterogeneous microstructures to various microstructural features is discussed and a remarkable correlation between fracture surface roughness and fracture toughness is shown for the first time.

In summary in my PhD I have focused on correlating the material's microstructural features to specific failure modes through experimental observations and mechanistic simulations. Study of material failure begins with observations and descriptions. Computer simulations using an idealized model which are governed by the equations of mechanics provide insight into features that are not directly accessible experimentally. These simulations seek to provide trends, scaling relations and insight into the mechanisms of material failure. However, the observed patterns of behavior, when sufficiently clear, leads to the development of simple models which permits sensible planning in engineering applications and can be used to make better materials. My infinitesimally small contribution to the already existing field of "Mechanics of Materials" has been compiled in this dissertation. I have tried my best to be substantial and yet remain concise.

# CHAPTER 2

# EFFECT OF SPECIMEN THICKNESS ON THE CREEP RESPONSE OF A NI-BASED SINGLE CRYSTAL SUPERALLOY

## 2.1. Introduction

Single crystal Ni-based superalloys were introduced in the early 1980s [1]. Since then they have been widely used in turbine aerofoils in jet engines in order to allow for increased turbine inlet gas temperatures so as to improve thermal efficiency. The desire for weight reduction and the use of advanced metal cooling schemes to improve jet engine efficiency tends to drive designs toward thinner airfoil walls [2]. Creep tests on both polycrystalline and single crystal Ni-based superalloy specimens have shown greater creep strain rates and/or reduced strain to creep rupture for thinner specimens than predicted by current theories [3, 4, 5, 6, 7, 8, 9, 11, 10, 12, 13, 14]. This is known as the thickness debit effect. Current theories of creep deformation and rupture are expressed in terms of stress, strain, strain rate, rupture strain and rupture time, and so, for a given applied stress, predict size independent values of the creep strain rate and the creep rupture time and strain. Phrased another way, current theories predict that for a given applied force and given specimen width the creep strain rate and the creep rupture strain should scale with the specimen thickness. The understanding of creep in single crystal superalloy turbine blades is of importance for designing more reliable and fuel efficient aircraft engines.

A qualitative comparison of the thickness debit effect for conventionally cast, columnar grain and single crystal PWA1483 superalloy materials by Duhl [5] showed that the thickness debit effect is smallest for single crystals. Doner and Heckler [4, 6] investigated the thickness debit effect in single crystal CMSX-3 mini-flat specimens. Uncoated specimens with a thickness of 0.76mm tested in air at 982°C at a stress level below 275MPa exhibited a 30% reduction in the time to creep rupture as compared with specimens with a thickness of 3.18mm. On the other hand, Doner and Heckler [4, 6] observed no thickness debit effect for both aluminide coated and uncoated specimens tested in high purity argon. Hüttner

et al. [13, 14] reported a thickness debit effect in the creep response of both coated and uncoated René N5 single crystal superalloy specimens at a test temperature of 980°C. In [13, 14] coated samples showed a greater thickness debit effect than the corresponding uncoated samples. Hüttner et al. [13, 14] also showed that the samples with a misorientation of about 16° showed an increased thickness debit effect as compared with $< 001 >$ orientated samples. Seetharaman and Cetel [10] performed creep tests on uncoated PWA1484 (see Cetel and Duhl [15]) single crystal superalloy specimens in air at four conditions: 760°C/758MPa, 871°C/413MPa, 982°C/207MPa and 982°C/248MPa. They found a moderate thickness debit effect for the high temperature low stress (982°C/248MPa) condition and a greater thickness debit effect for the low temperature high stress (760°C/758MPa) condition.

Although attention here is focused on a single crystal superalloy, similar size dependent creep behavior has been observed in a variety of materials. Cane and Townsend [16] observed the effect of section size on the creep behavior of 0.5CrMoV steel. Storesund and Tu [17] showed that the creep life of a cross-weld bar specimen (1Cr0.5Mo weldment) is a strong function of specimen diameter. Size effect on the creep properties of lead free solders under several stress levels was observed by Ueno et al. [18]. Villain et al. [19] also observed size dependent creep response on both lead free and lead containing solders. In all cases increased creep strain rates and/or reduced creep life with decreasing sample dimensions were seen over a range of size scales similar to those for single crystal superalloy materials.

At smaller length scales, length scales of the order of tens of microns and smaller, room temperature plastic deformation size effects have recieved a great deal of attention both experimentally and theoretically, e.g. [20, 21, 22, 23, 24, 25, 26, 27, 28, 29, 30, 31, 32]. A variety of dislocation mechanisms are known to give rise to a room temperature size dependent plastic response including geometrically necessary dislocations, dislocation starvation and source truncation, e.g. [20, 26, 32, 29, 31, 30]. Micron scale size effects at elevated temperatures have received less attention, see [33, 34].

The thickness debit effect occurs at size scales of the order of hundreds of microns to millimeters and at elevated temperatures and, although it has been widely observed, the

mechanism (or mechanisms) responsible for the thickness debit effect have not been experimentally documented. The relatively larger size scale over which the thickness debit effect occurs suggests that the mechanisms leading to creep size effects can differ from those that give rise to room temperature size effects and a variety of mechanisms have been proposed as being responsible for the thickness debit effect. Baldan [9] presumed that the thickness debit effect occurs due to a damage mechanism occurring throughout the section and argued that the creep response is controlled by the crack size to section size ratio. Doner and Heckler [4, 6] suggested that the degradation in the time to creep rupture in their experiments was primarily due to environmental effects. Seetharaman and Cetel [10] considered several possible explanations including deformation constraint, cavity nucleation, growth and coalescence, environmental degradation and changes in anisotropy with section thickness. Gullickson et al. [35] assumed that the thickness debit effect observed in the creep tests of Seetharaman and Cetel [10] was due to damage occurring in a surface layer. They used a constitutive model for the nucleation and growth of voids and carried out three dimensional finite element analyses incorporating a surface damage layer. Cassenti and Staroselsky [36] modeled a mechanism involving an overstressed boundary layer created due to plastic slip and the preferential nucleation of voids or micro-cracks near surface to explain the thickness debit effect. The results for the thickness dependence of creep curves in [35, 36] were qualitatively consistent with the experimental observations. Bensch et al. [37] analyzed surface oxidation in uncoated specimens to model the thickness debit reported in [13, 14]. Their results indicated that surface oxidation could qualitatively explain the thickness debit effect in circumstances where environmental degradation is the main mechanism.

Given the variety of observations and proposed mechanisms, a further investigation of the mechanism (or mechanisms) responsible for the thickness debit effect in creep properties of single crystal superalloys is warranted. Here, the results of creep tests and the microscopic analysis of the test specimens aimed at identifying the mechanism (or mechanisms) responsible for the thickness debit effect are reported. The tests were performed on uncoated PWA1484 single crystal superalloy sheet specimens with thicknesses of 3.18mm

and 0.51mm at 760°C/758MPa and 982°C/248MPa (the same material and test conditions as in Seetharaman and Cetel [10]). Two specimens for each thickness and test condition were creep tested until rupture, while three creep tests at 982°C/248MPa were terminated after a time in the range of 30% to 70% of the time to rupture. In total eleven creep tests were conducted. Several finite element analyses were also carried out to aid in interpreting the experimental results.

2.2. Material Description and Experimental Procedure

Single crystal bars (25.4mm diameter × 228.6mm long) of PWA1484 [15, 38] alloy with nominal chemical composition of (weight percent) Co 10.0%, Cr 5.0%, Al 5.6%, Ta 8.7%, W 6.0%, Mo 2.0%, Re 3.0%, and Ni the balance was directionally solidified at Pratt & Whitneys in-house Rapid Prototype Casting Laboratory. X-ray diffraction (Laue) analysis and macro-etching were used to confirm that the bars were single crystals with a primary orientation within 10° of the [100] axis. The single crystal bars were subjected to a standard sequence of heat treatment cycles, viz., solution annealing at 1316°C (2400°F) for 2 hours in vacuum, coating diffusion heat treatment at 1080°C (1975°F) for 4 hours in a controlled atmosphere, and with a precipitation heat treatment at 704°C (1300°F) for 24 hours in air.

The creep test specimens with a gauge length of $\approx 25.58$mm, a width of $\approx 4.75$mm and a thickness of either $h = 0.51$mm or $h = 3.18$mm (Fig. 2.1) were electro-discharge machined from heat treated single crystal bars and ground to remove the recast layer. All creep test specimens were machined from bulk single crystal bars to eliminate the influence of variations in secondary dendrite arm spacing, micro-segregation patterns and initial micro-voids as in [10]. The sheet specimens were machined such that the orientation of the specimen width was within $\pm 2$ degrees of $< 100 >$ (see Fig. 2.1).

Metallographic studies were performed on all the creep tested specimens using scanning electron microscopy (SEM). Specimens creep tested in air at 982°C developed surface oxides where as no oxidation was observed on the specimens creep tested at 760°C. The chemical analysis of the oxides formed due to environmental effects during the high temperature creep tests (982°C) was performed using energy dispersive spectroscopy (EDS) in the

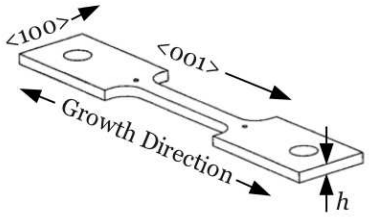


FIGURE 2.1. Schematic illustrating the shape and orientation of the uncoated PWA1484 single crystal superalloy sheet specimens used in the creep tests.

SEM using an Apollo X silicon drift detector (SDD) at 20kV excitation voltage. The measured X-ray intensities were converted to atom% using an atomic number absorbance and fluorescence (ZAF) program. Electron backscatter diffraction known as orientation imaging microscopy (OIM), was carried out using a field emission gun (FEI Nova 230) scanning electron microscope (FEGSEM) in order to determine the local texture and microstructural changes, if any.

## 2.3. Results

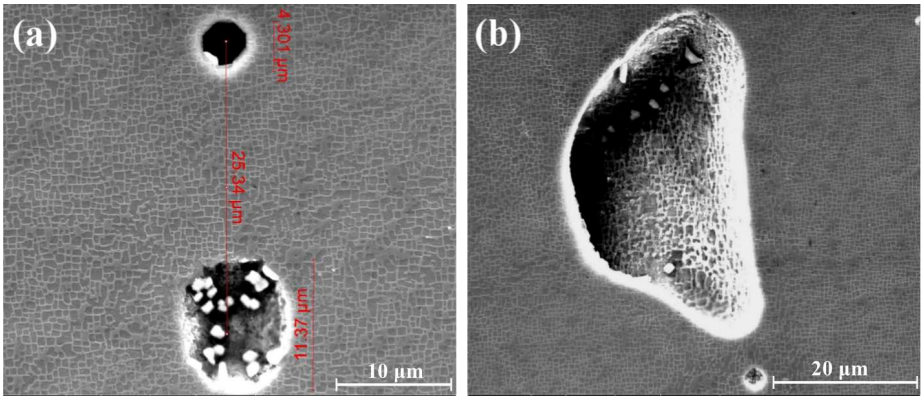


FIGURE 2.2. SEM images of the microstructure of the PWA1484 single crystal superalloy showing initial voids. (a) Two nearly spherical homogenization voids. (b) An irregular shaped shrinkage void.

The undeformed microstructure of the PWA1484 single crystal superalloy contained micro-voids formed during the solidification and homogenization processes as shown in Fig. 2.2 and also observed for other Ni-based single crystal superalloys, see e.g. [39, 40].

The nearly spherical voids in Fig. 2.2a are generally formed during the homogenization process while the larger, irregular shaped voids such as shown in Fig. 2.2b are mainly formed during the solidification process. The volume fraction of the micro-voids is generally low but the voids are mainly confined to the interdendritic regions of the crystal which results in a relatively high local void volume fraction. The dendrite arm spacing in a nickel base single crystal superalloy mainly depends on solidification velocity and thermal gradient [41]. The secondary dendrite arm spacings of the single crystal bars of PWA1484 used in the present study were less than 100$\mu$m.

Isothermal creep tests were carried out at Metcut Research Inc., Cincinnati, OH (USA) on uncoated specimens in air under two conditions: (i) a test temperature of 760°C (1400°F) with a fixed nominal stress (force/initial area) of 758MPa (110ksi); and (ii) a test temperature of 982°C (1800°F) with a fixed nominal stress of 248MPa (36ksi). At 760°C the ratio of applied stress to yield strength is 0.79 while at 982°C this ratio is 0.46 [10]. The elastic deformation was neglected and the creep data was recorded after applying the tensile load. The creep strain ($\varepsilon_c$) is defined as $\Delta\ell/\ell_0$, where $\ell_0$ is the initial gauge length. The creep data was recorded until a creep strain of 5% and after that the test was continued until rupture. Specimens that showed evidence of bending or that failed near the grips were discarded (there was one of each).

Based on the results of Seetharaman and Cetel [10] creep tests of two specimens of thickness 3.18mm at 982°C/248MPa were interrupted after a test duration of 75 hours ($\varepsilon_c$ = 0.63%) and 145.7 hours ($\varepsilon_c$ = 5.5%). For the 0.51mm thick specimens one test at 982°C/248MPa was interrupted after 51.2 hours ($\varepsilon_c$ = 0.76%) to explore the evolution of damage as a function of the accumulated creep strain. Subsequently, the creep tests conducted at 760°C/758MPa will be termed the low temperature high stress creep tests and the tests at 982°C/248MPa will be termed the high temperature low stress creep tests.

### 2.3.1. Low Temperature High Stress Results

The creep strain, $\varepsilon_c$, versus time, $t$, curves for the low temperature high stress loading condition for specimen thicknesses of 0.38mm, 0.76mm, 1.52mm and 3.18mm from the work

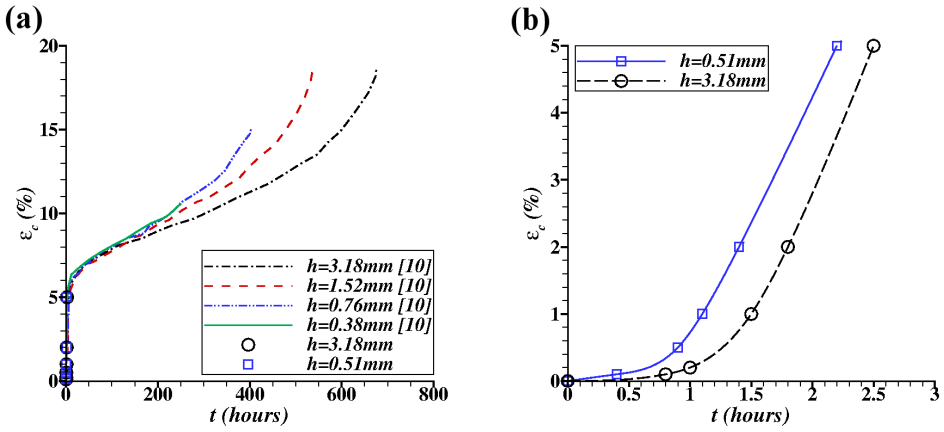


FIGURE 2.3. Creep strain, $\varepsilon_c$ versus time, $t$, curves for sheet specimens having various thicknesses, $h$, tested at 760°C with a 758MPa applied nominal stress. (a) Data from Seetharaman and Cetel [10] and the current work are shown. (b) Short time creep strain $\varepsilon_c$ versus time, $t$, curves for sheet thicknesses $h =$ 0.51mm and 3.18mm.

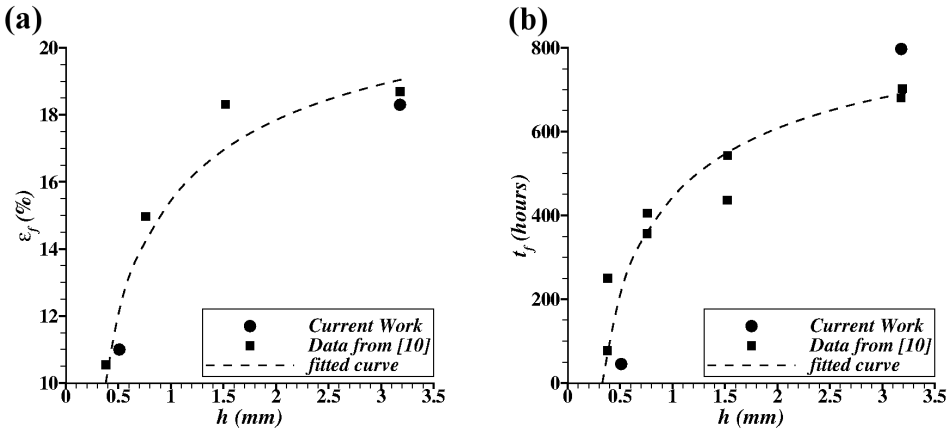


FIGURE 2.4. The effect of specimen thickness ($h$) on (a) the creep strain to fracture ($\varepsilon_f$) and (b) the time to fracture ($t_f$) of sheet specimens creep tested at 760°C/758MPa. Data from Seetharaman and Cetel [10] and the current work are included. The dashed line is a least squares fit of $a - b/\sqrt{h}$ to $\varepsilon_f$ and $t_f$ data, where $a$ and $b$ are positive fitting constants.

of Seetharaman and Cetel [10] along with the results for specimen thicknesses of 0.51mm and 3.18mm from the current work are shown in Fig. 2.3. Irrespective of the specimen thickness

the primary creep regime extends to approximately 6% strain. The creep curves up to 5% strain for a $h = 0.51$mm and a $h = 3.18$mm are shown in Fig. 2.3b. Both specimens showed a brief time delay before primary creep begins, as also reported in [42, 43], followed by a constant primary creep rate. Specimens of thickness 0.51mm reached 5% creep strain in 2.2 hours and those with thickness 3.18mm reached $\varepsilon_c = 5\%$ in 2.5 hours. The difference in time to 5% creep strain is very small compared with the difference in final creep rupture time. For specimens of thicknesses 0.76mm, 1.52mm and 3.18mm a deviation from steady state creep to tertiary creep occurred whereas failure occurred for the 0.38mm thick specimens in the secondary creep regime.

Figure 2.4 shows the effect of thickness on the creep strain to fracture, Fig. 2.4a, and on the time to fracture, Fig. 2.4b. The creep strain to fracture, $\varepsilon_f$, is nearly the same for $h = 3.18$mm and $h = 1.52$mm while for thinner specimens, the creep ductility is reduced. There is a more than 40% reduction in $\varepsilon_f$ for the specimens with a thickness of 0.38mm as compared with the specimens with $h = 3.18$mm. The time to creep rupture, $t_f$, is reduced by about 60% for $h = 0.38$mm as compared with that for $h = 3.18$mm. Interestingly the variations of both $\varepsilon_f$ and $t_f$ for this range of specimen thicknesses $h$ are well represented by a fit of the form $a - b/\sqrt{h}$, where $a$ and $b$ are positive fitting constants.

Standard fractography using secondary electron imaging (SE) in a scanning electron microscope (SEM) was performed. SEM images of the fracture surface for a $h = 3.18$mm specimen are shown in Fig. 2.5. Figure 2.5a shows the reconstructed fracture surface with the loading direction marked as $ld$ and with the thickness direction into the plane of the image. Specimens with $h = 3.18$mm showed pronounced tertiary creep and failed after $\varepsilon_c \approx 18\%$. Failure of the $h = 3.18$mm specimens are accompanied by localized necking with the cross-sectional area near fracture surface being approximately 10% less than the cross-sectional area of the far gauge section. Micro-cracks are also present away from the fracture region on the gauge section. No surface oxidation was observed in the low temperature high stress specimens.

The fracture morphology in Fig. 2.5b shows stepped cleavage-like planes as well as

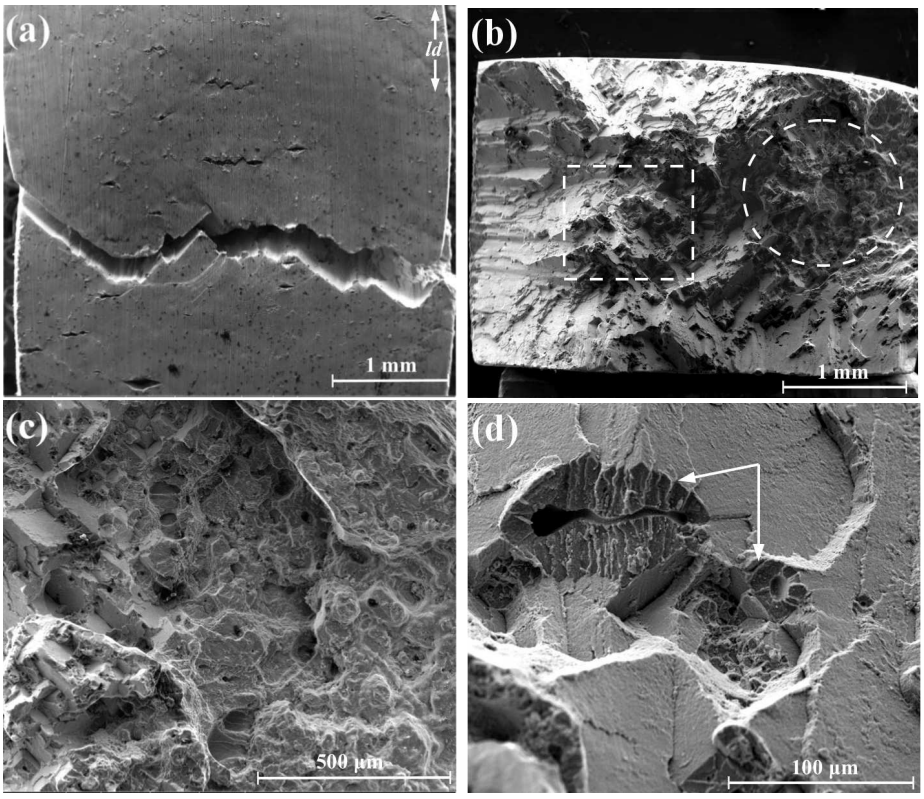


FIGURE 2.5. SEM images of a 3.18mm thick sheet specimen tested at 760°C/758MPa. (a) The region near the fracture surface reconstructed after rupture (the loading direction is *ld* and the sheet thickness is into the plane). (b) The fracture morphology of the upper half of the specimen in (a) (the loading direction is into the viewed plane). (c) Zoomed view of the region enclosed by the dotted circle in (b). (d) Zoomed view of the region enclosed by the dotted rectangle in (b).

micro-voids. The crystallographic cleavage-like planes have traces of slip bands showing evidence of creep deformation by a slip process. The edges of the projected fracture surface are inclined at an angle $\approx 45°$ with respect to the loading axis, i.e. a $< 001 >$ crystallographic direction so that these edges are along a $< 011 >$ direction. The maximum resolved shear stress is at 45° to the tensile direction and, since $\{111\}$ planes intersect with $\{100\}$ planes along $< 011 >$ directions, these cleavage-like planes are $\{111\}$ planes. A similar observation was made by Sherry and Pilkington [44] in creep rupture testing of single-crystal superalloy

SRR99 at 750°C. The presence of numerous crystallographic facets indicate that the rupture process involves multiple {111} planes. The zoomed view of the region with void activity in Fig. 2.5c shows numerous shallow voids joined by shear along slip bands. In Fig. 2.5d voids connected by micro-cracks are also seen. At several locations the fracture surface surrounding the voids is orthogonal to the loading axis as in brittle fracture, marked by the arrow in Fig. 2.5d. Also two intersecting {111} crystallographic cleavage-like planes can be seen.

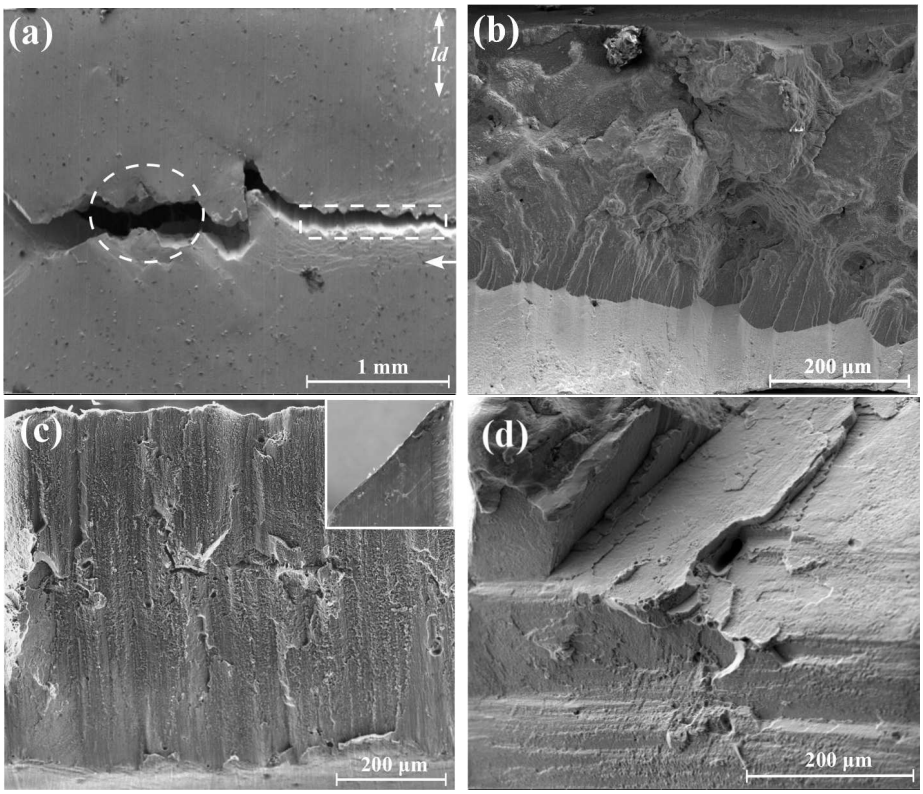


FIGURE 2.6. SEM images of a 0.51mm thick sheet specimen tested at 760°C/758MPa. (a) The region near the fracture surface reconstructed after rupture (the loading direction is *ld* and the sheet thickness is into the plane). (b) The fracture morphology of the region marked by a dotted circle in (a) (the loading direction is into the viewed plane). (c) The fracture morphology of the region marked by a dotted rectangle in (a) and the inset shows the side view marked by the arrow in (a). (d) Zoomed view of the fracture surface showing stepped cleavage-like planes.

Figure 2.6 shows SEM images of the fracture surface for a $h = 0.51$mm specimen. Unlike the $h = 3.18$mm specimens there is no evidence of micro-cracks on the surface away from the fracture region of the $h = 0.51$mm specimens as shown in the reconstructed fracture surface in Fig. 2.6a. Also no significant necking is observed and the specimens failed at a very low creep strain of $\varepsilon_c \approx 11\%$ as compared to $h = 3.18$mm specimens. However, there is a shear lip in the extreme left of Fig. 2.6a. The orthogonal view of the region marked with a dotted circle in Fig. 2.6a is shown in Fig. 2.6b. In the upper half of Fig. 2.6b there is a region that contains numerous micro-cracks that apparently originated from micro-voids. A shear lip inclined at an angle of approximately 45° to the loading axis can also be seen at the bottom of the image. The shear lip in Fig. 2.6b contains numerous cleavage-like steps. At the root of the shear lip a river pattern [45] can be seen. The region marked with a dotted rectangle in Fig. 2.6a and shown in Fig. 2.6c is flat with the right side edge inclined at an angle of $\approx 45°$ to the loading axis, as can be seen in the inset. Micro-cracks and micro-voids are present on this surface. Figure 2.6d shows a zoomed view of the fracture surface between the dotted circle and the dotted rectangle in Fig. 2.6a. The presence of intersecting crystallographic cleavage-like planes shows that rupture in this region occurred along more than one $\{111\}$ family of planes unlike what is observed near one end of the specimen as shown in Fig. 2.6c.

The major differences between the fracture morphology of thick and thin specimens can be summarized as, (i) an increased cleavage-like fracture and (ii) a transition from heterogeneous multi crystallographic cleavage-like fracture to mainly single plane cleavage-like fracture with reducing specimen thickness. The presence of initial micro-voids are the preferred sites for crack nucleation as shown in Figures 2.7a and 2.7b. The SEM images in Figs. 2.7a and 2.7b are taken from the section above the fracture surface of a specimen with $h = 0.51$mm. As shown in Fig. 2.7a the voids elongate predominantly in the loading direction and precipitate cracks near (but not at) the tip of the deformed void. The transverse view of another deformed void is shown in Fig. 2.7b. Once a crack initiates it propagates along planes, probably $\{111\}$ planes, that have a high resolved shear stress. The bead-like structure

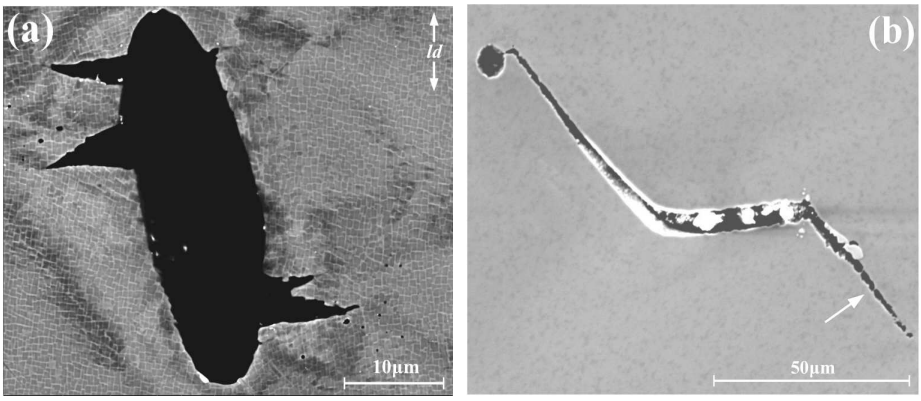


FIGURE 2.7. SEM images from the section near fracture surface of a specimen with $h = 0.51$mm tested at 760°C/758MPa. (a) Initiation of micro-cracks from the surface near the tip of the elongated void (the loading direction is $ld$). (b) Growth of crack initiated from the surface of a void (the loading direction is into the viewed plane).

on the slant portion of the crack in Fig. 2.7b (marked with an arrow) shows the presence of connected micro-voids. Deformed voids and micro-cracks such as those in Fig. 2.7 are also seen with $h = 3.18$mm specimens at locations just above the fracture surface. The loss of area associated with cleavage-like cracks nucleating from deformed voids as in Fig. 2.7 has a greater impact on the load carrying capacity of thinner specimens leading to a transition from creep-ductile to creep-brittle behavior with reducing specimen thickness.

### 2.3.2. High Temperature Low Stress Results

Curves of creep strain versus time for specimen thicknesses of $h = 0.51$mm and $h = 3.18$mm tested at a temperature of 982°C and a nominal stress of 248MPa are shown in Fig. 2.8. The creep strain versus time curves were recorded up to a creep strain of 5%. Two tests for each specimen thickness were continued to rupture while two tests on specimens with $h = 3.18$mm were interrupted after test durations of 75 hours and 145.7 hours. One test on a specimen with $h = 0.51$mm was interrupted after a test duration of 51.2 hours. The interrupted tests allowed exploration of damage evolution as a function of accumulated creep strain. As shown in Fig. 2.8 the time to reach 5% creep strain for a specimen with

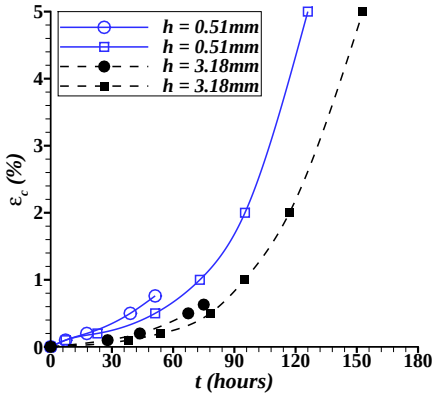


FIGURE 2.8. Creep strain ($\varepsilon_c$) versus time ($t$) curves for sheet specimens with $h = 0.51$mm and $h = 3.18$mm tested at 982°C and with 248MPa applied nominal stress to a creep strain of $\varepsilon_c = 5\%$. Also shown are creep strain versus time curves for creep tests interrupted after $t = 51.2$ hours for $h = 0.51$mm and after $t = 75$ hours for $h = 3.18$mm.

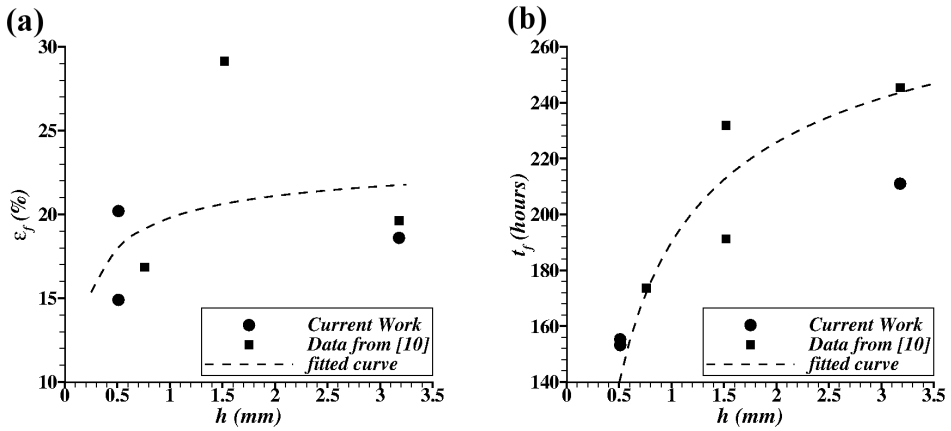


FIGURE 2.9. The effect of specimen thickness ($h$) on (a) the creep strain to fracture ($\varepsilon_f$) and (b) the time to fracture ($t_f$) for sheet specimens creep tested at 982°C/248MPa. Data from Seetharaman and Cetel [10] and the current work are included. The dashed line is a least squares fit of $a - b/\sqrt{h}$ to $\varepsilon_f$ and $t_f$ data, where $a$ and $b$ are positive fitting constants.

$h = 3.18$mm is 152 hours while for a specimen with $h = 0.51$mm it is 125 hours. The plots in Fig. 2.8 show an increased creep rate with decreasing thickness at low strain levels for

both the specimens tested to rupture and for the interrupted tests.

The creep strain to rupture and the time to rupture for specimens with $h = 0.51$mm and with $h = 3.18$mm from the current work and for specimens with $h = 0.76$mm, $h = 1.52$mm and $h = 3.18$mm from the work of Seetharaman and Cetel [10] are shown in Figs. 2.9a and 2.9b, respectively. There is a clear dependence of the time to rupture on specimen thickness as shown in Fig. 2.9b. On the other hand, there is no clear dependence of the creep strain to rupture on specimen thickness. The largest value of $\varepsilon_f$ occurs for $h = 1.52$mm and, even if that point is neglected, the dependence of $\varepsilon_f$ on specimen thickness $h$ is relatively weak. The dotted lines in Fig. 2.9 show a least squares fit to $a - b/\sqrt{h}$. The fit in Fig. 2.9a reflects the weak dependence on specimen thickness whereas the fit in Fig. 2.9b shows a strong dependence on $h$. The specimens with thickness $h = 3.18$mm ruptured after 210 hours whereas the specimens with $h = 0.51$mm ruptured after 155 hours, a reduction of about 25% in the time to creep rupture.

In contrast to the creep tests at 760°C significant surface oxidation was observed during the creep tests at 982°C. Figures 2.10a and 2.10b shows the surface textures of the gauge region surface oxide after various creep exposure times for specimens with thicknesses $h = 0.51$mm and Figs. 2.10c and 2.10d show the same for specimens with $h = 3.18$mm. As will be shown subsequently, layer A is an Al-rich oxide layer and layer M is a mixed oxide layer. After 51.2 hours of creep exposure time for $h = 0.51$mm and 75 hours of creep exposure time for $h = 3.18$mm, the gauge region surfaces show a single oxide layer marked as layer A in Figs. 2.10a and 2.10c. With continuing creep exposure layer A on the specimen gauge surface develops cracks perpendicular to the loading direction. These cracks expose metal to air for further oxidation. The oxides formed in the open cracks are shown in Fig. 2.10b for a $h = 0.51$mm and in Fig. 2.10d for a $h = 3.18$mm specimen. This shows that the cracks formed in the surface oxide layers were arrested due to further oxidation. So that propagation of these cracks did not play a role in the creep rupture process. The grip regions of all specimens creep tested at 982°C/248MPa also showed M and A oxide layers with significant spallation of layer M. The surface texture of the gauge region did not depend

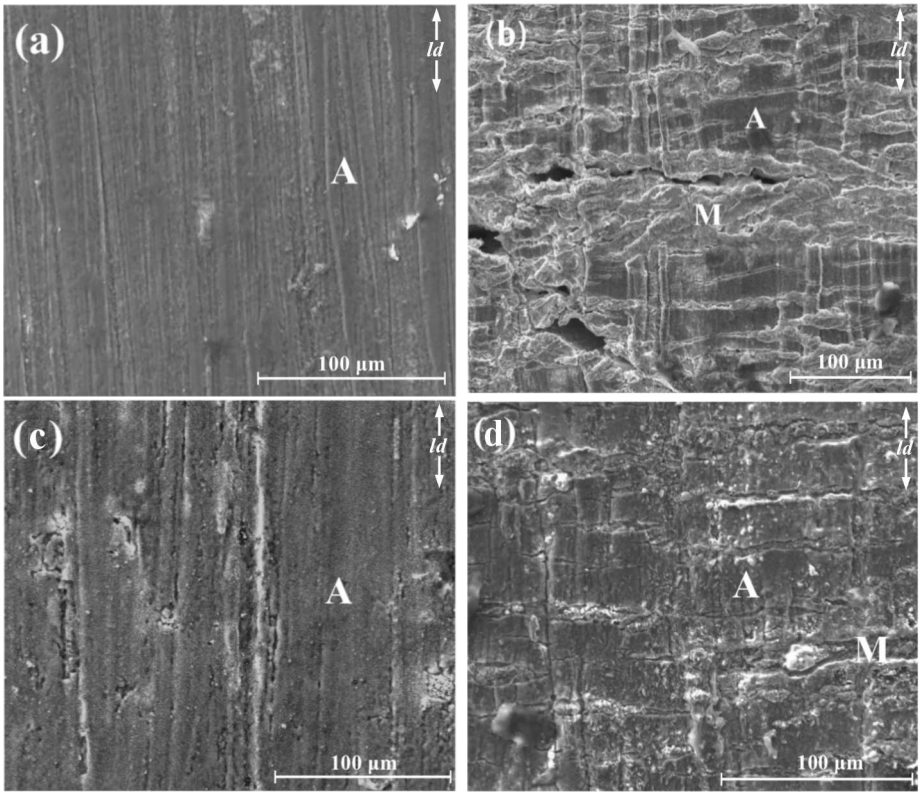


FIGURE 2.10. SEM images showing the evolution of the specimen surface of the gauge region during the creep test at 982°C/248MPa (the loading direction is $ld$). (a) A $h = 0.51$mm thick specimen after 51.2 hours. (b) A $h = 0.51$mm thick specimen after creep rupture. (c) A $h = 3.18$mm thick specimen after 75 hours. (d) A $h = 3.18$mm thick specimen after creep rupture. 'A' marks the Al-rich oxide and 'M' marks the mixed oxide.

on the creep exposure time.

A further examination of the oxide layers is important to analyze the progressive loss of load-carrying cross-section of the specimens as it will affect thinner specimens more than thicker specimens. Metallographic examination of the polished samples taken from near the fracture region of the gauge section of the creep ruptured specimens showed the presence of various layers of oxides and the microstructure that developed in the alloy. One of the images taken from near the fracture surface of a $h = 3.18$mm creep ruptured specimen is shown in Fig. 2.11. Similar layers can also be seen in 0.51mm thick specimens. There are three layers of oxides, layer N, layer M and layer A. The first layer after the oxide layers is

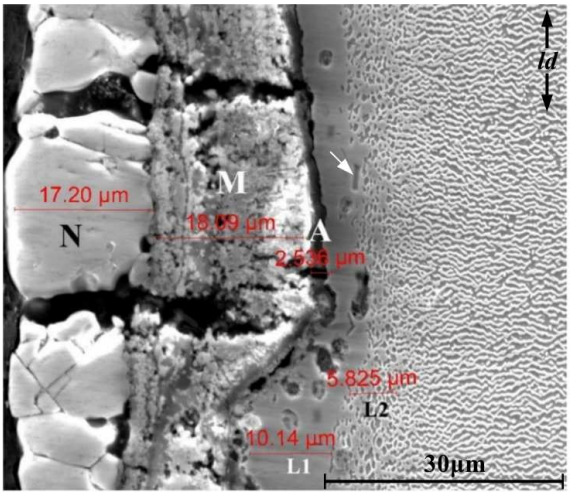


FIGURE 2.11. SEM image from near the fracture surface showing three layers of oxides in a $h = 3.18$mm specimen creep tested at 982°C/248MPa. N marks the Ni-rich oxide layer. M marks the mixed oxide layer. A marks the Al-rich oxide layer. L1 marks the $\gamma'$ free layer. L2 marks the $\gamma'$ reduced layer. The rafting in the bulk can be seen. The arrow marks the presence of faceted precipitates in the L1 layer. The loading direction is *ld*.

a precipitate free layer, denoted as layer L1. As shown in the Fig. 2.11 no $\gamma'$ precipitates are present in this layer. Two interesting features observed in layer L1 are the presence of large micro-voids and faceted precipitates (marked with an arrow). After the $\gamma'$-free layer is the depleted $\gamma'$ precipitate layer, denoted as L2. The extensive rafting of $\gamma'$ normal to the loading direction in the bulk of the material is consistent with other observations on superalloys characterized by a small negative misfit between the lattices of $\gamma$ and $\gamma'$ phases, e.g. [46, 47, 48].

The first two oxide layers shown in Fig. 2.11 are present in small patches on specimen surfaces both at the stressed gauge section and the unstressed grip section. The EDX spectra in Fig. 2.12 identifies layer N as a Ni-rich oxide layer; Layer-M as a mixed oxide of Ni, Al, Ta, Cr and Co; and the adherent layer A as the Al-rich oxide. The mixed oxide M is also present in the cracks in the adherent layer A as shown in Figs. 2.10b and 2.10d. The quantification of EDX spectra from the faceted precipitates in the $\gamma'$-free layer in Fig. 2.11

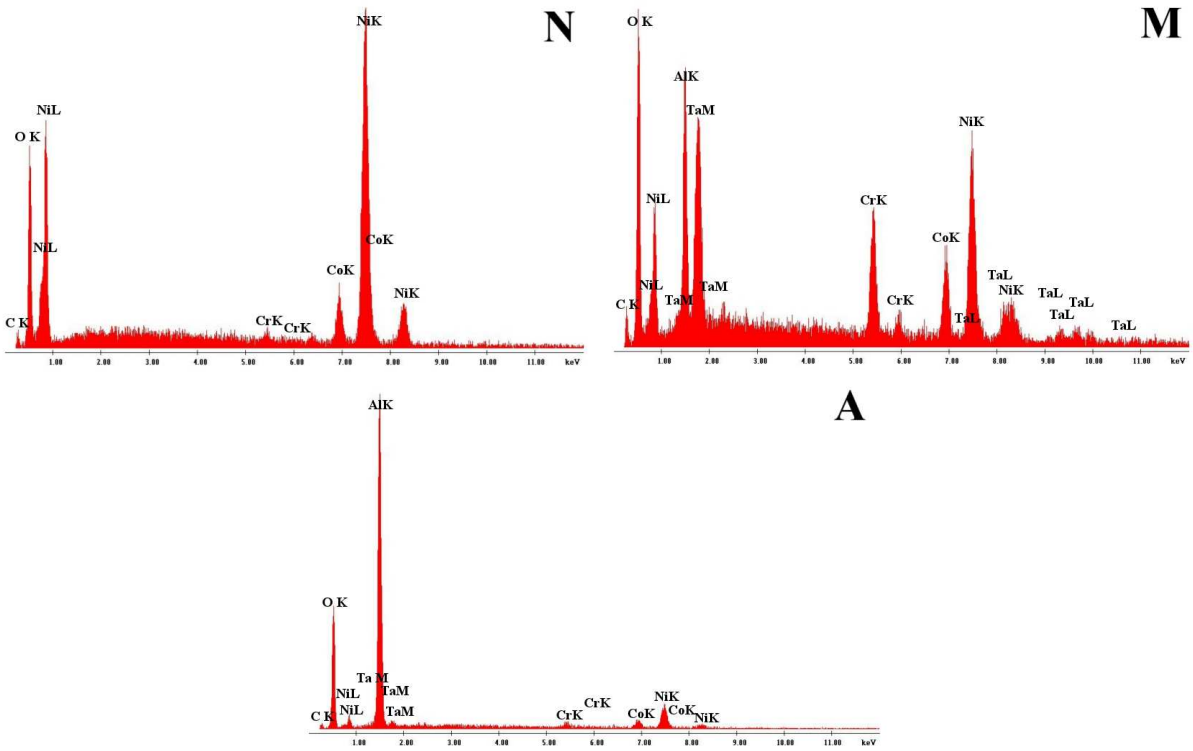


FIGURE 2.12. EDX spectra from the representative regions marked as N, M and A in Fig. 2.11.

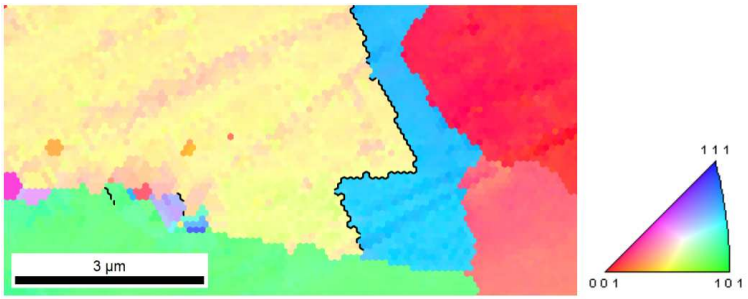


FIGURE 2.13. Inverse pole figure map of the $\gamma'$ free zone in a specimen creep tested to fracture at 982°C/248MPa. The map is given in the [001] orientation. The recrystallized grain orientations can be seen from the color-coded stereographic triangle. $\Sigma_3$ (twin) boundaries are marked in black.

suggests the presence of a $\beta$ (NiAl) phase similar to what has been reported in oxidation studies of CMSX-10 by Akhtar et al. [49]. The EBSD inverse pole figure, Fig. 2.13, of the $\gamma'$ precipitate free zone in Fig. 2.11 shows the presence of recrystallized grains. Figure 2.13

represents an area of $9.1 \times 4.6\mu m^2$ and the electron beam was scanned in steps of $0.1\mu$m. The EBSD pattern was indexed using the nickel fcc phase. Dynamic recrystallization in the precipitate free zone under the oxide scale occurred both in specimens with $h = 3.18$mm and $h = 0.51$mm. Oxidation induced dynamic recrystallization of the near surface region during thermomechanical fatigue of CMSX-4 single crystal superalloy has been recently reported by Moverare and Johansson [50]. Surface recrystallization of single crystal superalloys has been generally observed in circumstances where the surface is predeformed via surface indentation [51] or shot peening [52]. In the absence of residual plastic strain and at a temperature well below the solvus temperature of $\gamma'$ precipitates, dynamic recrystallization is mainly due to oxidation induced precipitate depletion. The dynamic recrystallization mainly resulted in subgrain boundaries and recrystallization twin boundaries. The grain boundaries that form during recrystallization could promote creep cavitation and, indeed, an increase in the number of voids in the precipitate free zone is seen in Fig. 2.11. Hence, oxidation not only contributes to a reduction in load carrying cross-sectional area but also leads to processes that produce a boundary layer prone to void nucleation. The size of the recrystallized zone formed due to oxidation during high temperature creep will be independent of the specimen thickness and will have more adverse effect on thinner specimens.

Figure 2.14 compares the evolution of micro-voids and micro-cracks for the specimens with $h = 0.51$mm and $h = 3.18$mm. Figures 2.14a and 2.14b show the accumulated damage in the gauge region of a specimen interrupted after 51.2 hours ($\varepsilon_c$=0.76%) and in the region above the fracture surface of a creep ruptured ($\varepsilon_f$=14.9% and $t_f = 155$ hours) specimen with $h = 0.51$mm. Similarly Figs. 2.14c and 2.14d show micro-voids and micro-cracks in the gauge region of a specimen interrupted after 75 hours ($\varepsilon_c$=0.63%) and in the region above the fracture surface of a creep ruptured ($\varepsilon_f$=18.6% and $t_f = 210$ hours) specimen with $h = 3.18$mm. The comparison of Figs. 2.14a and 2.14b and of Figs. 2.14c and 2.14d reveals an increase in the number and size of micro-voids with increasing creep deformation. Several voids are elongated in the loading direction (as shown in the inset of Fig. 2.14b) and also many voids have initiated micro-cracks near the tip of the elongated void or have

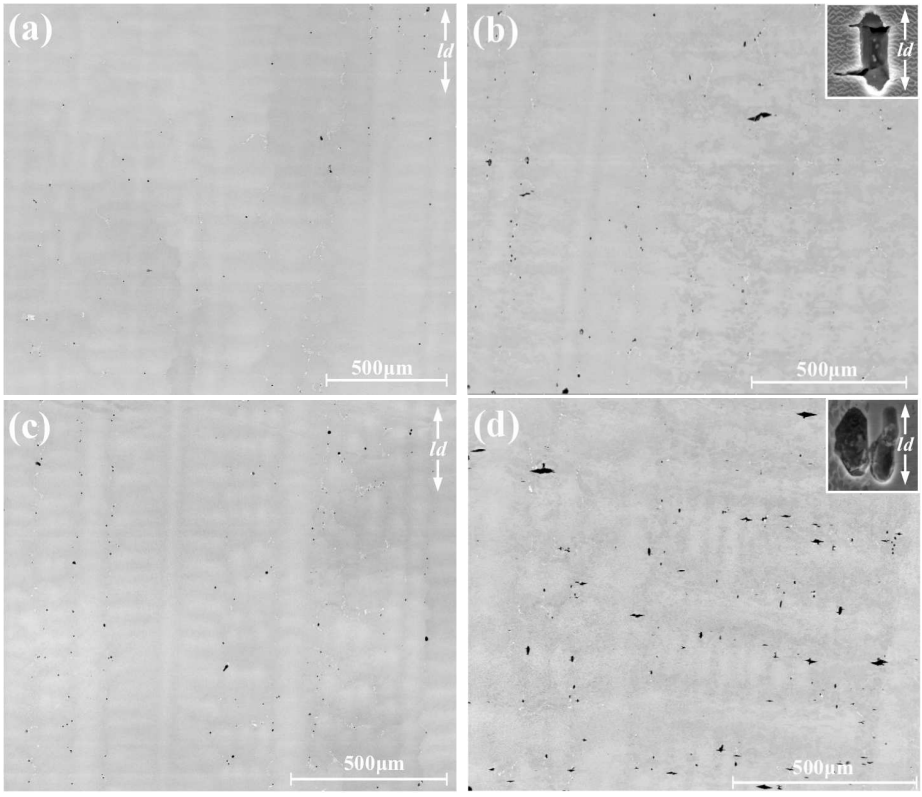


FIGURE 2.14. SEM images showing evolution of damage in the gauge region of the specimens creep tested at 982°C/248MPa. (a) A $h = 0.51$mm thick specimen after 51.2 hours. (b) A $h = 0.51$mm thick specimen after creep rupture. (c) A $h = 3.18$mm thick specimen after 75 hours. (d) A $h = 3.18$mm thick specimen after creep rupture. The loading direction is $ld$.

coalesced with the neighboring void perpendicular to the loading direction (as shown in the inset of Fig. 2.14d). The increased number of voids observed after creep deformation indicates nucleation of new voids as well as the growth of existing voids. Epishin and Link [53] observed similar nucleation and growth of voids in the interdendritic regions and at the $\gamma$-$\gamma'$ interfaces. A comparison of Fig. 2.14b with 2.14d shows an increased number and size of micro-voids and an increased number of micro-cracks in the creep ruptured specimens with $h = 3.18$mm as compared with the specimens with $h = 0.51$mm. This suggests that the thicker specimens are more damage tolerant than the thinner specimens as in the case of low temperature high stress creep.

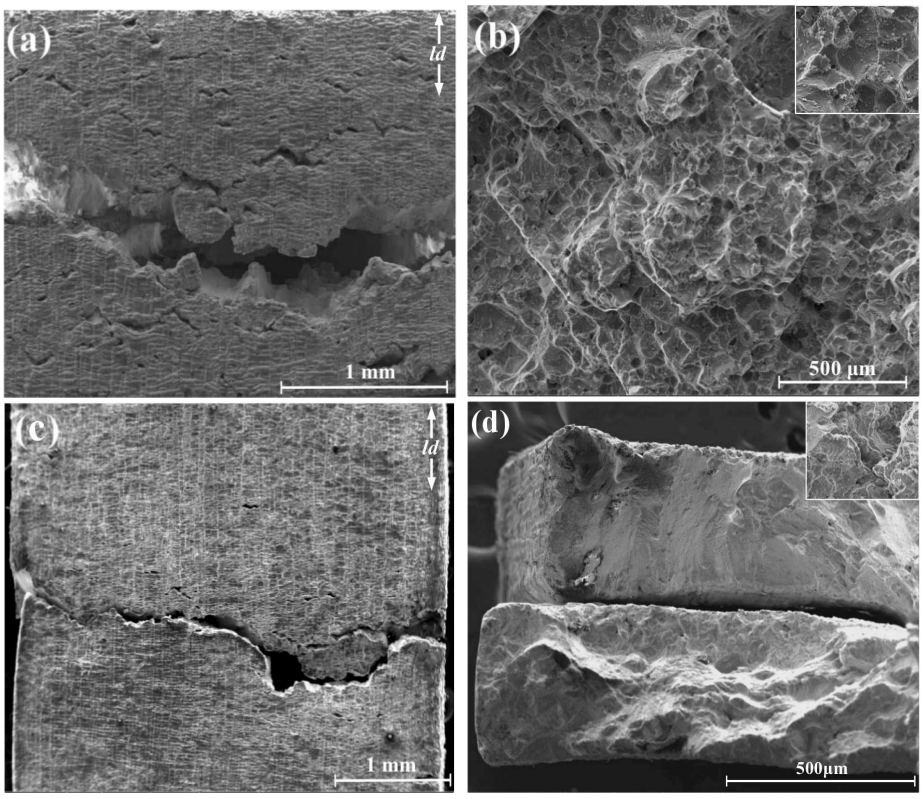


FIGURE 2.15. SEM images of the sheet specimens tested at 982°C/248MPa. (a) The region near the fracture surface of a 3.18mm thick specimen reconstructed after rupture (the loading direction is $ld$ and the sheet thickness is into the plane). (b) The fracture morphology of the one half of the specimen in (a) (the loading direction is into the viewed plane). (c) The region near the fracture surface of a 0.51mm thick specimen reconstructed after rupture (the loading direction is $ld$ and the sheet thickness is into the plane). (d) Two non-mating halves of the fracture surface of the specimen in (c) (the loading direction is into the viewed plane).

SEM images of the fracture surface of a $h = 3.18$mm and of a $h = 0.51$mm specimen tested under the high temperature low stress condition are shown in Fig. 2.15. The SEM image of a reconstructed creep ruptured specimen with thickness $h = 3.18$mm is shown in Fig. 2.15a and with thickness $h = 0.51$mm is shown in Fig. 2.15c. The tensile loading direction is marked by $ld$ and the thickness direction is into the plane of the image. The

presence of micro-cracks perpendicular to the loading direction can be seen in the gauge section away from the fracture surface. Specimens with $h = 0.51$mm show fewer micro-cracks in the gauge section as compared with $h = 3.18$mm specimens. The $h = 0.51$mm specimens and $h = 3.18$mm specimens failed after undergoing roughly the same creep strain. Under high temperature low stress creep loading conditions $h = 0.51$mm thick and $h = 3.18$mm thick specimens showed gradual reduction in the cross-sectional area with cross-sectional area near fracture section roughly being $25 - 30\%$ less than the cross-sectional area of the far gauge section.

A dimpled fracture morphology can be seen in Fig. 2.15b for a $h = 3.18$mm specimen. The zoomed view of the fracture morphology in the inset of Fig. 2.15b shows the presence of micro-voids and micro-cracks in cup-like depressions. The fracture morphology indicates that the rupture occurred due to the nucleation, growth and coalescence of voids and not because of micro-cracks initiated in the oxide layer as these cracks were arrested after further oxidation. The two non-mating halves of the fracture surface of a $h = 0.51$mm specimen are shown in Fig. 2.15d. The fracture surface shows the presence of deformed micro-voids and irregular bulged areas (bottom half of Fig. 2.15d and the inset). This type of fracture morphology is observed over 50% fraction of the fracture surface. Near one end of the fracture surface, as shown in the upper half of Fig. 2.15d, cleavage-like steps can be seen that are inclined to the loading direction. There is a transition from more or less complete ductile fracture for thicker specimens to a mix mode of ductile and cleavage-like fracture for thinner specimens. This transition, together with the environmental effects, plays a major role in the observed thickness debit effect under the high temperature low stress condition.

## 2.4. Discussion

The thickness debit effect of sheet specimens of PWA1484 Ni-based single crystal superalloy has a distinctly different manifestation in the two creep test conditions considered. In the low temperature high stress creep condition (760°C/758MPa) the thickness debit effect has the form of a reduction in the creep strain to rupture and the time to rupture with decreasing specimen thickness. The fracture surfaces for the thinner specimens are

more cleavage dominated and the creep strain versus time response exhibits little or no tertiary creep. The thickness debit effect at the high temperature low stress creep condition (982°C/248MPa) has the form of an increase in creep rate even at low creep strain levels and a reduction in the time to creep rupture with decreasing thickness but with no, or limited, dependence of the creep strain to rupture on specimen thickness, even though the fracture surfaces for the thinner specimens are more cleavage dominated as for the case of low temperature high stress creep.

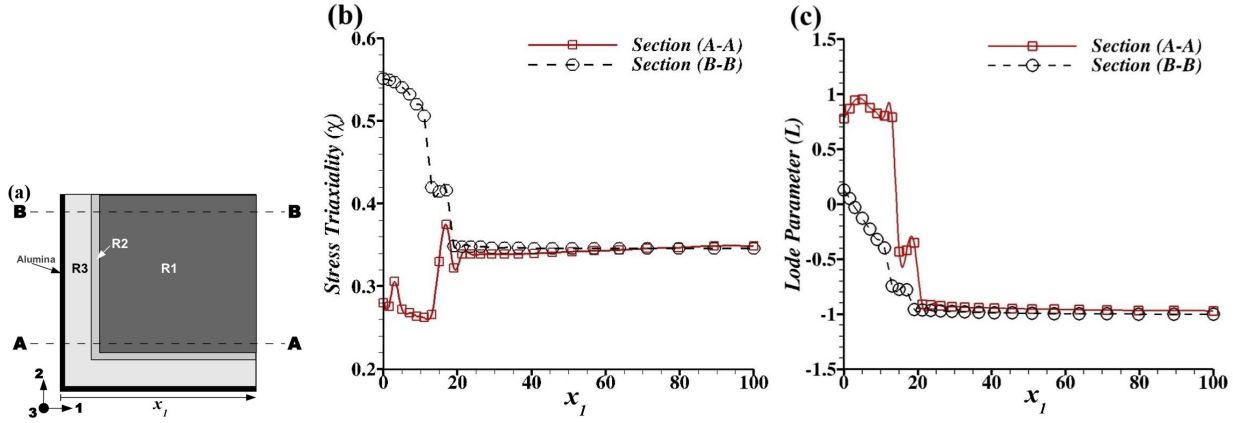


FIGURE 2.16. Computational results for the change in stress state near the free surface due to an adherent surface oxide and dynamic recrystallization for applied uniaxial creep loading in the $x_3-$direction giving $\chi = 1/3$ and $L = -1$. (a) Sketch of the cross section of the configuration analyzed. (b) Variation of stress triaxiality $\chi$ on two cuts. (c) Variation of the value of the Lode parameter $L$ on two cuts.

The adherent surface oxide and the layered structure that forms near the surface at 982°C/248MPa will affect the stress distribution in the specimen. Finite element finite deformation calculations were carried out to explore this effect. The material in each layer was taken to follow the isotropic Norton power law creep relation

$$\dot{\epsilon}_e = \dot{a}\left(\frac{\sigma_e}{\sigma_0}\right)^n \tag{1}$$

where $\sigma_e$ is the Mises effective stress and $\dot{\epsilon}_e$ is the corresponding effective strain rate. The commercial program ABAQUS [54] was used with C3D20H elements (20 node hybrid ele-

ments). Constant engineering stress creep loading, as in the experiments, was imposed in the $x_3$ direction. The deformation was assumed uniform in the $x_3$ direction so that only 5 layers of elements normal to the $x_3$ direction were used. On one external plane normal to the loading direction $u_3 = U$ is imposed for all nodes while $u_3 = 0$ is for all nodes on the opposite normal plane. The displacement $u_1$ was taken to vanish on the external surface parallel to the $x_1$ direction similarly $u_2 = 0$ on the external surface parallel to the $x_2$ direction in order to simulate the constrain imposed by the adherent alumina layer. Since the adherent alumina layer readily cracks normal to the loading direction hence it is assumed that it does not impose any constraint in the loading direction ($x_3$ direction). Symmetry conditions were imposed on the sides at $x_1 = 100\mu$m and $x_2 = 100\mu$m.

The creep properties of regions R2 and R3 are not known but it is expected that the creep rate increases with a decreasing volume of $\gamma'$ as assumed in [37]. The parameters $\sigma_0$ and $n$ are chosen to exhibit this trend in creep rate and the reference strain rate $\dot{a}$ is fixed at $7.59 \times 10^{-8}\text{s}^{-1}$. In region R1 $\sigma_0 = 150$MPa and $n = 5$, in region R2 $\sigma_0 = 15$MPa and $n = 5$ and in region R3 $\sigma_0 = 6.92$MPa with $n = 7$. Note that in Eq. 1 the values of $\sigma_0$ and $\dot{a}$ do not independently affect $\dot{\epsilon}_e$; all that matters is the combination $\dot{a}/\sigma_0^n$. The elastic constants in region R1 was taken as $C_{11} = 271$GPa, $C_{12} = 194$GPa and $C_{44} = 105$GPa, region R2 was assumed to be elastically isotropic with $E = 210$GPa and Poisson's ratio 0.3, and region R3 was also assumed to be elastically isotropic with $E = 200$GPa and Poisson's ratio 0.31. The calculations were continued to an engineering creep strain of 10%.

Figures 2.16b and 2.16c illustrates the change in stress state that can occur due to the development of a heterogeneous microstructure. Figure 2.16b shows the variation of stress triaxiality $\chi$ and Fig. 2.16c shows the variation in Lode parameter $L$ along the sections A-A and B-B. The stress triaxiality $\chi$ is the ratio of the first to second stress invariants and is given by

$$\chi = \frac{\Sigma_h}{\Sigma_e} \tag{2}$$

where

$$\Sigma_e = \frac{1}{\sqrt{2}}\sqrt{(\Sigma_1 - \Sigma_2)^2 + (\Sigma_2 - \Sigma_3)^2 + (\Sigma_3 - \Sigma_1)^2} \tag{3}$$

$$\Sigma_h = \frac{1}{3}(\Sigma_1 + \Sigma_2 + \Sigma_3) \tag{4}$$

The stress triaxiality is 1/3 for uniaxial tension. The influence of the third stress invariant is assessed via the Lode parameter, $L$, which is given by

$$L = \frac{2\Sigma_2 - \Sigma_1 - \Sigma_3}{\Sigma_1 - \Sigma_3} \tag{5}$$

The value of the Lode parameter ranges from $-1$ to $+1$ with $L = -1$ for uniaxial tension.

The constraint imposed on the free surface of the region R3 results in a decrease in stress triaxiality value near the corner and an increase in the value of $\chi$ away from the corner. Away from the surface stress triaxiality $\chi$ and Lode parameter $L$ attain values corresponding to a uniaxial state of stress ($\chi = 1/3$ and $L = -1$). The variation of $L$ in the regions R2 and R3 covers the entire range from $-1$ to 1. It is in the R2 and R3 layers that increased micro-cracks, as well as void nucleation, was seen in the specimens tested at 982°C/248MPa. It is worth noting that the change in stress state associated with the formation of a layered structure will also affect the material response during thermomechanical fatigue.

In both the low temperature high stress condition, 760°C/758MPa, and the high temperature low stress condition, 982°C/248MPa, the initial voids can precipitate nucleation of cleavage-like cracks so that the thickness debit effect is a bulk effect arising from the increased crack size to thickness ratio for thinner specimens. At least under the conditions considered here, the results indicate that bulk effects play a major role in the observed thickness debit effect. In the high temperature low stress condition surface effects including oxidation, dynamic recrystallization and the formation of a boundary damage layer leading to a near surface change in stress state play contributing roles as well. The surface effects are independent of specimen thickness and hence affects thinner specimens more than thicker ones.

## 2.5. Summary and Conclusions

Isothermal, constant nominal stress creep tests at two test conditions 760°C/758MPa and 982°C/248MPa were performed on uncoated PWA1484 Ni-based single crystal superalloy sheet specimens of thickness $h = 3.18$mm and $h = 0.51$mm. Metallographic studies showed that the specimens contained initial voids mainly in the interdendritic regions. To understand the contribution of various mechanisms possibly leading to the thickness debit effect, creep tests at 982°C/248MPa were interrupted after $t = 75$ hours and $t = 145.7$ hours for specimens of $h = 3.18$mm and after $t = 51.2$ hours for specimen of $h = 0.51$mm. The dependence of the creep response on specimen thickness differed under the two test conditions:

*Low temperature high stress condition (760°C/758MPa):*

- There was little effect of specimen thickness on the steady-state creep rate. The main effect of specimen thickness was on the onset of tertiary creep and for $h = 0.38$mm failure occurred prior to any tertiary creep.
- A decrease in specimen thickness from 3.18mm to 0.38mm resulted in over 40% reduction in the creep strain to rupture and around a 60% reduction in the time to rupture.
- Neither oxide formation on the specimen surfaces, rafting nor void nucleation was observed.
- With $h = 3.18$mm a mixed mode of failure involving ductile void growth and coalescence and cleavage-like cracking was observed. With $h = 0.51$mm cleavage-like cracking covered more of the failure surface.
- The thickness debit effect can be attributed to the following process: The loss in load carrying area due to cleavage-like cracking raises the stress level on the remaining intact surface which promotes additional cleavage. The deleterious effect of loss of intact area is greater for thinner specimens.

*High temperature low stress condition (982°C/248MPa):*

- The steady-state creep rate increased with decreasing specimen thickness. The time to reach 5% creep strain was reduced by 18% for the specimens with thickness

$h = 0.51$mm as compared with the specimens with $h = 3.18$mm.

- The time to rupture for the specimens with $h = 0.51$mm was 25% less than that for the specimens with $h = 3.18$mm but there was no systematic dependence of the strain to rupture on specimen thickness.
- Surface oxides formed. Spallation of the Ni-rich and mixed oxide layers and formation of adherent Al-rich oxide was observed. Cracks formed in the adherent oxide layer exposed metal but were arrested due to further oxidation.
- Oxidation of the uncoated specimens resulted in the formation of a $\gamma'$-precipitate free zone. The precipitate free zone underwent dynamic recrystallization resulting in the formation of subgrains.
- Void nucleation was observed throughout the specimen and particularly in the precipitate free zone.
- Finite element analysis of a constrained layered structure shows a near surface increase in stress triaxiality and a change in Lode parameter.
- A transition from homogeneous dimple fracture due to void nucleation, growth and coalescence to a mixed mode of void nucleation, growth and coalescence together with cleavage was observed with decreasing specimen thickness.

In summary the results show that, depending on temperature and stress magnitude, bulk and surface mechanisms can play a role in the thickness debit effect. This is also the case for room temperature plastic deformation with, depending on circumstances, geometrically necessary dislocations (a bulk effect) and/or source truncation and dislocation starvation (where surfaces are involved) leads to a size effect.

# CHAPTER 3

# POROSITY EVOLUTION IN A CREEPING SINGLE CRYSTAL

## 3.1. Introduction

The motivation for this study stems from experimental observations of creep deformation and failure of a nickel based single crystal superalloy in Chapter 2. Metallographic observations have shown that Ni-based single crystal superalloys contain micro voids formed during the solidification and homogenization processes as shown in Chapter 2 and in [39, 40]. A variety of experimental results, e.g. [9, 14, 10], have shown greater creep strain rates and reduced creep life for thinner specimens (but still larger than the micron scale at which size dependent plasticity effects come into play) than is predicted by current theories. This is termed the thickness debit effect and is typically attributed to some sort of surface damage as in [35, 36, 37]. Isothermal creep tests carried out on plate-like specimens of a PWA1484 nickel-based single crystal superalloy having various thicknesses and deformed at several stress levels and temperatures in [10] showed a thickness debit effect even at temperatures too low for there to be any significant effect of diffusion or environmental damage. Void growth was observed in Chapter 2 and played a role in the creep failure process.

The focus here is confined on analyzing void growth in a single crystal matrix using a unit cell model. Each unit cell contains a single initially spherical void. Isothermal conditions are assumed and the attention is confined to circumstances where diffusion effects have a negligible influence on void growth. Finite deformation finite element analyses are carried out using a rate dependent crystal plasticity constitutive relation accounting for both primary and secondary creep. One initial crystallographic orientation, as in the experiments in Chapter 2, and one initial void volume fraction is considered.

There is a large literature on cell models of porosity evolution aimed at understanding the micromechanics of ductile fracture and developing damage-type constitutive relations, e.g. [55, 56, 57, 58, 59, 61, 60, 62, 63, 64, 65, 66]. The initial focus was on relatively high values of stress triaxiality where the effect of the stress triaxiality (the ratio of the

first and second stress invariants) is dominant, for example [55, 56, 57, 58, 59, 61, 60, 62]. More recently, largely motivated by experiments of Bao and Wierzbicki [67], modeling the behavior at moderate and low values of stress triaxiality where the influence of the third stress invariant becomes more prominent has been receiving much attention, e.g. [63, 64, 65, 66]. These studies have been carried out for isotropic solids and for imposed loadings where the applied stress increases with time.

Hori and Nemat-Nasser [68] analyzed void growth and void collapse in a three dimensional single crystal matrix with an isolated ellipsoidal void under far field tensile and compressive loading. Void growth in two dimensional single crystals have been analyzed in [69, 70, 71, 72]. Kysar et al. [72] used anisotropic slip line theory to obtain stress and deformation state around a cylindrical void in a single crystal oriented such that plane strain conditions are admitted from three effective in-plane slip systems. Void growth in a single crystal was analyzed in [73, 74, 75, 76, 77, 78, 80, 79] using a three dimensional cell model based crystal plasticity calculation that accounts for void-void interaction effects. Wan et al. [74] and Yu et al. [80] analyzed the effect of the Lode parameter (a parameter that characterizes the third invariant of stress) on void growth. It has been shown that the effect of the Lode parameter can depend on crystallographic orientation [80] and void shape (crack-like or pore-like) [75]. All these results were obtained for monotonically increasing loading conditions.

For creep loading, Budiansky et al. [81] analyzed deformation of an isolated void in an isotropic viscous material under a wide range of remote axisymmetric stress states. Based on the void growth model in [81], Dennis [82] (also see [83]) carried out an analysis of an isolated void in a single crystal and proposed a failure criterion for the initiation of a micro-crack from a void surface in terms of a critical inelastic strain in the vicinity of the void which in turn was linked to a stress triaxiality dependent critical relative void volume fraction. Finite deformation analyses of the effect of void interaction and void shape change on the void growth rate in an isotropic power law creeping matrix were carried out in [84]. For polycrystalline metals, grain boundary diffusion often plays a significant role, see for

example [86, 85]. However, for single crystals this mechanism is ruled out and, at least for one of the temperatures tested in Chapter 2, 760°C, bulk diffusion also was not significant so that dislocation creep was the main deformation mechanism.

The analyses here is focused on the role of stress state on deformation and void growth in ductile single crystals in the dislocation creep regime. The possible role of porosity evolution in the thickness debit effect is also explored. Two types of imposed loading has been considered: in one case the applied true stress (force/current area) is fixed in time while in the other case the applied nominal stress (force/initial area) is time independent. For both type of loading, stress states corresponding to various values of triaxiality (the ratio of hydrostatic to Mises effective stress) and various values of the Lode parameter has been analyzed. The true stress conditions are of interest for constitutive modeling while the experiments in Chapter 2 were carried out under fixed nominal stress loading conditions. Results are presented for the effects of stress triaxiality and Lode parameter on the evolution of the void volume fraction and the void shape as well as for the effect of void shape changes on the stress state that develops in the crystal matrix. A part of results have been reproduced from the work of Srivastava [87] for the sake of completion.

## 3.2. Problem Formulation

### 3.2.1. Unit Cell

Three dimensional cell model analyses of a single initially spherical void in a face centered cubic (fcc) crystal under tensile creep loading conditions has been carried out. Cartesian tensor notation is used. The unit cell is initially cubic with side lengths $2a_0$ ($-a_0 \leq x_i \leq a_0$) and the initial void radius is $r_0$. The main loading direction is parallel to the $x_1$ axis and the edges initially parallel to the $x_2$ and $x_3$ axes are required to remain parallel to their respective axes during deformation which is consistent with, but stronger than, symmetry about these axes. The fcc crystal is taken to be in a $< 001 >$ (cube) orientation. Symmetry about each axis is assumed so that only 1/8 of the unit cell needs to be analyzed numerically. The configuration analyzed is shown in Fig. 3.1.

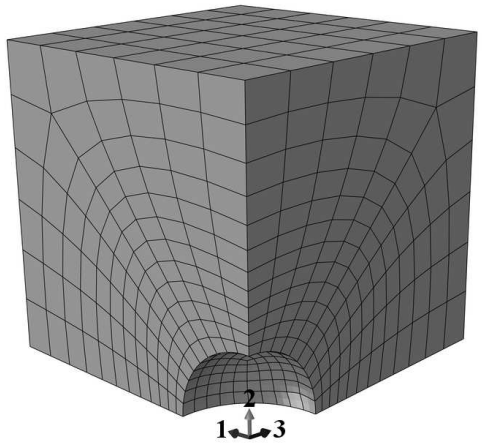


FIGURE 3.1. A finite element mesh of 1/8 of the unit cell with a spherical void in the center.

Overall tractions are imposed on the faces of the unit cell with the requirement that the cell boundaries remain planes aligned with the coordinate axes and shear free so that

$$
\begin{aligned}
u_1(a_0, x_2, x_3) &= U_1(t)\ ,\ T_2(a_0, x_2, x_3) = 0\ ,\ T_3(a_0, x_2, x_3) = 0 \\
u_2(x_1, a_0, x_3) &= U_2(t)\ ,\ T_1(x_1, a_0\, x_3) = 0\ ,\ T_3(x_1, a_0, x_3) = 0 \\
u_3(x_1, x_2, a_0) &= U_3(t)\ ,\ T_1(x_1, x_2, a_0) = 0\ ,\ T_2(x_1, x_2, a_0) = 0
\end{aligned} \tag{6}
$$

The symmetry conditions on the remaining surfaces are

$$
\begin{aligned}
u_1(0, x_2, x_3) &= 0\ ,\ T_2(0, x_2, x_3) = 0\ ,\ T_3(0, x_2, x_3) = 0 \\
u_2(x_1, 0, x_3) &= 0\ ,\ T_1(x_1, 0, x_3) = 0\ ,\ T_3(x_1, 0, x_3) = 0 \\
u_3(x_1, x_2, 0) &= 0\ ,\ T_1(x_1, x_2, 0) = 0\ ,\ T_2(x_1, x_2, 0) = 0
\end{aligned} \tag{7}
$$

The macroscopic true (or Cauchy) stresses, $\Sigma_i$, are defined as

$$
\begin{aligned}
\Sigma_1 &= \frac{1}{a_2 a_3} \int_0^{a_2} \int_0^{a_3} \sigma_{11}(a_1, x_2, x_3) dx_2 dx_3 \\
\Sigma_2 &= \frac{1}{a_1 a_3} \int_0^{a_1} \int_0^{a_3} \sigma_{22}(x_1, a_2, x_3) dx_1 dx_3 \\
\Sigma_3 &= \frac{1}{a_1 a_2} \int_0^{a_1} \int_0^{a_2} \sigma_{33}(x_1, x_2, a_3) dx_1 dx_2
\end{aligned} \tag{8}
$$

where $a_1 = a_0 + U_1$, $a_2 = a_0 + U_2$ and $a_3 = a_0 + U_3$.

The time histories of the displacements $U_1(t)$, $U_2(t)$ and $U_3(t)$ in Eq. (6) are determined by the analysis. In one set of calculations, true stresses $\Sigma_1$, $\Sigma_2$ and $\Sigma_3$ are applied and remain constant throughout the deformation history. In the other set of calculations, the value of the nominal (or engineering) stress, $N_1$ is required to remain fixed throughout the deformation history. The macroscopic nominal stress $N_i$ are related to the values of $\Sigma_i$ in Eq. (8) by

$$N_1 = \frac{a_2 a_3}{a_0^2}\Sigma_1 \ , \ N_2 = \frac{a_1 a_3}{a_0^2}\Sigma_2 \ , \ N_3 = \frac{a_1 a_2}{a_0^2}\Sigma_3 \tag{9}$$

For both types of imposed loading, the macroscopic true stresses follow a proportional stress history that is given by

$$\Sigma_2 = \rho_2 \Sigma_1 \qquad \Sigma_3 = \rho_3 \Sigma_1 \tag{10}$$

where $\rho_2$ and $\rho_3$ are constants. Hence, with $N_1$ fixed and proportional true stress values imposed $N_2$ and $N_3$ generally vary during the loading history. However, for uniaxial tensile loading $\Sigma_2 = \Sigma_3 = 0$, the values of $N_2$ and $N_3$ also remain zero. Here, calculations with $\Sigma_1$ fixed (and by Eq. (10) $\Sigma_2$ and $\Sigma_3$ fixed) are termed constant true stress calculations while calculations with $N_1$ fixed are termed constant nominal stress calculations even though $N_2$ and $N_3$ typically vary during the deformation history.

The macroscopic effective stress, $\Sigma_e$, and the macroscopic hydrostatic stress (positive in tension), $\Sigma_h$, are given by

$$\Sigma_e = \frac{1}{\sqrt{2}}\sqrt{(\Sigma_1 - \Sigma_2)^2 + (\Sigma_2 - \Sigma_3)^2 + (\Sigma_3 - \Sigma_1)^2} \qquad \Sigma_h = \frac{1}{3}(\Sigma_1 + \Sigma_2 + \Sigma_3) \tag{11}$$

The stress triaxiality $\chi$, is then defined as

$$\chi = \frac{\Sigma_h}{\Sigma_e} = \frac{\sqrt{2}}{3}\frac{1 + \rho_2 + \rho_3}{\sqrt{(1 - \rho_2)^2 + (\rho_2 - \rho_3)^2 + (\rho_3 - 1)^2}} \tag{12}$$

The stress triaxiality involves the first and second stress invariants, the influence of the third invariant is assessed via the Lode parameter, $L$, which is

$$L = \frac{2\Sigma_2 - \Sigma_1 - \Sigma_3}{\Sigma_1 - \Sigma_3} = \frac{2\rho_2 - 1 - \rho_3}{1 - \rho_3} \tag{13}$$

3.2.2. Constitutive Relation

The crystal plasticity constitutive implementation is based on the UMAT due to Huang [88] as modified by Kysar [89]. This crystal constitutive formulation follows that in Asaro and Needleman [90] (see also Asaro [91]). The deformation gradient, $\mathbf{F}$, is written as

$$\mathbf{F} = \mathbf{F}^* \cdot \mathbf{F}^P \tag{14}$$

where $\mathbf{F}^*$ is due to stretching and rotation of the crystal lattice and $\mathbf{F}^P$ is due to crystallographic slip. In the reference, undeformed lattice, the slip direction and the slip plane normals of the crystal are denoted by $\mathbf{s}^{(\alpha)}$ and $\mathbf{m}^{(\alpha)}$, respectively. In the current configuration these are given by

$$\mathbf{s}^{(\alpha)*} = \mathbf{F}^* \cdot \mathbf{s}^{(\alpha)} \qquad \mathbf{m}^{(\alpha)*} = \mathbf{m}^{(\alpha)} \cdot \mathbf{F}^{*-1} \tag{15}$$

Differentiating Eq. (14) with respect to time and combining terms gives

$$\dot{\mathbf{F}} \cdot \mathbf{F}^{-1} = \mathbf{D} + \mathbf{\Omega} = (\mathbf{D}^* + \mathbf{\Omega}^*) + (\mathbf{D}^p + \mathbf{\Omega}^p) \tag{16}$$

Here, $(\mathbf{D}^* + \mathbf{\Omega}^*)$ are, respectively, the elastic rate of stretching and spin tensors, and the plastic rate of stretching, $\mathbf{D}^p$, and spin tensors, $\mathbf{\Omega}^p$, are given by

$$\mathbf{D}^p = \sum_\alpha \dot{\gamma}^{(\alpha)} \mathbf{P}^{(\alpha)} \qquad \mathbf{\Omega}^p = \sum_\alpha \dot{\gamma}^{(\alpha)} \mathbf{W}^{(\alpha)} \tag{17}$$

where $\dot{\gamma}^{(\alpha)}$ is the rate of shearing on slip system $\alpha$, and

$$\mathbf{P}^{(\alpha)} = \frac{1}{2}(\mathbf{s}^{(\alpha)*}\mathbf{m}^{(\alpha)*} + \mathbf{m}^{(\alpha)*}\mathbf{s}^{(\alpha)*}) \qquad \mathbf{W}^{(\alpha)} = \frac{1}{2}(\mathbf{s}^{(\alpha)*}\mathbf{m}^{(\alpha)*} - \mathbf{m}^{(\alpha)*}\mathbf{s}^{(\alpha)*}) \tag{18}$$

Elastic strains are presumed small so that the lattice Jaumann rate of Cauchy stress, $\hat{\boldsymbol{\sigma}}^*$, is given by

$$\hat{\boldsymbol{\sigma}}^* = \dot{\boldsymbol{\sigma}} + \boldsymbol{\sigma} \cdot \mathbf{\Omega}^* - \mathbf{\Omega}^* \cdot \boldsymbol{\sigma} = \mathbf{L} : \mathbf{D}^* - \boldsymbol{\sigma}(\mathbf{I} : \mathbf{D}^*) \tag{19}$$

with $\mathbf{L}$ being the tensor of elastic moduli. The corotational stress rate on axes rotating with the material, $\hat{\boldsymbol{\sigma}}$, is given by

$$\hat{\boldsymbol{\sigma}} = \dot{\boldsymbol{\sigma}} - \mathbf{\Omega} \cdot \boldsymbol{\sigma} + \boldsymbol{\sigma} \cdot \mathbf{\Omega} \tag{20}$$

The difference between $\hat{\boldsymbol{\sigma}}^*$ and $\hat{\boldsymbol{\sigma}}$ is

$$\hat{\boldsymbol{\sigma}}^* - \hat{\boldsymbol{\sigma}} = \sum_\alpha \dot{\gamma}^{(\alpha)} \mathbf{W}^{(\alpha)} \cdot \boldsymbol{\sigma} - \sum_\alpha \dot{\gamma}^{(\alpha)} \boldsymbol{\sigma} \cdot \mathbf{W}^{(\alpha)} \tag{21}$$

Defining

$$\boldsymbol{\psi}^{(\alpha)} = \mathbf{W}^{(\alpha)} \cdot \boldsymbol{\sigma} - \boldsymbol{\sigma} \cdot \mathbf{W}^{(\alpha)} \tag{22}$$

and using Eqs. (16) and (17) with Eqs. (19) and (21) gives

$$\hat{\boldsymbol{\sigma}} = (\mathbf{L} - \boldsymbol{\sigma}\mathbf{I}) : \mathbf{D} - \sum_\alpha \dot{\gamma}^{(\alpha)} \mathbf{R}^{(\alpha)} \tag{23}$$

since $\mathbf{I} : \mathbf{D}^* = \mathbf{I} : \mathbf{D}$ and with

$$\mathbf{R}^{(\alpha)} = \mathbf{L} : \mathbf{P}^{(\alpha)} + \boldsymbol{\psi}^{(\alpha)} \tag{24}$$

The Schmid resolved shear stress is given by

$$\tau^{(\alpha)} = \mathbf{m}^{(\alpha)*} \cdot \boldsymbol{\sigma} \cdot \mathbf{s}^{(\alpha)*} = \boldsymbol{\sigma} : \mathbf{P}^{(\alpha)} \tag{25}$$

The material modeled is a PWA1484 Ni based single crystal superalloy [10]. The elastic constants have cubic symmetry and are specified by $C_{11} = 283.3$GPa, $C_{12} = 197.5$GPa and $C_{44} = 112$GPa. The active slip systems for this material at the temperature of interest are not known. Given the fcc-based crystal structure, potentially active slip system are taken to be the twelve primary octahedral slip systems $\{111\} < 110 >$.

Slip is assumed to obey Schmid's law so that the slip rate $\dot{\gamma}^{(\alpha)}$ only depends on the current stress state through the slip-system resolved shear stress $\tau^{(\alpha)}$. The crystals exhibit both primary and secondary creep, both of which are represented in terms of power law relations. The initial value of slip on each slip system is taken to be zero and the evolution of slip on slip system $\alpha$ is given by

$$\dot{\gamma}^{(\alpha)} = \left\{ (1-\beta)\dot{\gamma}_M \left| \frac{\tau^{(\alpha)}}{\tau_0} \right|^M + \beta \dot{\gamma}_N \left| \frac{\tau^{(\alpha)}}{\tau_0} \right|^N \right\} \mathrm{sgn}(\tau) \tag{26}$$

where $\tau_0$, $\dot{\gamma}_M$, $\dot{\gamma}_N$, $M$ and $N$ are material constants and $\beta$ evolves as

$$\dot{\beta} = \frac{1}{t_0} (\beta_{ss} - \beta) \tag{27}$$

with the initial condition that $\beta = 0$ at $t = 0$ and with $\beta_{ss}$ the steady state value of $\beta$ and $t_0$ a time constant that governs the transition from primary to secondary creep. This particular form was fit to the experimental constant applied nominal stress creep data of Seetharaman and Cetel [10] for the sheet specimen of thickness 3.18mm at a test temperature of 760°C and an applied nominal stress of $N_1 = 758$MPa. The material parameters used in Eq. (26) are $\tau_0 = 245$MPa, $\dot{\gamma}_M = 1.04 \times 10^{-6}\text{s}^{-1}$, $\dot{\gamma}_N = 1.53 \times 10^{-9}\text{s}^{-1}$, $M = 1$ and $N = 5$ and the parameters used in Eq. (27) are $\beta_{ss} = 0.998$ and $t_0 = 1.35 \times 10^4$s. Figure 3.2 shows the experimental tensile creep curve of $\Delta l/l_0$ versus time, where $l_0$ is the initial length of the specimen gauge section and $\Delta l$ is the change in length of the gauge section with the loading applied in the $< 001 >$ direction. For comparison purposes two computed curves for a fully dense material using the parameter values given above are also plotted: one with constant nominal stress and one with constant true stress. The computed and experimental curves with a constant nominal stress are in good agreement until the time at which the onset of tertiary creep occurs in the experiment.

### 3.2.3. Numerical Method

The calculations are carried out using the commercial finite element code ABAQUS standard, version 6.x [54], and using a UMAT based on that developed by Huang [88] and Kysar [89] modified for the creep relation in Section 3.2.2. In all calculations the initial values of $\Sigma_i$ are prescribed so that $\Sigma_1 \geq \Sigma_2 \geq \Sigma_3$. In the calculations with fixed values of the true stresses $\Sigma_i$ the values of the stress triaxiality $\chi$ and the Lode parameter $L$ directly remain fixed. In the calculations with the nominal stress $N_1$ kept fixed the values of $\Sigma_i$ vary with time so that the fixed stress ratio in Eq. (10) needs to be maintained by controlling the tractions acting on the surfaces of the unit cell. At each time step the values of $\Sigma_i$ are calculated from Eq. (8). The proportional history of stress state is monitored using the URDFIL user subroutine in ABAQUS standard 6.x [54] and any deviation in the proportionality constants $\rho_2$ and $\rho_3$ given in Eq. (10) is counteracted by applying an additional uniform traction on the corresponding surfaces using the DLOAD user subroutine. The variations in $\rho_2$ and $\rho_3$ were kept within 0.1% over the course of the loading history. This procedure enables the

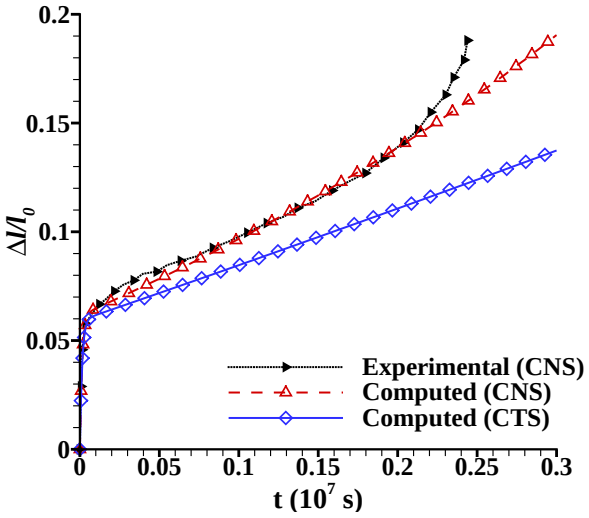


FIGURE 3.2. Comparison of experimental and computed tensile creep curves for a single crystal of orientation $< 001 >$. The experimental creep curve is obtained for constant nominal stress creep loading and the computed creep curves are shown for both constant nominal stress (CNS) and constant true stress (CTS) creep loading. The computed curves are for a fully dense material.

responses under prescribed true stress conditions and under prescribed nominal stress $N_1$ to be compared for fixed $\chi$ and $L$ values. Prescribed proportional true stressing is of interest for formulating a phenomenological damage-type constitutive relation while the interest in prescribed nominal stressing is because that was the condition in the creep experiments in Chapter 2.

A finite element mesh with C3D20H (20-node hybrid solid elements with quadratic displacement interpolation and linear pressure interpolation) elements is shown in Fig. 3.1. Most calculations are carried out using 916 elements. Convergence was assessed by carrying out calculations with 1250 and 1786 elements for a representative case with $\chi = 2$, $L = -1$ and fixed $\Sigma_i$. The time to reach an effective creep strain of $E_e = 0.3$ was used to assess convergence. For meshes with 916, 1250 and 1786 elements the time to $E_e = 0.3$ was $7.2889 \times 10^6$s, $7.2887 \times 10^6$s and $7.2885 \times 10^6$s respectively. The time steps were varied during the course of the deformation history so that $\Delta\gamma^{(\alpha)}$ on any slip system never exceeded 0.001.

3.3. Numerical Results

The unit cell analyzed, see Fig. 3.1, has $r_0/a_0 = 0.267$ which gives a void volume fraction of $(4\pi r_0^3/3)/(2a_0)^3 = 0.01$. This is selected based on the distribution of porosity in the material in Chapter 2. The average void volume fraction in a Ni-based single crystal material is generally low but these pores are confined in interdendritic areas [39, 40], hence leading to a higher local void volume fraction. This initial void volume fraction and the crystal properties are the same in all calculations. The loading axis in the creep tests of [10] is within 10° of $< 001 >$ and $< 001 >$ tensile loading is prescribed in the calculations here.

In the first time step values of $\Sigma_i$ are specified that give a value of $\Sigma_e$ in Eq. (11) of 750MPa and the crystal response is taken to be elastic. Calculations are carried out for six values of the stress triaxiality $\chi$, Eq. (12), and, for each value of $\chi$, for five values of the Lode parameter $L$, Eq. (13). The stress state is taken to be such that $\Sigma_1 \geq \Sigma_2 \geq \Sigma_3$. The expressions Eq. (12) and Eq. (13) together with $\Sigma_e = 750$MPa in Eq. (11) constitute a set of quadratic equations for the stress components. For a given value of $\chi$ and $L$ two sets of values of the stress components are obtained only one of which satisfies the specified inequality constraint. For example, with $\chi = 3$ and $L = -1$ the two solutions are: $\Sigma_1 = 2750$MPa, $\Sigma_2 = 2000$MPa, $\Sigma_3 = 2000$MPa; and $\Sigma_1 = 1750$MPa, $\Sigma_2 = 2500$MPa, $\Sigma_3 = 2500$MPa. A reordering of the second of these solutions to $\Sigma_1 = 2500$MPa, $\Sigma_2 = 2500$MPa, $\Sigma_3 = 1750$MPa corresponds to $\chi = 3$, $L = 1$. Similarly for other combinations of $\chi$ and $L$, the solution that does not satisfy the inequality constraint gives stress components with the same value of $\chi$ and a sign change in $L$ when the stresses are reordered.

The initial stress states together with the values of stress triaxiality $\chi$, the Lode parameter $L$ and the parameter $\omega$ introduced by Nahshon and Hutchinson [65] are shown in Table. 3.1. The value of $\omega$ is given by

$$\omega = 1 - \left(\frac{27 J_3}{2\Sigma_e^3}\right)^2 \tag{28}$$

where, $J_3 = (\Sigma_1 - \Sigma_h)(\Sigma_2 - \Sigma_h)(\Sigma_3 - \Sigma_h)$ with $\Sigma_e$ and $\Sigma_h$ defined in Eq. (11).

For each initial stress state, the creep response under both constant true stress and

constant nominal stress loading is analyzed. For constant true stress creep $\Sigma_i$ remains constant through out loading history whereas for constant nominal stress creep $\Sigma_i$ varies during the deformation history.

Table 3.1: Initial values of the stress triaxiality $\chi$, the Lode parameter $L$, the parameter $\omega$ and the initial macroscopic stresses $\Sigma_i$.

| $\chi$ | L | $\omega$ | $\Sigma_1$ (MPa) | $\Sigma_2$ (MPa) | $\Sigma_3$ (MPa) |
|---|---|---|---|---|---|
| 3.00 | -1.00 | 0.00 | 2750.00 | 2000.00 | 2000.00 |
| 3.00 | -0.50 | 0.44 | 2735.36 | 2111.33 | 1903.31 |
| 3.00 | 0.00 | 1.00 | 2683.01 | 2250.00 | 1816.99 |
| 3.00 | 0.50 | 0.44 | 2596.69 | 2388.68 | 1764.64 |
| 3.00 | 1.00 | 0.00 | 2500.00 | 2500.00 | 1750.00 |
| 2.00 | -1.00 | 0.00 | 2000.00 | 1250.00 | 1250.00 |
| 2.00 | -0.50 | 0.44 | 1985.36 | 1361.33 | 1153.31 |
| 2.00 | 0.00 | 1.00 | 1933.01 | 1500.00 | 1066.99 |
| 2.00 | 0.50 | 0.44 | 1846.69 | 1638.68 | 1014.64 |
| 2.00 | 1.00 | 0.00 | 1750.00 | 1750.00 | 1000.00 |
| 1.00 | -1.00 | 0.00 | 1250.00 | 500.00 | 500.00 |
| 1.00 | -0.50 | 0.44 | 1235.36 | 611.32 | 403.31 |
| 1.00 | 0.00 | 1.00 | 1183.01 | 750.00 | 316.99 |
| 1.00 | 0.50 | 0.44 | 1096.69 | 888.68 | 264.64 |
| 1.00 | 1.00 | 0.00 | 1000.00 | 1000.00 | 250.00 |
| 0.75 | -1.00 | 0.00 | 1062.50 | 312.50 | 312.50 |
| 0.75 | -0.50 | 0.44 | 1047.86 | 423.82 | 215.81 |
| 0.75 | 0.00 | 1.00 | 995.51 | 562.50 | 129.49 |

*Continued on next page*

Table 3.1 – *Continued from previous page*

| $\chi$ | L | $\omega$ | $\Sigma_1$ (MPa) | $\Sigma_2$ (MPa) | $\Sigma_3$ (MPa) |
|---|---|---|---|---|---|
| 0.75 | 0.50 | 0.44 | 909.19 | 701.18 | 77.14 |
| 0.75 | 1.00 | 0.00 | 812.50 | 812.50 | 62.50 |
| 0.50 | -1.00 | 0.00 | 875.00 | 125.00 | 125.00 |
| 0.50 | -0.50 | 0.44 | 860.36 | 236.32 | 28.31 |
| 0.50 | 0.00 | 1.00 | 808.01 | 375.00 | -58.01 |
| 0.50 | 0.50 | 0.44 | 721.69 | 513.68 | -110.36 |
| 0.50 | 1.00 | 0.00 | 625.00 | 625.00 | -125.00 |
| 0.33 | -1.00 | 0.00 | 750.00 | 0.00 | 0.00 |
| 0.33 | -0.50 | 0.44 | 735.36 | 111.32 | -96.69 |
| 0.33 | 0.00 | 1.00 | 683.01 | 250.00 | -183.01 |
| 0.33 | 0.50 | 0.44 | 596.69 | 388.68 | -235.36 |
| 0.33 | 1.00 | 0.00 | 500.00 | 500.00 | -250.00 |

The parameter $\omega$ defined in [65], lies in the range $0 \leq \omega \leq 1$, with $\omega = 0$ for all axisymmetric stress states and $\omega = 1$ for all stress comprised of a pure shear stress plus a hydrostatic contribution. Thus, $\omega$ does not distinguish between the imposed stress states corresponding to $L = -1$ and $L = 1$. In the following the Lode parameter $L$ has been used to characterize the imposed stress state.

The macroscopic effective creep strain is defined as

$$E_e = \frac{\sqrt{2}}{3}\sqrt{(E_1^c - E_2^c)^2 + (E_2^c - E_3^c)^2 + (E_3^c - E_1^c)^2} \tag{29}$$

where

$$E_1^c = \ln\left(\frac{a_1}{\tilde{a}_1}\right) \qquad E_2^c = \ln\left(\frac{a_2}{\tilde{a}_2}\right) \qquad E_3^c = \ln\left(\frac{a_3^c}{\tilde{a}_3}\right) \tag{30}$$

where $\tilde{a}_i$ is the value of $a_i$ after the first elastic step.

The calculations proceed with fixed true or nominal stresses until one of the following conditions is met: (i) 90% loss of ligament in either the $x_2$ or the $x_3$ direction; (ii) void collapse, $f/f_0 \approx 0$; or (iii) achieving an effective macroscopic creep strain $E_e = 1.5$.

3.3.1. Evolution of the Macroscopic Creep Strain

The time history of $E_e$ for stress triaxiality values $\chi = 3$ and 0.33 and values of the Lode parameter ranging from $-1$ to 1 is shown in Fig. 3.3 under constant true stress creep loading conditions. The transition from primary to secondary (steady state) creep, governed by the evolution of $\beta$ in Eq. (27), is essentially independent of the stress triaxiality and occurs at $t \approx 1.0 \times 10^5$s. This corresponds to $E_e = 0.061$ for $\chi = 3$ and $L = -1$ and to $E_e = 0.058$ for $\chi = 0.33$ and $L = -1$. The steady state effective creep strain rate, $\dot{E}_{ss}$, is essentially independent of the value of the Lode parameter and is almost same for $\chi \leq 0.75$ as for the fully dense material in Fig. 3.2 which is $\dot{E}_{ss} = 0.235 \times 10^{-7}\text{s}^{-1}$. For greater values of the stress triaxiality $\chi$ there is an effect of $\chi$ on $\dot{E}_{ss}$ with $\dot{E}_{ss}$ increasing to $\dot{E}_{ss} = 0.438 \times 10^{-7}\text{s}^{-1}$ for $\chi = 3$.

For $\chi = 3$, Fig. 3.3(a), there is a transition to tertiary creep which, as will be shown subsequently, is associated with necking of the ligament between adjacent voids. Under the creep loading conditions here the increase in strain rate accompanying necking occurs less abruptly than for the nearly rate independent materials in [58]. Here, and subsequently, the time at which tertiary creep begins has been identified as the earliest time at which $\dot{E}_e/\dot{E}_{ss} \geq 5$. With this definition, in Fig. 3.3(a) where $\chi = 3$ the onset of tertiary creep occurs at $t \approx 0.32 \times 10^7$s. For $\chi = 0.33$, Fig. 3(b), tertiary creep does not occur over the range computed and the calculations are terminated either when void collapse occurs or when $E_e = 1.5$. The maximum quantitative difference in Fig. 3(b) is between the curves for $L = \pm 1$ and $L = 0$.

The values $L = -1$ and $L = 1$ both correspond to axisymmetric stress states. For a fully dense single crystal, the number of slip systems with the same magnitude of resolved shear stress is the same and the number of systems with positive and negative values of resolved shear stress are also the same although the particular slip systems differ. For

example, with $\chi = 0.33$, there are four slip systems with $\tau = 306.3$MPa and four with $\tau = -306.3$MPa for both $L = 1$ and $L = -1$. Nevertheless, the responses with a void differ with different values of Lode parameter in particular at low values of stress triaxiality.

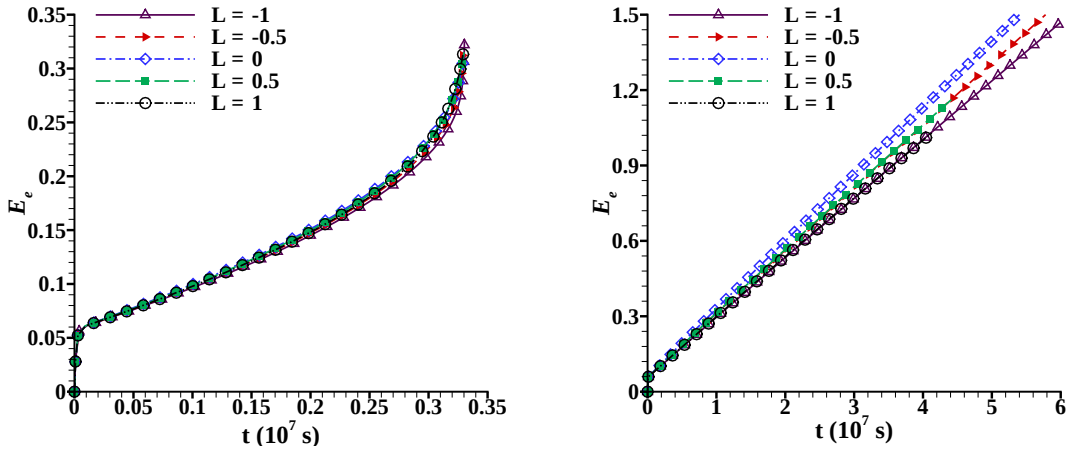


(a) (b)

FIGURE 3.3. Time histories of macroscopic effective creep strain $E_e$ under constant true stress creep loading for stress triaxiality (a) $\chi = 3$ and (b) $\chi = 0.33$.

The variation of macroscopic effective strain, $E_e$, with time for all six values of stress triaxiality, $\chi$, is shown in Fig. 3.4 for $L = -1$ and $L = 1$. Whether or not tertiary creep occurs depends on the value of the stress triaxiality, $\chi$, and, if it does occur, the value of time at which it occurs also depends on the value of $\chi$. For $L = -1$ to $L = 1$ tertiary creep (as defined here) occurs for $\chi \geq 2$ and does not occur for $\chi \leq 0.75$. The value of $\chi$ at which the transition from tertiary creep occurring to no tertiary creep (over the time computed) does depend on the value of the Lode parameter $L$. For example, tertiary creep occurs for $\chi = 1$ and $L = -1$ at $t = 3.5 \times 10^7$s but for $\chi = 1$ and $L = 1$, $\dot{E}_e/\dot{E}_{ss}$ remains less than 5 till 90% loss of ligament. The curves for $\chi = 0.5$ and $\chi = 0.33$ with $L = 1$ in Fig. 4(b) are terminated before $E_e = 1.5$ because void collapse occurred as will be shown in Section 3.3.2.

The results for constant nominal stress creep loading are shown in Figs. 3.5 and 3.6. Under constant nominal stress creep loading, $\Sigma_1$ increases with the deformation induced

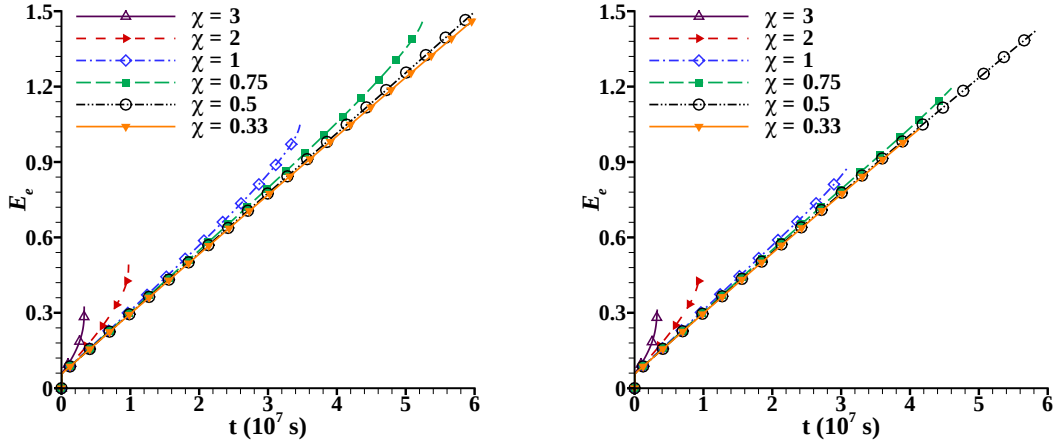


(a) (b)

FIGURE 3.4. Time histories of macroscopic effective creep strain $E_e$ under constant true stress creep loading for Lode parameter (a) $L = -1$ and (b) $L = 1$.

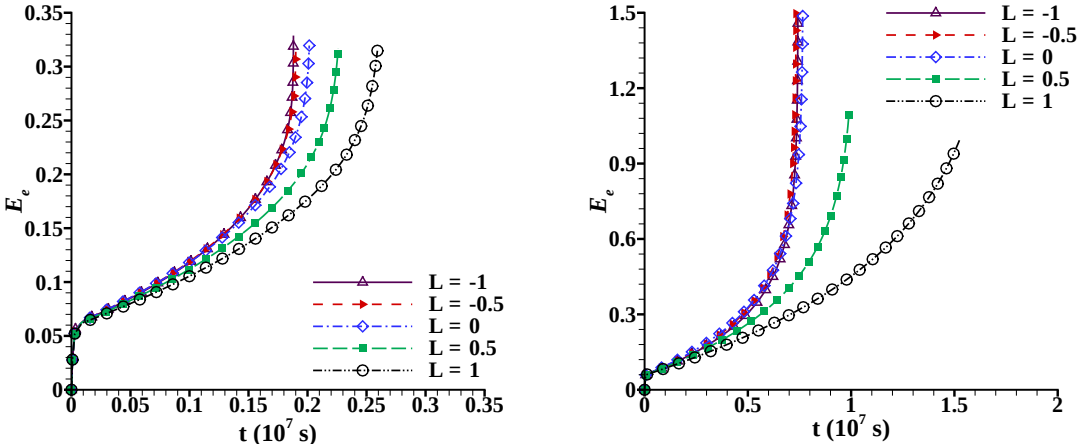


(a) (b)

FIGURE 3.5. Time histories of macroscopic effective creep strain $E_e$ for constant nominal stress creep loading for stress triaxiality (a) $\chi = 3$ and (b) $\chi = 0.33$.

reduction in cross sectional area perpendicular to the $x_1$ direction, see Eq. (9). In contrast to the results for constant true stress creep loading, there is a significant dependence on the

value of the Lode parameter $L$ for all values of $\chi$ in Fig. 3.5. In particular, the responses for $L = -1$ and $L = 1$ differ significantly. The steady state effective strain rate for a fully dense material with constant $N_1$ in Fig. 3.2 is $\dot{E}_{ss} = 0.355 \times 10^{-7} s^{-1}$. There is a small effect of porosity (with $f_0 = 0.01$) on the steady state creep rate for $\chi = 0.33$; $\dot{E}_{ss} = 0.395 \times 10^{-7}\text{s}^{-1}$ for $\chi = 0.33$ and $L = -1$. As for constant $\Sigma_i$ loading, the effect of porosity on the secondary creep rate increases with increasing stress triaxiality being $0.61 \times 10^{-7}\text{s}^{-1}$ for $\chi = 3$ and $L = -1$. At all values of $\chi$, the effect of porosity is greater under constant $N_1$ (nominal stress) loading than it is under constant $\Sigma_i$ (true stress) loading.

Under constant nominal stress loading, tertiary creep occurs for $\chi = 0.33$. and there is a significant dependence on the values of Lode parameter $L$ for all values of $\chi$. For example, in Fig. 5(b) where $\chi = 0.33$ the onset of tertiary creep, i.e. $\dot{E}_e/\dot{E}_{ss} > 5$, takes place at $t = 0.642 \times 10^7$s for $L = -1$ while it occurs at $t = 1.482 \times 10^7$s for $L = 1$. This sensitivity to the value of the Lode parameter decreases with increasing values of $\chi$. For example, in Fig. 5(a) where $\chi = 3$, the onset of tertiary creep occurs at $t = 0.178 \times 10^7$s for $L = -1$ and at $t = 0.243 \times 10^7$s for $L = 1$. The analyses for $L = 0.5$ and $L = 1$ with $\chi = 0.33$ are terminated after void collapse.

The time histories of the effective creep strain $E_e$ for six values of $\chi$ and for Lode parameter values of $L = -1$ and $L = 1$ are shown in Fig. 3.6. For all values of the Lode parameter, a decreasing value of stress triaxiality decreases the creep rate and delays the onset of tertiary creep for $\chi \geq 1$. For $\chi \leq 1$ with $L = -1$, Fig. 3.6(a), the secondary creep rate, $\dot{E}_{ss} \approx 0.4 \times 10^{-7}\text{s}^{-1}$, and the onset of tertiary creep are nearly independent of $\chi$. With $L = -1$ and $\chi \leq 1$ the onset of tertiary creep occurs at $t \approx 0.6 \times 10^7$s. For $L = -1$ the calculations for $\chi = 0.5$ and 0.33 were terminated at $E_e = 1.5$.

In Fig. 3.6(b) where $L = 1$ $\dot{E}_{ss} \approx 0.35 \times 10^{-7}\text{s}^{-1}$ for $\chi \leq 1$. The onset of tertiary creep takes place at $t = 1.34 \times 10^7$s for $\chi = 1$ and at $t = 1.48 \times 10^7$s for $\chi = 0.33$. With $L = 1$ void collapse occurs for $\chi = 0.5$ and 0.33.

One feature common to all cases analyzed, both constant true stress loading and constant nominal stress loading, and for values of the Lode parameter, is that for values

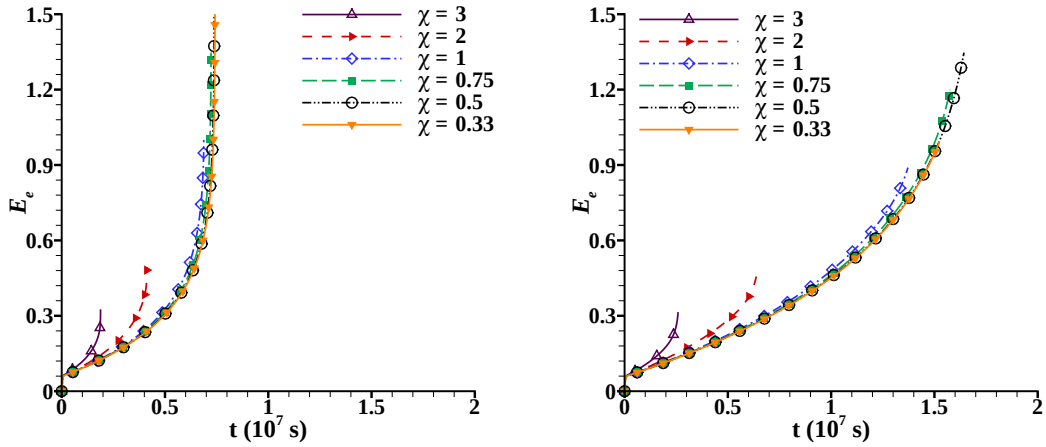


(a) (b)

FIGURE 3.6. Time histories of macroscopic effective creep strain ($E_e$) under constant nominal stress creep loading for Lode parameter (a) $L = -1$ and (b) $L = 1$.

of the stress triaxiality $\chi \geq 0.75$ the analyses were terminated due to necking down of the ligament between adjacent voids giving a 90% loss of ligament.

3.3.2. Evolution of the Porosity

The void volume fraction is defined as $f = (V_{\text{cell}} - V_M)/V_{\text{cell}}$ where $V_{\text{cell}}$ is the current cell volume and $V_M$ is the current material volume (the small elastic volume change is neglected) and $f/f_0$ is the relative void volume fraction.

Plots of relative void volume fraction $f/f_0$ versus time are shown in Fig. 3.7 for $\chi = 3$. The evolution of porosity is essentially independent of the value of the Lode parameter $L$ for constant true stress creep loading, Fig. 3.7(a), whereas there is a significant dependence on $L$ for constant nominal stress creep loading, Fig. 3.7(b). The void growth rate initially decreases as creep deformation shifts from primary to secondary creep, reaches a minimum value and then increases. The onset of tertiary creep (as defined here) is marked by the circles in Fig. 3.7. The earliest onset of tertiary creep in Fig. 3.7(b) occurs for $L = -1$ and the latest for $L = 1$. Due to the increase in imposed true stress under constant nominal stress loading the void growth rate is greater at any given time than that under constant

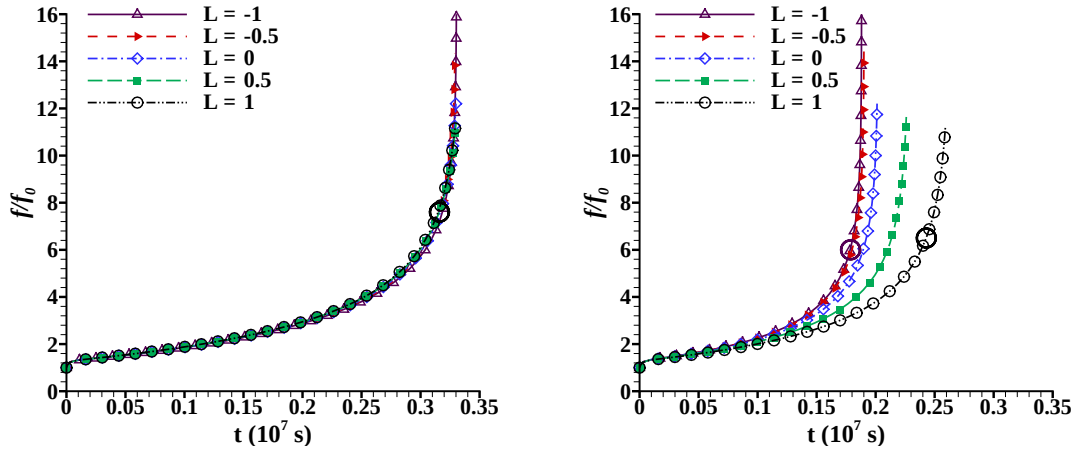


FIGURE 3.7. Plots of relative void volume fraction $f/f_0$ versus time $t$ for stress triaxiality $\chi = 3$. (a) Constant true stress creep loading. (b) Constant nominal stress creep loading. The onset of tertiary creep for the Lode parameter values $L = -1$ and $L = 1$ is marked by a circle.

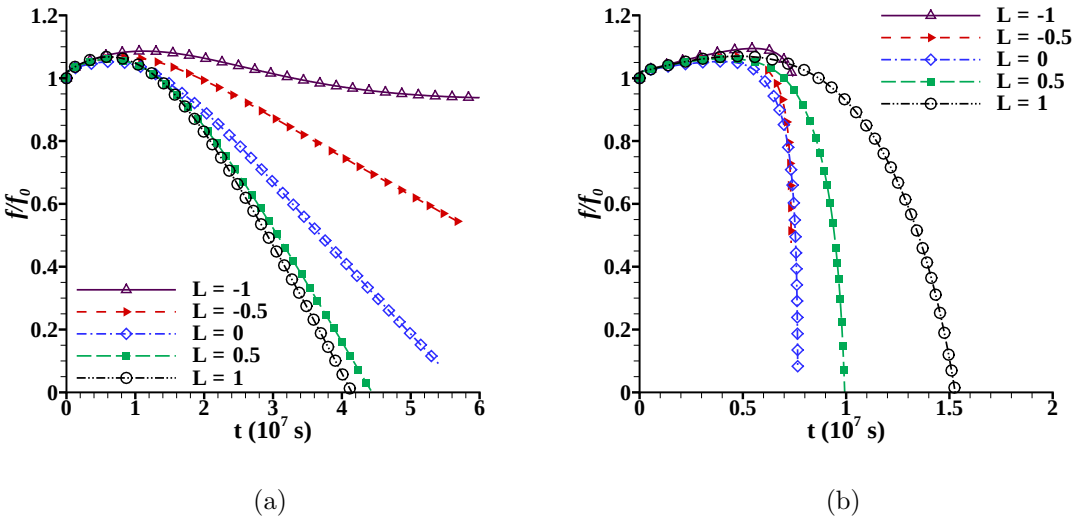


FIGURE 3.8. Plots of relative void volume fraction $f/f_0$ versus time $t$ for stress triaxiality $\chi = 0.33$. (a) Constant true stress creep loading. (b) Constant nominal stress creep loading.

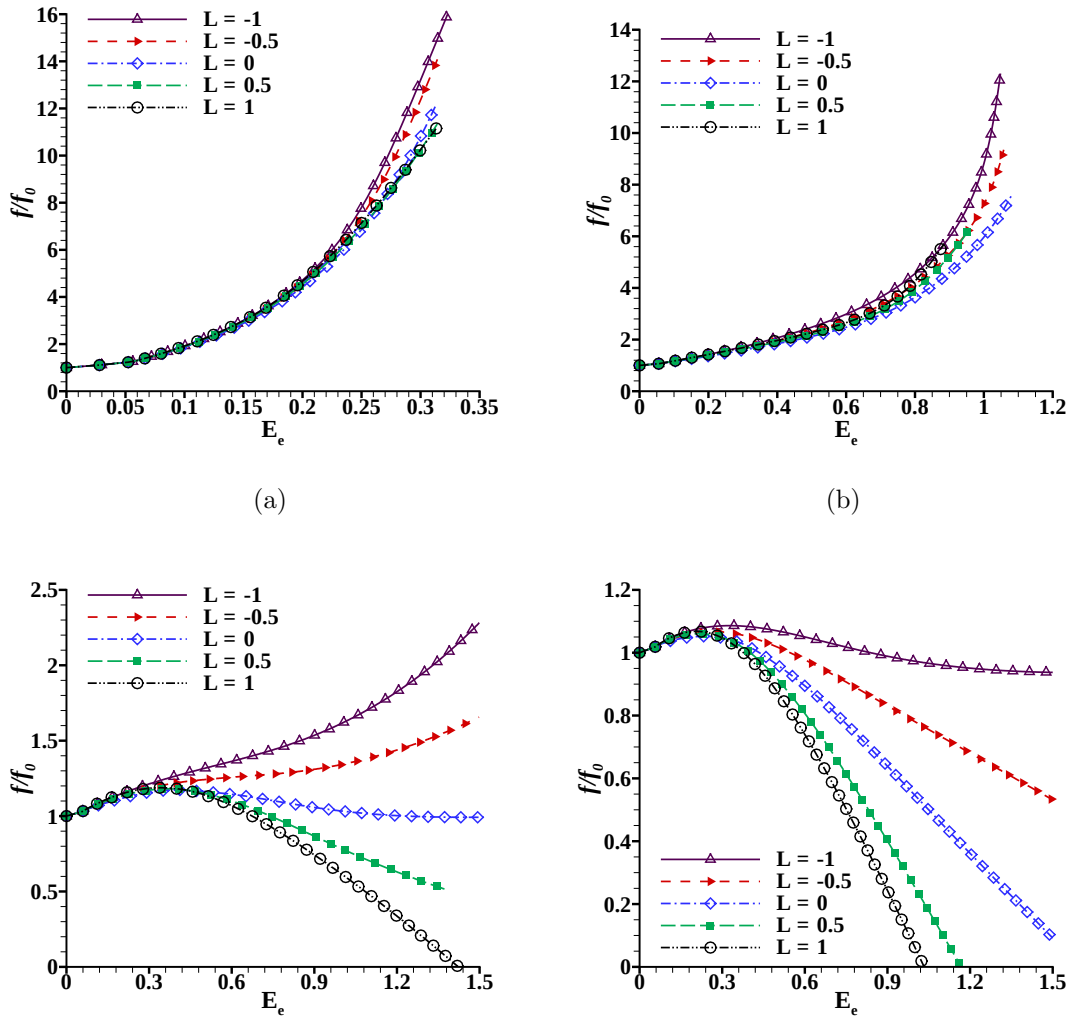


FIGURE 3.9. Evolution of the relative void volume fraction $f/f_0$ as a function of the macroscopic effective creep strain $E_e$ for various values of the stress triaxiality. (a) $\chi = 3$. (b) $\chi = 1$. (c) $\chi = 0.5$. (d) $\chi = 0.33$. The data is for constant true stress creep loading. However, the calculations for constant nominal stress loading give nearly the same results.

true stress loading.

With $\chi = 0.33$ in Fig. 3.8 the relative void volume fraction decreases after an initial increase. In Fig. 3.8 $f/f_0$ is independent of the value of the Lode parameter in the early stages of deformation. For $\chi = 0.33$ and $L = -1$ in Fig. 3.8(a), the relative void volume

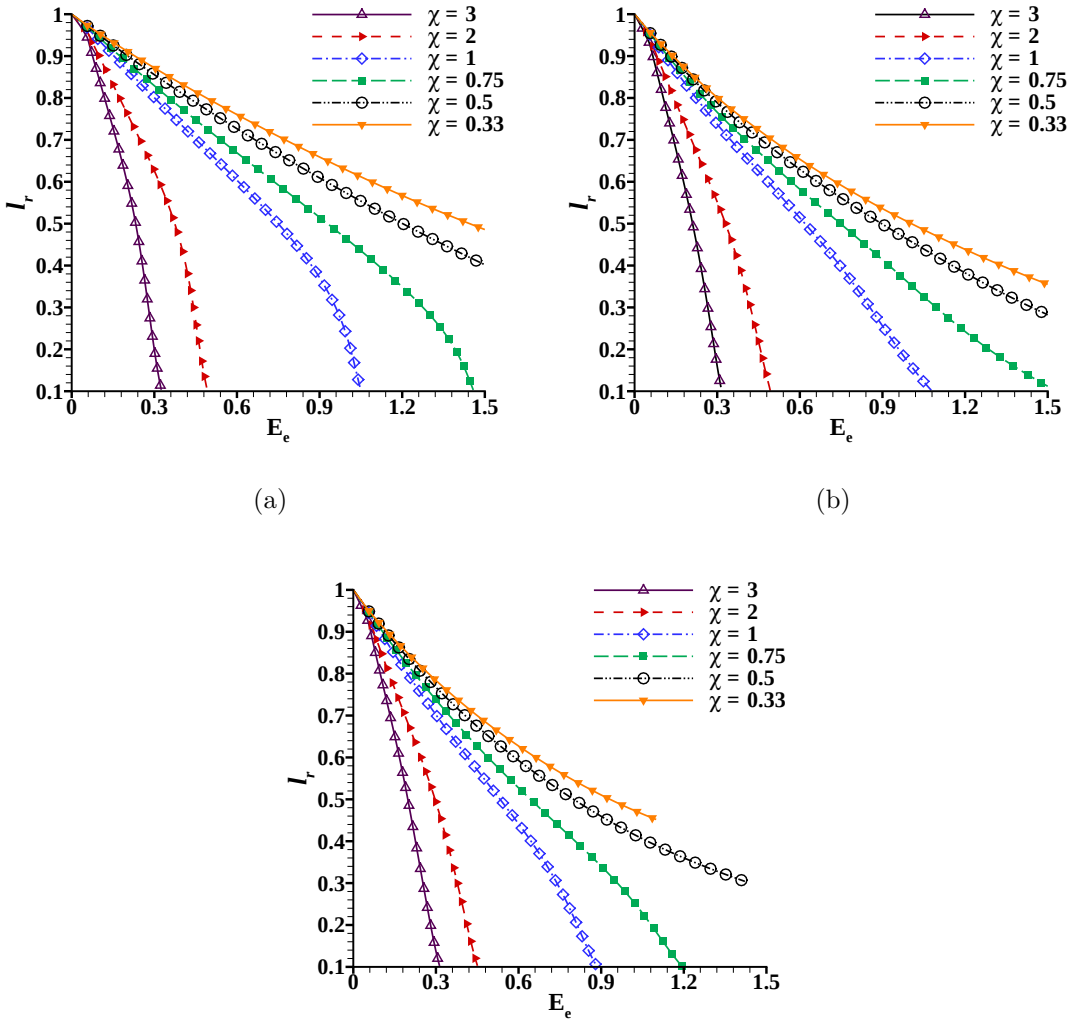


FIGURE 3.10. Progressive loss of relative ligament ($l_r = (a_3 - r_3)/(\tilde{a}_3 - \tilde{r}_3)$) in the $x_3$ direction under constant true stress creep loading for various values of the stress triaxiality $\chi$ and the Lode parameter $L$. (a) $L = -1$. (b) $L = 0$. (c) $L = 1$.

fraction increases to a maximum with $f/f_0 > 1$ and saturates to $f/f_0 \approx 1$. For $\chi = 0.33$ and $L \geq -0.5$, after an initial increase $f/f_0$ decreases. As seen in Fig. 3.8 $f/f_0$ decreases more rapidly under constant nominal stress loading than under constant true stress loading. This because under constant nominal stress loading the increasing value of $\Sigma_1$ leads to an increasing strain rate. The rate of decrease of porosity increases with increasing Lode

parameter value under constant true stress loading whereas the rate decreases with increasing value of Lode parameter under constant nominal stress loading. For instance the time to void collapse, $f/f_0 \approx 0$, under constant true stress loading for $L = -0.5$ is $t \approx 4.5 \times 10^7$s and for $L = 1$ it is $t \approx 4.2 \times 10^7$s. Under constant nominal stress loading the time to void collapse for $L = -0.5$ is $t \approx 1 \times 10^7$s and for $L = 1$ it is $t \approx 1.5 \times 10^7$s.

Figure 3.9 shows plots of relative void volume fraction $f/f_0$ versus macroscopic effective creep strain $E_e$ under constant true stress loading. The corresponding results for constant nominal stress loading are nearly the same. For a given stress triaxiality the evolution of relative void volume fraction with respect to macroscopic creep deformation is not strongly dependent on the type of creep loading. Hence, the main difference between these two types of imposed loading is the different strain histories that occur. The evolution of the void volume fraction, at least with the constitutive description used here, mainly depends on the creep strain.

The evolution of porosity with $E_e$ shows no dependence on the values of the Lode parameter until a stress triaxiality dependent value of $E_e$ is reached. The value of $E_e$ at which $f/f_0$ depends on the value of the Lode parameter increases with decreasing stress triaxiality until $\chi = 0.75$. For example, for $\chi = 3$ the effect of Lode parameter value is seen for $E_e > 0.25$ and for $\chi = 1$ the effect of Lode parameter value is seen for $E_e > 0.6$. On the other hand, the dependence of $f/f_0$ on the Lode parameter value for $\chi = 0.5$ occurs for $E_e > 0.3$ and for $\chi = 0.33$ this dependence can be seen for $E_e > 0.2$.

In Fig. 3.9(a) for $\chi = 3$, $f/f_0$ is maximum for $L = -1$ and minimum for $L = 1$ at any given $E_e > 0.25$. Whereas for $\chi = 1$ in Fig. 3.9(b) the value of $f/f_0$ is smaller for $L = 0$ than that for $L = \pm 1$ at any given $E_e > 0.6$. For void growth in an fcc single crystal unit cell analyses under monotonically increasing load for $\chi \geq 1$ Wan et al. [74] and Yu et al. [80] observed a smaller void volume fraction at a given strain for $L = 0$ than for $L = \pm 1$. The analyses here for $\chi \geq 0.75$ were terminated after 90% loss of ligament and $f/f_0$ at the end of these analyses was found to decrease with increasing Lode parameter value. For example, for $\chi = 1$ and $L = -1$, 0 and 1, $f/f_0 = 12.3$, 7.6 and 5.71 at the end of the analysis,

respectively.

In Fig. 3.9(c) where $\chi = 0.5$ void collapse occurs for $L = 1$ while in Fig. 3.9(d) where $\chi = 0.33$ void collapse occurs for both $L = 1$ and $L = 0.5$. In other cases in Figs. 3.9(c) and 3.9(d) the calculations were terminated on reaching $E_e = 1.5$. These results indicate that void collapse for $\chi = 0.5$ and 0.33, or an evolution toward void collapse can occur, for some values of Lode parameter at low values of stress triaxiality even when $\chi$ is positive. Budiansky et al. [81] found void collapse in an axisymmetric analysis of an isolated void in a power law creeping solid with $\Sigma_1 = \Sigma_2$ and $\Sigma_3/\Sigma_1 = -0.5$ which corresponds to $\chi = 0.33$ and $L = 1$.

The necking down between voids is quantified in terms of the evolution of the smallest ligament length between voids. For values of stress triaxiality and Lode parameter analyzed here the $x_3$ direction is the direction with the minimum value of $\Sigma_i$, Table. 3.1, and necking down between voids generally takes place in the $x_3$ direction. With $L = -1$ $\Sigma_2 = \Sigma_3$ and there is simultaneous necking down in the $x_2$ and $x_3$ directions. However, the ligament length in the $x_3$ direction can still be used to characterize necking.

The relative ligament length in this direction is $l_r = (a_3 - r_3)/(\tilde{a}_3 - \tilde{r}_3)$, where $a_3$ and $r_3$ are, respectively, the current cell length and void size along the $x_3-$axis, and $\tilde{a}_3$ and $\tilde{r}_3$ are, respectively, the cell length and void size along the $x_3-$axis after the first elastic step. Plots of $l_r$ versus $E_e$ are shown in Fig. 3.10 for $L = -1$, 0 and 1. The results in Fig. 3.10 are shown for constant true stress creep loading. The results for constant nominal stress creep loading are nearly the same.

There is a significant difference between the responses with $L = -1$ and $L = 1$ in Fig. 3.10. With $L = -1$, $\Sigma_2 = \Sigma_3$ there is simultaneous necking in the ligament between adjacent voids in the $x_2$ and $x_3$ directions, whereas for $L = 1$, $\Sigma_1 = \Sigma_2$ necking between adjacent voids only occurs in the $x_3$ direction. The necking down of the ligament is mainly responsible for the rapid increase in void growth rate during tertiary creep regime for $\chi = 3$ and 2 and, as discussed, void growth occurs more slowly with strain with increasing Lode parameter value.

Figure 3.10 shows the variation of the ligament length $l_r$ for $L = -1$, 0 and 1. For $\chi \geq 0.75$ $l_r$ decreases to $\approx 0.1$ for $E_e \leq 1.5$. There is, as expected, a strong dependence on the strain to reach $l_r = 0.01$ on the value of $\chi$. For $L = -1$ a strain is reached at which $l_r$ decreases rapidly for $\chi \geq 0.75$. For $L = 1$ this rapid decrease only occurs for $\chi = 3$ and 2 although there is an increases in the magnitude of the slope for $\chi = 1$ and (slightly) for $\chi = 0.75$. For $L = 0$, there is only a rapid increase in slope magnitude for $\chi = 3$ and 2; for $\chi = 1$ and 0.75 there is a very gradual decrease in ligament which is associated with the Poisson area reduction with increasing strain rather than a more or less abrupt necking down. The results show that under creep loading there is a gradual transition depending on stress triaxiality and Lode parameter between necking down between voids that can occur at relatively small strains and a gradual decrease in distance between voids that requires much larger strains.

### 3.3.3. Evolution of the Void Shape

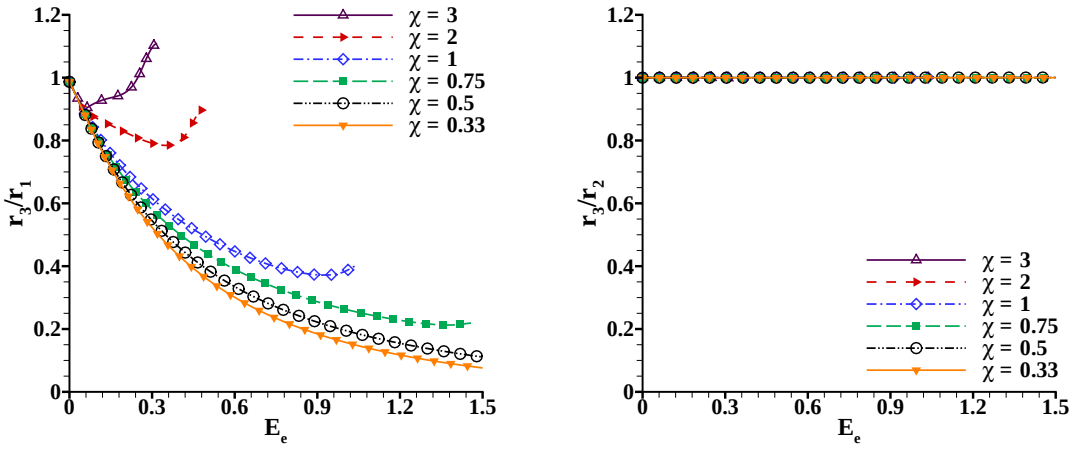


(a) (b)

FIGURE 3.11. Evolution of void radius ratios for various values of the stress triaxiality $\chi$ with the Lode parameter $L = -1$. (a) $r_3/r_1$. (b) $r_3/r_2$.

The void shape has been characterized by two ratios: (i) $r_3/r_1$ where $r_1$ is the void size along the $x_1-$axis and $r_3$ is the void size along the $x_3-$axis; and (ii) $r_3/r_2$ where $r_2$ is

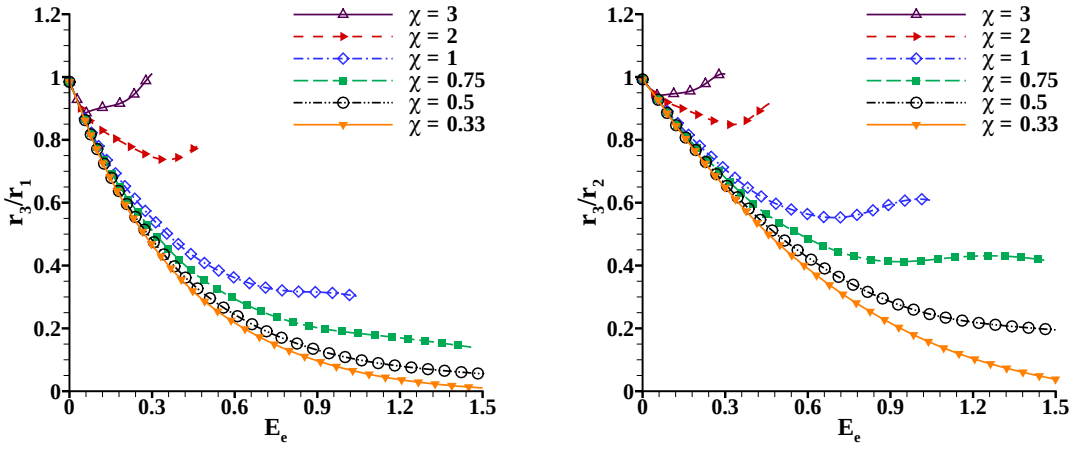


(a) (b)

FIGURE 3.12. Evolution of void radius ratios for various values of the stress triaxiality $\chi$ with the Lode parameter $L = 0$. (a) $r_3/r_1$. (b) $r_3/r_2$.

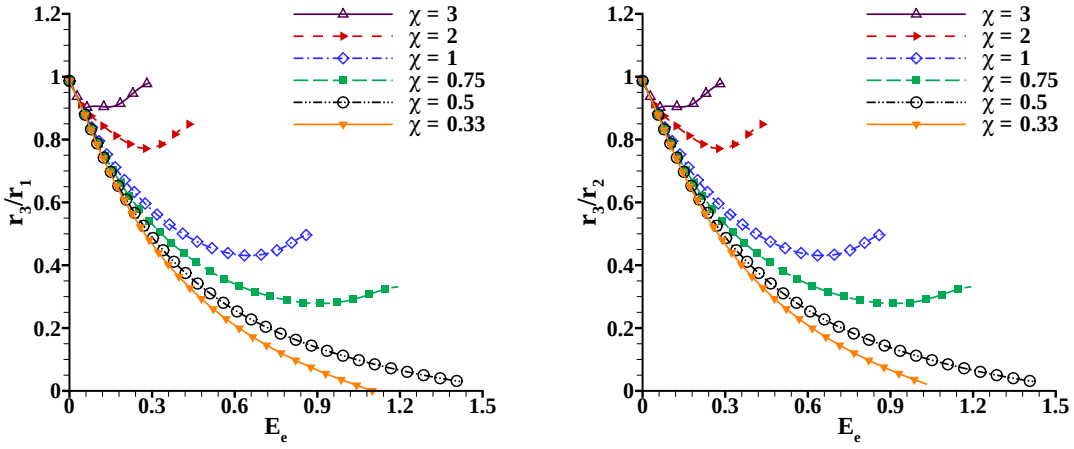


(a) (b)

FIGURE 3.13. Evolution of void radius ratios for various values of the stress triaxiality $\chi$ with the Lode parameter $L = 1$. (a) $r_3/r_1$. (b) $r_3/r_2$.

the void size along the $x_2-$axis. The ratio $r_3/r_1$ gives the gives the ratio of the minimum cross sectional radius to that in the loading direction while $r_3/r_2$ is the ratio of the void sizes along the coordinate axes in the plane perpendicular to the loading direction.

Figure 3.11 shows the evolution of the radius ratios with effective creep strain $E_e$

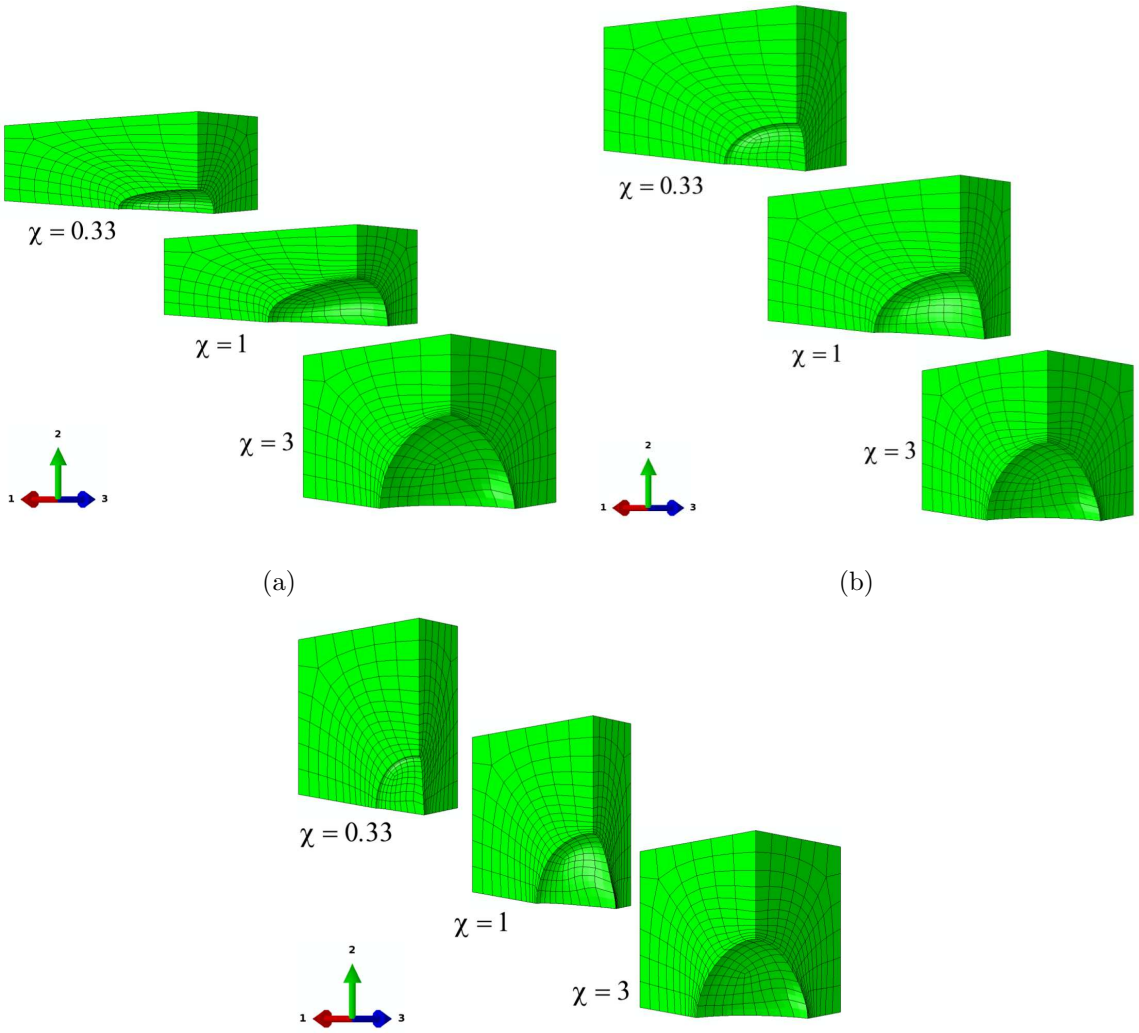


FIGURE 3.14. The void shape for various values of the Lode parameter for $\chi = 0.33$ at $E_e = 0.8$, $\chi = 1$ at $E_e = 0.8$ and $\chi = 3$ at $E_e = 0.3$. (a) $L = -1$. (b)$L = 0$. (c)$L = 1$.

for $L = -1$ and for constant true stress loading (the curves for both constant true stress and constant nominal stress loading are essentially identical). In Fig. 3.11(a) for $\chi \geq 2$ the ratio $r_3/r_1$ initially decreases and then increases indicating the necking down of the ligament between adjacent voids. For $\chi = 1$ there is an increase in $r_3/r_1$ just before the calculation is terminated at $E_e \approx 1$. For smaller values of $\chi$ the value of $r_3/r_1$ monotonically decreases during the deformation history so that the void becomes prolate.

The value of the Lode parameter $L = -1$ corresponds to an axisymmetric state of stress, $\Sigma_1 > \Sigma_2 = \Sigma_3$, with the $x_1-$axis being the symmetry axis. The radius ratio $r_3/r_2$ remains close to unity, Fig. 3.11(b), for the range of stress triaxiality values analyzed in the current work. However the void cross sectional shape depends on the stress triaxiality value. For $\chi = 0.33$, where void interaction effects are not significant and no necking down of the ligament between voids occurs, the cross sectional shape remains essentially circular. For $\chi = 3$ necking down of the ligament in the $x_2$ and $x_3$ directions leads to a rapid increase in the void radii in these directions whereas void growth in off-axis directions is less so that the void cross section is not circular. The largest deviation from a circle occurs at 45°. For example, the radius ratio $r_{45°}/r_3 = 0.91$ for $\chi = 3$ and $L = -1$ at an effective creep strain $E_e = 0.322$ which is when there is 90% loss of ligament.

For $L = 0$, Fig. 3.12, $r_3/r_1$ and $r_3/r_2$ decrease initially for $\chi \geq 2$ but then increase for $L = -1$. For $\chi = 1$ both radius ratios eventually level off while for $\chi = 0.5$ and 0.33 the void predominantly elongates in the $x_1$ direction which is the major stress axis. Both $r_3/r_1$ and $r_3/r_2$ approach zero with $\chi = 0.33$ indicating void collapse.

The trends for the variation of $r_3/r_1$ and $r_3/r_2$ for $L = 1$ in Fig. 3.13 are qualitatively similar to those for $L = 0$ in Fig. 3.12 but with void collapse occurring for $\chi = 0.5$ as well as for $\chi = 0.33$. For $\chi = 1$ and 0.75, the radius ratio $r_3/r_1$ increases due to void interaction effects in the $x_3$ direction, but the values remain well below unity over the entire deformation history leading to the formation of an oblate shape (largest cross section perpendicular to the direction of loading). Although not shown here $r_2/r_1 \approx 1$ throughout the deformation history for all values of stress triaxiality $\chi$ for $L = 1$ since the $x_3-$axis is the axis of symmetry, with $\Sigma_1 = \Sigma_2$. It is worth noting that for high stress triaxiality, $\chi \geq 2$, the void radii along all three axes increase for all Lode parameter values. For smaller values of $\chi$, $r_3$ decreases during the deformation history so that the void becomes oblate.

Figure 3.14 shows the void shapes obtained for $L = -1$, 0 and 1 and for three values of stress triaxiality $\chi = 3$, 1 and 0.33. For all values of $L$, the void is essentially spherical for $\chi = 3$. For $L = -1$ and $\chi = 1$ the void is a prolate spheroid (largest cross section along the

loading direction) and needle-like for $\chi = 0.33$. For $L = 0$ the void has a three dimensional shape for $\chi = 1$ and is like an elliptical crack for $\chi = 0.33$. For $L = 1$ the void evolves into a shape like that of an oblate spheroid for $\chi = 1$ and like that of a penny shaped crack for $\chi = 0.33$ (and also for $\chi = 0.5$ not shown here).

3.3.4. Stress Distributions

Distributions of $\sigma_{11}$ normalized by the current value of the applied stress $\Sigma_1$ for $\chi = 0.33$ are shown in Fig. 3.15. Figure 3.15(a) shows distributions for $L = -1$ and Fig. 3.15(b) for $L = 1$. The value of $\Sigma_1$ is constant throughout the deformation history under constant true stress loading but the value of $\Sigma_1$ changes with the change in cross sectional area under constant nominal stress loading. For both types of imposed loading the distributions of $\sigma_{11}/\Sigma_1$ at a given value of $E_e$ are nearly same and the distributions in Fig. 3.15 (and in Fig. 3.16) are for constant $\Sigma_1$ loading. The three values of strain shown in Fig. 3.15 are: (i) after the first elastic step, denoted as $E_e = 0$; (ii) at $E_e = 0.2$; and (iii) at $E_e = 0.8$.

After the first elastic step, $\Sigma_1 = 750$MPa and the maximum value of the stress ratio, $\sigma_{11}/\Sigma_1$ is 1.77. This maximum occurs at the circumference of the void on the $x_2 - x_3$ plane. For $L = -1$ at $E_e = 0.2$ in Fig. 15(a) the maximum value of $\sigma_{11}/\Sigma_1$ has decreased to 1.29. This corresponds to maximum $\sigma_{11} = 968$MPa under constant true stress loading but to 1189MPa under constant nominal stress loading since $\Sigma_1$ has increased to 922MPa due to the reduction in cross sectional area. At $E_e = 0.8$ the maximum stress concentration has shifted towards the tip of the void which has taken on a needle-like shape and the maximum value of $\sigma_{11}/\Sigma_1$ is 1.63. The maximum $\sigma_{11}$ under constant true stress creep loading is 1222MPa and is 2.69GPa under constant nominal stress loading since $\Sigma_1 = 1.65$GPa at $E_e = 0.8$.

For $\chi = 0.33$ and $L = 1$, Fig. 15(b), $\Sigma_1 = 500$MPa after the first elastic step and the peak value of $\sigma_{11}/\Sigma_1$ is 2.37 and occurs at the circumference of the void in $x_2 - x_3$ plane. Under constant nominal stress creep, $\Sigma_1$ increases to 554MPa at $E_e = 0.2$. At $E_e = 0.2$ the maximum stress concentration is still on the $x_2 - x_3$ plane but has slightly shifted away from the void surface and has increased to $\sigma_{11}/\Sigma_1 = 2.66$ so that the maximum values of

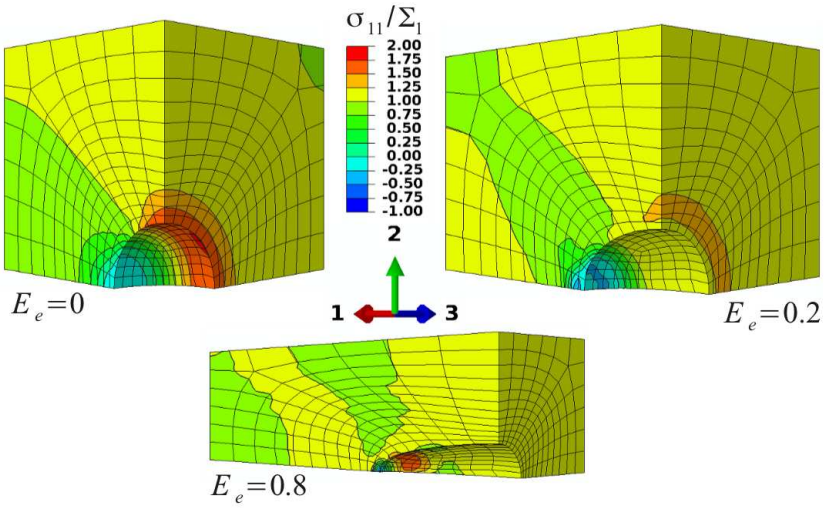


(a)

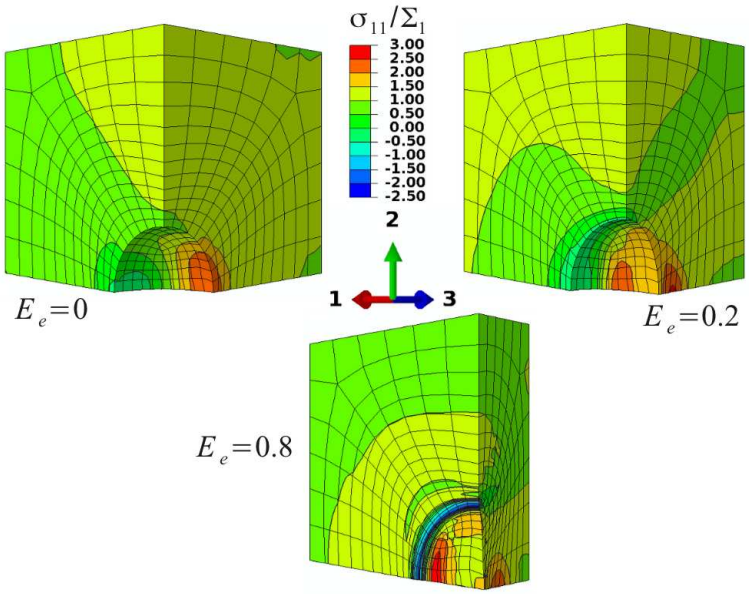


(b)

FIGURE 3.15. Distributions of normalized stress $\sigma_{11}/\Sigma_1$ after the first elastic step and at $E_e = 0.2$ and 0.8 under constant true stress creep loading for stress triaxiality $\chi = 0.33$. (a) $L = -1$. (b) $L = 1$.

$\sigma_{11}$ are 1.33GPa and 1.47GPa for constant true stress and constant nominal stress loading, respectively. For $\chi = 0.33$ and $L = 1$ at $E_e = 0.8$, void collapse has led to the void evolving into a shape like that of a penny shaped crack. The maximum value of $\sigma_{11}/\Sigma_1$ has increased to 2.79 and occurs near the tip. Under constant nominal stress loading $\Sigma_1 = 751$MPa at

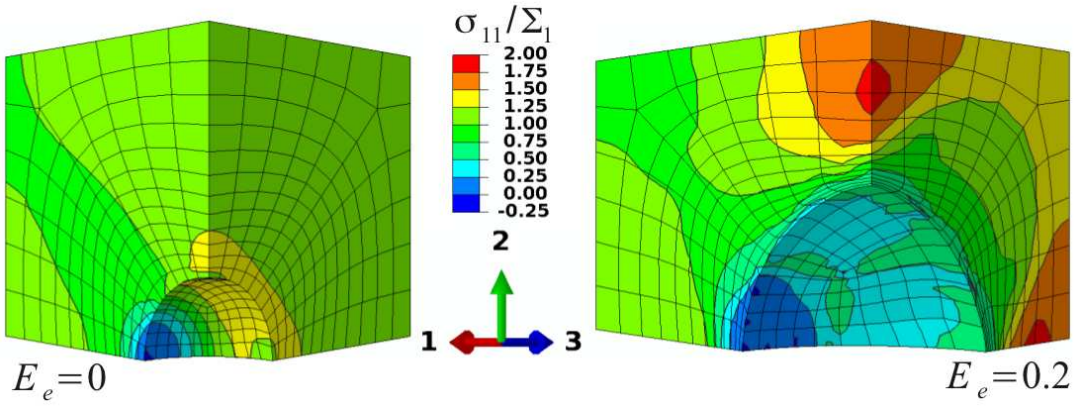


(a)

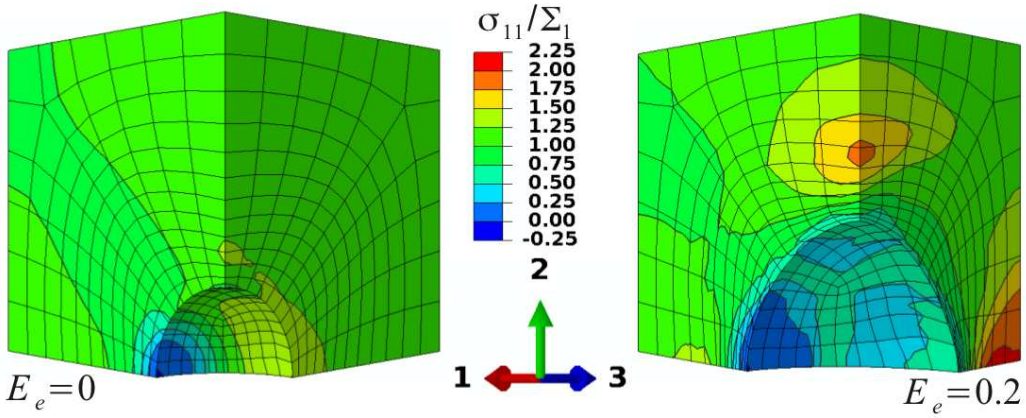


(b)

FIGURE 3.16. Distributions of normalized stress $\sigma_{11}/\Sigma_1$ after the first elastic step and at $E_e = 0.2$ under constant true stress creep loading for stress triaxiality $\chi = 3$. (a) $L = -1$. (b) $L = 1$.

$E_e = 0.8$ leading to $\sigma_{11} = 2.10$GPa at the point of maximum stress concentration while $\sigma_{11} = 1.40$GPa for constant true stress loading.

Distributions of $\sigma_{11}/\Sigma_1$ for $\chi = 3$ and $L = -1$ and $L = 1$ are shown in Fig. 3.16. At $E_e = 0$ $\Sigma_1 = 2750$MPa for $L = -1$ and $\Sigma_1 = 2500$MPa for $L = 1$; the maximum value, $\sigma_{11}/\Sigma_1 = 1.48$, is the same for both $L = -1$, Fig. 16(a), and $L = 1$, Fig. 16(b). At $E_e = 0.2$ the peak value of $\sigma_{11}/\Sigma_1$ is 1.83 for $L = -1$ and 2.11 for $L = 1$. For $L = -1$ the maximum value occurs at the center of the ligament between adjacent voids along both the $x_2$ and $x_3$ axes, Fig. 16(a). For $L = 1$ at $E_e = 0.2$ the maximum value is attained only along the $x_3$

axis. At $E_e = 0.2$ the maximum stress values are 5.0GPa for $L = -1$ and 5.3GPa for $L = 1$ under constant true stress loading.

## 3.4. Discussion

The analyses were motivated by the experiments in Chapter 2 on creep of a nickel based single crystal superalloy under uniaxial tensile loading. Since the aim is to model porosity evolution under creep, applied stresses (of one kind or another) are taken to be not varying with time. In the experiments the applied nominal stress was fixed so that type of loading was imposed in the calculations. However, for comparison purpose as well as to provide a basis for developing a phenomenological creep damage constitutive relation the response under time constant true stresses applied to the unit cell was also analyzed. This latter type of loading is analogous to the type of loading applied in the ductile fracture oriented studies. Although the imposed loading in the crystals tested in Chapter 2 was uniaxial tension, say due to constraint or inhomogeneity effects, the stress state can differ and, in particular, there can be regions of locally enhanced stress triaxiality as well as local variations in the value of the Lode parameter.

The calculations show that the time history of deformation and porosity depends on which type of creep loading is imposed. However, when the evolution of void volume fraction and shape is considered as a function of a measure of the overall creep strain, the results from the two types of imposed loading essentially coincide. This is not particularly surprising because (except for the effect of elasticity) the slip system resolved shear stress-resolved shear strain relation is history independent. If the slip system flow rule were strongly history dependent this conclusion would not hold. Another simplification in the crystal constitutive relation is that only self hardening has been considered. It is worth noting that with porosity evolution considered as a function of strain, the results exhibit many of the same qualitative features regarding the dependence on stress triaxiality and Lode parameter values as those found in ductile fracture oriented cell model studies.

In the analyses here one value of initial applied Mises effective stress was considered. The initial applied Mises effective stress is time independent under constant true stress creep

loading whereas it increases with time under constant nominal stress creep loading. In the absence of experimental creep data at different stress levels at 760°C for the material tested in Chapter 2 as well as in [10] a representative value for the secondary creep slip system power law exponent was used. Since, at least with this constitutive characterization, the creep response is essentially history independent and the void shape changes mainly occur when the material is in the secondary creep regime, it is expected that the macroscopic stress dependence will exhibit this same power law relation. Additional parameter studies are needed to determine the orientation dependence of the porosity evolution. The results of such analyses together with the constant true stress results obtained here could provide the background for developing a phenomenological constitutive relation using a framework such as in [92].

The Lode parameter was used to characterize the role of the third invariant of the applied stress. Another parameter that could be used for that purpose is the parameter $\omega$ in Nahshon and Hutchinson [65] which has the convenient feature that it lies between zero and one. The value of $\omega$ is zero for all axisymmetric stress states. The value of the Lode parameter can be 1 or $-1$ for an axisymmetric stress state (two of the applied stresses on the unit cell equal). The three dimensional analyses of void growth in the current work showed that significantly different void evolution histories are possible for $L = 1$ and $L = -1$ because the results depend on which plane contains the two equal stresses.

Budiansky et al. [81] found that an isolated initially spherical void in an isotropic matrix under power law creep for high stress triaxiality tends to become a prolate spheroid for stress ratios giving $L = -1$ whereas it tends to become an oblate spheroid for stress ratios giving $L = 1$. Here, for those loading conditions the same shape evolution occurs until void interaction effects come into play and the void aspect ratio then tends to increase and three dimensional void growth is observed. Similar void interaction effects were seen in [84] for an initially spherical void in an isotropic axisymmetric ($L = -1$) unit cell under power law creep at high stress triaxiality. For uniaxial tension with $\chi = 0.33$ and $L = -1$, Budiansky et al. [81] found that the void predominantly elongates in the loading direction

leading to a needle-like shape. Whereas for $\chi = 0.33$ and $L = 1$ the void collapses forming a penny-shaped crack. In the cell model calculations here at low stress triaxiality values void interaction effects are not dominant and the void shape in the analyses here evolves as in [81].

With reducing thickness of the sheet specimens it was found that local cleavage played a significant role in the observed creep rupture process whether environmental effects were dominant or not. The analyses here suggest that the high local stresses that develop in the ligament between voids could precipitate cleavage which would lead to an abrupt loss of load carrying area. This then would increase the stress on the remaining load carrying material and so act to precipitate further cleavage. This loss of area would be more damaging for thinner cross-sections. This could account for a thickness debit effect in Ni-based single crystal superalloys in circumstances where surface damage effects do not come into play.

## 3.5. Summary and Conclusions

Finite deformation finite element analyses of void growth in an fcc crystal under isothermal creep loading conditions were carried out. The slip system constitutive relation modeled primary and secondary creep. A unit cell was analyzed for crystals with a $< 001 >$ orientation and with a fixed initial void volume fraction of 0.01. The effect of stress triaxiality values (the ratio of mean normal true stress to Mises effective stress) between 0.33 and 3 and Lode parameter values between $-1$ and 1 was considered for both constant applied true stress loading and for constant applied nominal stress loading. For both types of loading proportional true stress ratios were maintained. The results show that:

- For fixed values of the stress triaxiality and Lode parameter, the mode of creep loading (constant applied true stress or constant applied nominal stress) has a significant effect on the time histories of the macroscopic effective creep strain and the void volume fraction. This dependence is more pronounced at low values of the stress triaxiality.
- The effect of imposed loading type stems from the loading mode dependence of the macroscopic effective creep strain. The dependence of the void volume fraction and

shape evolution on the macroscopic effective creep strain is independent of whether constant true stress or constant nominal stress creep loading is applied. The main features of this dependence are similar to the observations in previous cell model analyses of void growth under monotonically increasing loading.

- There is no significant effect of the value of the Lode parameter at high values of the stress triaxiality. At low values of the stress triaxiality the evolution of void volume fraction (including whether or not void collapse occurs) and the void shape evolution can be strongly dependent on the Lode parameter value.
- Due to void growth and the change in void shape the local stress magnitude in the void vicinity generally increases with time. For low values of the stress triaxiality, stress concentration factors exceeding 2.5 were found.
- A possibility, for certain materials, is that locally high stresses could initiate cleavage before void coalescence occurs. The associated loss of stress carrying capacity would be more pronounced for thinner specimens and this could lead to a thickness debit effect.

# CHAPTER 4

# VOID GROWTH VERSUS VOID COLLAPSE IN A CREEPING SINGLE CRYSTAL

## 4.1. Introduction

The studies here are largely motivated by the experimental observations in Chapter 2. In Chapter 2, it was found that porosity evolution played a significant role in the creep rupture processes. The microstructural analysis of these creep tested specimens revealed nucleation of cracks from isolated voids and coalescence of closely spaced voids. Finite element analyses in Chapter 2 indicated that observed microstructural changes near the specimen surface at high temperatures would give rise to local changes in the stress triaxiality and Lode parameter values.

The evolution of porosity plays an important role in the processing of porous materials as well as in fracture processes at room temperature and at elevated temperatures. Depending on the stress state, the void distribution and the temperature, the voids can either grow and coalesce or collapse and close up. There is a large literature on porosity evolution in rate independent or nearly rate independent solids aimed at modeling room temperature ductile fracture processes, see [93] and [94] for reviews. Analyses of void growth and collapse in linear and nonlinear viscous solids have been aimed at modeling creep fracture and/or compaction of porous solids, see for example [81, 95, 96, 97, 84, 98]. Typically, void coalescence occurs at high values of the stress triaxiality (the ratio of the first to second stress invariants) and void collapse occurs at negative values of the stress triaxiality. More recently the role of the third stress invariant (as can be measured by the Lode parameter) in affecting porosity evolution at moderate and low values of stress triaxiality has been receiving much attention, e.g. [63, 67, 99, 74, 64, 65, 80, 66].

At low but positive values of the stress triaxiality, isolated [81] or well separated voids [100, 101] (as also shown in Chapter 3) may collapse for certain Lode parameter values. On the other hand, Pardoen and Hutchinson [61] showed that a reduction in initial void spacing promotes void coalescence and hence closely spaced voids could coalesce even at low values

of the stress triaxiality. Thus, there is the possibility, depending on void spacing and stress state, that either void collapse or void coalescence may occur.

Here, the possible transition between void collapse for well separated voids to coalescence for sufficiently close voids in a nonlinearly viscous single crystal subject to creep loading has been investigated . The value of the stress triaxiality is fixed at 1/3 and three values of the Lode parameter (a measure of the third stress invariant that has values between $-1$ and 1) $-1, 0$ and 1 are considered. Three dimensional unit cell calculations are carried out for three values of creep exponent, two initial void volume fractions and, for each initial void volume fraction, a range of void spacings. The results show that, depending on the values of these parameters void coalescence, void collapse or neither can occur.

## 4.2. Problem Formulation

The problem formulation and numerical method follow that in Chapter 3 where further details and additional references are given.

### 4.2.1. Cell Model

Three dimensional finite element calculations are carried out to model the response of a regular array of initially spherical voids of radius $r_0$ as shown in Fig. 4.1. Cartesian tensor notation is used and the origin of the coordinate system is taken to be at the center of the void. An initially rectangular cuboidal unit cell with side lengths $2a_i^0$ in the $x_i$ direction $(i = 1, 2, 3)$ is analyzed. The initial inter-void spacing is $2l_i^0 = 2a_i^0 - 2r_0$.

The main loading direction is parallel to the $x_1$ axis and the edges initially parallel to the $x_2$ and $x_3$ axes are required to remain parallel to their respective axes during deformation which is consistent with, but stronger than, symmetry about these axes.

The boundary conditions on the faces of the unit cell are

$$
\begin{aligned}
u_1(a_1^0, x_2, x_3) &= U_1(t)\ ,\ T_2(a_1^0, x_2, x_3) = 0\ ,\ T_3(a_1^0, x_2, x_3) = 0 \\
u_2(x_1, a_2^0, x_3) &= U_2(t)\ ,\ T_1(x_1, a_2^0, x_3) = 0\ ,\ T_3(x_1, a_2^0, x_3) = 0 \\
u_3(x_1, x_2, a_3^0) &= U_3(t)\ ,\ T_1(x_1, x_2, a_3^0) = 0\ ,\ T_2(x_1, x_2, a_3^0) = 0
\end{aligned}
\tag{31}
$$

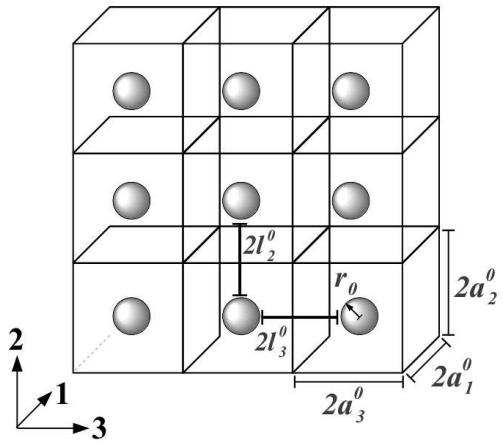


FIGURE 4.1. Schematic representation of the periodic arrangement of voids in the $x_2$ and $x_3$ directions with the geometric parameters. Not shown in the figure is the periodic distribution of voids in the $x_1$ direction where the initial inter-void ligament size is $2l_1^0$.

Symmetry about each axis is imposed so that only 1/8 of the cell needs to be analyzed numerically so that

$$\begin{aligned} u_1(0,x_2,x_3) &= 0\ ,\ T_2(0,x_2,x_3)=0\ ,\ T_3(0,x_2,x_3)=0 \\ u_2(x_1,0,x_3) &= 0\ ,\ T_1(x_1,0,x_3)=0\ ,\ T_3(x_1,0,x_3)=0 \\ u_3(x_1,x_2,0) &= 0\ ,\ T_1(x_1,x_2,0)=0\ ,\ T_2(x_1,x_2,0)=0 \end{aligned} \tag{32}$$

The time histories of the displacements $U_1(t)$, $U_2(t)$ and $U_3(t)$ in Eq. (31) are determined by the analysis. The value of the nominal (or engineering) stress, $N_1$, defined by

$$N_1 = \frac{a_2 a_3}{a_2^0 a_3^0}\Sigma_1\ ,\ \Sigma_1 = \frac{1}{a_2 a_3}\int_0^{a_2}\int_0^{a_3}\sigma_{11}(a_1,x_2,x_3)dx_2dx_3 \tag{33}$$

is required to remain fixed throughout the deformation history together with

$$\Sigma_2 = \rho_2\Sigma_1 \qquad \Sigma_3 = \rho_3\Sigma_1 \tag{34}$$

where $\rho_2$ and $\rho_3$ are constants, $a_i = a_1^0 + U_i$ and $\Sigma_2$ and $\Sigma_3$ are overall true stresses defined by expressions analogous to that for $\Sigma_1$. Also $2l_i = 2a_i - 2r_i$ is defined as the current inter-void

ligament size with $r_i$ the intersection of the void surface with the $x_i$ coordinate axis.

The overall effective stress, $\Sigma_e$, and the overall hydrostatic stress (positive in tension), $\Sigma_h$, are given by

$$\Sigma_e = \frac{1}{\sqrt{2}}\sqrt{(\Sigma_1-\Sigma_2)^2+(\Sigma_2-\Sigma_3)^2+(\Sigma_3-\Sigma_1)^2} \qquad \Sigma_h = \frac{1}{3}(\Sigma_1+\Sigma_2+\Sigma_3) \tag{35}$$

The stress triaxiality $\chi$, and Lode parameter, $L$, values are given by

$$\chi = \frac{\Sigma_h}{\Sigma_e} = \frac{\sqrt{2}}{3}\frac{1+\rho_2+\rho_3}{\sqrt{(1-\rho_2)^2+(\rho_2-\rho_3)^2+(\rho_3-1)^2}} \tag{36}$$

and

$$L = \frac{2\Sigma_2-\Sigma_1-\Sigma_3}{\Sigma_1-\Sigma_3} = \frac{2\rho_2-1-\rho_3}{1-\rho_3} \tag{37}$$

While calculating Lode parameter value in Eq. (37) the stress state is taken to be such that $\Sigma_1 \geq \Sigma_2 \geq \Sigma_3$.

The overall effective creep strain is defined as

$$E_e = \frac{\sqrt{2}}{3}\sqrt{(\tilde{E}_1-\tilde{E}_2)^2+(\tilde{E}_2-\tilde{E}_3)^2+(\tilde{E}_3-\tilde{E}_1)^2} \tag{38}$$

where

$$\tilde{E}_1 = \ln\left(\frac{a_1}{\tilde{a}_1}\right) \qquad \tilde{E}_2 = \ln\left(\frac{a_2}{\tilde{a}_2}\right) \qquad \tilde{E}_3 = \ln\left(\frac{a_3}{\tilde{a}_3}\right) \tag{39}$$

where $\tilde{a}_i$ is the value of $a_i$ after the first elastic step.

In Chapter 3 tensile creep calculations were carried out for fixed tensile nominal stress and for fixed tensile true stress, with in both cases the same values of stress triaxiality and Lode parameter. It was found that when quantities such as the evolution of void volume fraction $f$ were plotted against the overall effective strain $E_e$, the results were virtually the same for both types of fixed tensile stress loading.

4.2.2. Constitutive Relation

As in Chapter 3, the crystal plasticity constitutive implementation is based on the UMAT due to Huang [88] as modified by Kysar [89] which follows the constitutive formulation in Asaro and Needleman [90].

The deformation gradient, $\mathbf{F}$, is written as

$$\mathbf{F} = \mathbf{F}^* \cdot \mathbf{F}^P \tag{40}$$

where $\mathbf{F}^*$ is due to stretching and rotation of the crystal lattice and $\mathbf{F}^P$ is due to crystallographic slip. Differentiating Eq. (40) with respect to time and combining terms gives

$$\dot{\mathbf{F}} \cdot \mathbf{F}^{-1} = \mathbf{D} + \mathbf{\Omega} = (\mathbf{D}^* + \mathbf{\Omega}^*) + (\mathbf{D}^p + \mathbf{\Omega}^p) \tag{41}$$

Here, $(\mathbf{D}^* + \mathbf{\Omega}^*)$ are, respectively, the elastic rate of stretching and spin tensors, and the plastic rate of stretching, $\mathbf{D}^p$, and spin tensors, $\mathbf{\Omega}^p$, are given by

$$\mathbf{D}^p = \sum_\alpha \dot{\gamma}^{(\alpha)} \mathbf{P}^{(\alpha)} \qquad \mathbf{\Omega}^p = \sum_\alpha \dot{\gamma}^{(\alpha)} \mathbf{W}^{(\alpha)} \tag{42}$$

where $\dot{\gamma}^{(\alpha)}$ is the rate of shearing on slip system $\alpha$, and

$$\mathbf{P}^{(\alpha)} = \frac{1}{2}(\mathbf{s}^{(\alpha)*}\mathbf{m}^{(\alpha)*} + \mathbf{m}^{(\alpha)*}\mathbf{s}^{(\alpha)*}) \qquad \mathbf{W}^{(\alpha)} = \frac{1}{2}(\mathbf{s}^{(\alpha)*}\mathbf{m}^{(\alpha)*} - \mathbf{m}^{(\alpha)*}\mathbf{s}^{(\alpha)*}) \tag{43}$$

with

$$\mathbf{s}^{(\alpha)*} = \mathbf{F}^* \cdot \mathbf{s}^{(\alpha)} \qquad \mathbf{m}^{(\alpha)*} = \mathbf{m}^{(\alpha)} \cdot \mathbf{F}^{*-1} \tag{44}$$

where $\mathbf{s}^{(\alpha)}$ and $\mathbf{m}^{(\alpha)}$ are the slip directions and the slip plane normals of the crystal in the reference, undeformed lattice.

The stress rate on axes rotating with the material, $\hat{\boldsymbol{\sigma}}$, is given by

$$\hat{\boldsymbol{\sigma}} = (\mathbf{L} - \boldsymbol{\sigma}\mathbf{I}) : \mathbf{D} - \sum_\alpha \dot{\gamma}^{(\alpha)} \mathbf{R}^{(\alpha)} \tag{45}$$

with

$$\mathbf{R}^{(\alpha)} = \mathbf{L} : \mathbf{P}^{(\alpha)} + \mathbf{W}^{(\alpha)} \cdot \boldsymbol{\sigma} - \boldsymbol{\sigma} \cdot \mathbf{W}^{(\alpha)} \tag{46}$$

Here, $\mathbf{L}$ is the tensor of elastic moduli (small elastic strains are assumed). The elastic constants are taken to be those of a PWA1484 Ni-based single crystal superalloy and are specified by $C_{11} = 283.3$GPa, $C_{12} = 197.5$GPa and $C_{44} = 112$GPa as in Chapter 3.

An fcc-based crystal structure is modeled with the potentially active slip system taken to be the twelve primary octahedral slip systems $\{111\} < 110 >$. Slip is assumed to obey Schmid's law so that the slip rate $\dot{\gamma}^{(\alpha)}$ only depends on the current stress state through the slip-system resolved shear stress $\tau^{(\alpha)}$. A power law viscous relation for the slip rates $\dot{\gamma}^{(\alpha)}$ is used. The initial value of slip on each slip system is taken to be zero and the evolution of slip on slip system $\alpha$ is given by

$$\dot{\gamma}^{(\alpha)} = \left\{ \dot{\gamma}_0 \left| \frac{\tau^{(\alpha)}}{\tau_0} \right|^n \right\} \mathrm{sgn}(\tau) \tag{47}$$

where the slip-system resolved shear stress is

$$\tau^{(\alpha)} = \mathbf{m}^{(\alpha)*} \cdot \boldsymbol{\sigma} \cdot \mathbf{s}^{(\alpha)*} = \boldsymbol{\sigma} : \mathbf{P}^{(\alpha)} \tag{48}$$

with $\tau_0$, $\dot{\gamma}_0$ and $n$ material constants. The material parameters used in Eq. (47) are $\tau_0 = 245$MPa and $\dot{\gamma}_0 = 1.53 \times 10^{-9}\mathrm{s}^{-1}$. Three values of the power law creep exponent, $n = 3$, 5 and 7 are used in the calculations.

### 4.2.3. Numerical Method

The calculations are carried out using the commercial finite element code ABAQUS [54], and using a UMAT by Huang [88] and Kysar [89] modified for the creep relation given in Section 4.2.2. The values of $\Sigma_i$ vary with time so that the fixed stress ratio in Eq. (34) needs to be maintained by controlling the tractions acting on the surfaces of the unit cell. At each time step the proportionality of the overall stresses is monitored using the URDFIL user subroutine in ABAQUS [54]. Any deviation from the prescribed values of the proportionality constants $\rho_2$ and $\rho_3$ given in Eq. (34) is counteracted by applying an additional uniform traction on the corresponding surfaces using the DLOAD user subroutine. The variations in $\rho_2$ and $\rho_3$ were kept within 0.1% over the course of the loading history. The time steps were

varied during the course of the deformation history so that $\Delta\gamma^{(\alpha)}$ on any slip system never exceeded 0.001.

*Loading:*

The calculations here are carried out for a constant stress triaxiality value $\chi = 1/3$ and for three values of the Lode parameter $L = -1, 0$ and 1. The Lode parameter values $L = -1$ ($\Sigma_1 > \Sigma_2 = \Sigma_3$) and $L = 1$ ($\Sigma_1 = \Sigma_2 > \Sigma_3$) correspond to an overall axisymmetric state of stress while $L = 0$ ($\Sigma_1 > \Sigma_2 > \Sigma_3$ with $(\Sigma_1 + \Sigma_3)/2 = \Sigma_2$) corresponds to an overall state of shear plus hydrostatic stress. The $< 001 >$ orientations of the fcc crystal are taken to coincide with the coordinate axes.

The expressions Eq. (36) and Eq. (37) together with $\Sigma_e = 750$MPa in Eq. (35) constitute a set of quadratic equations for the stress components. Imposing the inequality $\Sigma_1 \geq \Sigma_2 \geq \Sigma_3$ as in Chapter 3, gives a unique state of stress for a given stress triaxiality and Lode parameter value. The initial values of $\Sigma_i$ for $\chi = 1/3$ and for $L = -1, 0$ and 1 are given in Table 4.1. For each initial stress state, the creep response with fixed $N_1$ is analyzed. In the first time step the response is taken to be elastic.

TABLE 4.1. Values of the stress triaxiality $\chi$, the Lode parameter $L$, and the initial overall stresses $\Sigma_i$.

| $\chi$ | $L$ | $\Sigma_1$ (MPa) | $\Sigma_2$ (MPa) | $\Sigma_3$ (MPa) |
|---|---|---|---|---|
| 1/3 | -1.00 | 750.00 | 0.00 | 0.00 |
| 1/3 | 0.00 | 683.01 | 250.00 | -183.01 |
| 1/3 | 1.00 | 500.00 | 500.00 | -250.00 |

*Unit cell geometry and finite element mesh:*

Two initial void volume fractions $f_0 = 0.01$ and $f_0 = 0.1$ are considered where $f_0 = (4\pi {r_0}^3/3)/8a_1^0 a_2^0 a_3^0$. Symmetry about each axis is assumed so that only 1/8 of the cuboidal cell shown in Fig. 4.1 is modeled. For both initial void volume fractions the cell dimensions are varied to achieve various initial inter-void spacings. The geometric parameters defining the various unit cells analyzed are tabulated in Table 4.2. The initial cell dimensions

are taken to be such that $a_1^0/r_0 = a_2^0/r_0$ in all cases.

TABLE 4.2. The ratios of initial cell dimensions to void radius, $a_i^0/r_0$, and the ratios of initial ligaments to void radius, $l_i^0/r_0$, where $i = 1, 2, 3$.

| $f_0 = 0.01$ | | | | | |
|---|---|---|---|---|---|
| $a_1^0/r_0$ | $a_2^0/r_0$ | $a_3^0/r_0$ | $l_1^0/r_0$ | $l_2^0/r_0$ | $l_3^0/r_0$ |
| 6.06 | 6.06 | 1.43 | 5.06 | 5.06 | 0.43 |
| 5.80 | 5.80 | 1.56 | 4.80 | 4.80 | 0.56 |
| 5.55 | 5.55 | 1.70 | 4.55 | 4.55 | 0.70 |
| 5.34 | 5.34 | 1.84 | 4.34 | 4.34 | 0.84 |
| 5.21 | 5.21 | 1.94 | 4.21 | 4.21 | 0.94 |
| 5.12 | 5.12 | 2.00 | 4.12 | 4.12 | 1.00 |
| 4.97 | 4.97 | 2.12 | 3.97 | 3.97 | 1.12 |
| 4.50 | 4.50 | 2.59 | 3.50 | 3.50 | 1.59 |
| 3.75 | 3.75 | 3.75 | 2.75 | 2.75 | 2.75 |
| $f_0 = 0.1$ | | | | | |
| $a_1^0/r_0$ | $a_2^0/r_0$ | $a_3^0/r_0$ | $l_1^0/r_0$ | $l_2^0/r_0$ | $l_3^0/r_0$ |
| 1.91 | 1.91 | 1.43 | 0.91 | 0.91 | 0.43 |
| 1.85 | 1.85 | 1.52 | 0.85 | 0.85 | 0.52 |
| 1.79 | 1.79 | 1.62 | 0.79 | 0.79 | 0.62 |
| 1.74 | 1.74 | 1.74 | 0.74 | 0.74 | 0.74 |
| 1.67 | 1.67 | 1.87 | 0.67 | 0.67 | 0.87 |
| 1.62 | 1.62 | 2.00 | 0.62 | 0.62 | 1.00 |
| 1.52 | 1.52 | 2.27 | 0.52 | 0.52 | 1.27 |
| 1.38 | 1.38 | 2.74 | 0.38 | 0.38 | 1.74 |

The calculations use 20-node hybrid solid elements with quadratic displacement interpolation and linear pressure interpolation, C3D20H elements [54]. Finite element meshes for two unit cells with $f_0 = 0.01$ are shown in Fig. 4.2(a) and for two unit cells with $f_0 = 0.1$

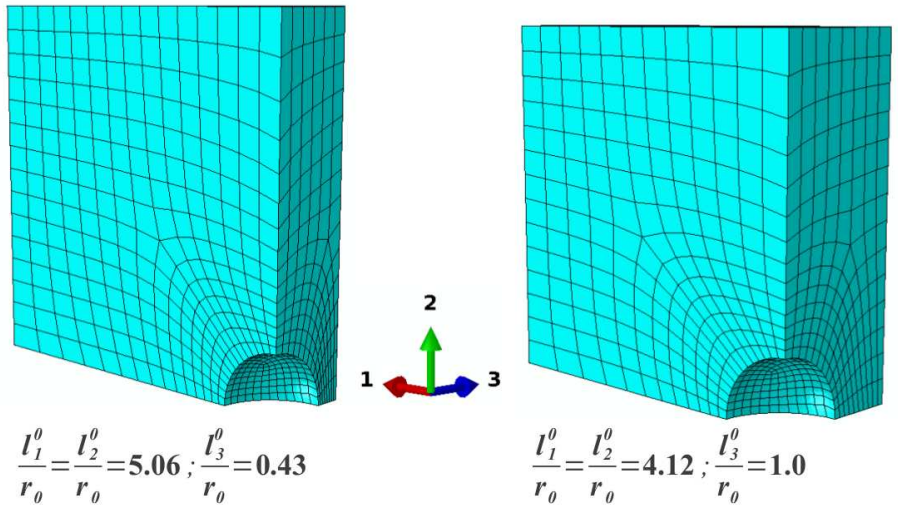


(a)

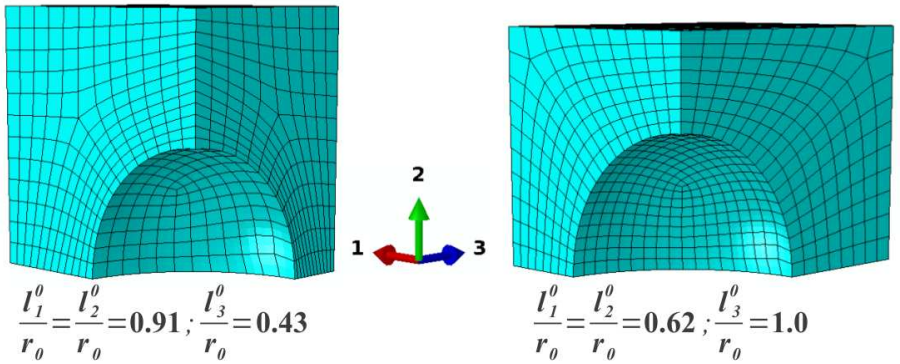


(b)

FIGURE 4.2. Finite element mesh showing 1/8 of the unit cell with an initial spherical void of radius $r_0$ in the center giving an initial void volume fraction of (a) $f_0 = 0.01$ and (b) $f_0 = 0.1$.

in Fig. 4.2(b). The number of elements in the finite element meshes varied from a minimum of 916 elements to a maximum of 2140 elements. In general a larger number of elements were used for smaller inter-void ligament sizes to account for possible localized deformations.

Mesh convergence studies were performed for several unit cells. The evolution of the relative void volume fraction $f/f_0$ with the overall effective creep strain $E_e$ was used to assess convergence. For example for $\chi = 1/3$ and $L = 1$ the unit cell with $f_0 = 0.01$ and $l_3^0/r_0 = 0.94$ with 994 elements at $E_e = 0.5$ reached $f/f_0 = 1.013$ and at $E_e = 1.0$ reached

$f/f_0 = 0.81$ whereas with 1680 elements at $E_e = 0.5$ reached $f/f_0 = 1.016$ and at $E_e = 1.0$ reached $f/f_0 = 0.83$. Leading to an error of 0.3% at $E_e = 0.5$ and 2.5% at $E_e = 1.0$.

## 4.3. Numerical Results

The calculations were carried out for the unit cell geometries in Table 4.2 with the values of stress triaxiality and Lode parameter given in Table 4.1 and for $n = 3, 5$ and 7 in Eq. (47). In total 153 cases were analyzed. The calculations were continued until one of the following conditions was met: (i) void coalescence; a minimum relative inter-void ligament $l_i^r = l_i/l_i^0 < 0.2$; (ii) void collapse; a relative void volume fraction $f/f_0 \approx 0$ or $f/f_0$ decreasing monotonically (and sufficiently rapidly) between $E_e \approx 0.5$ and $E_e = 1$; (iii) neither void coalescence or void collapse up to an overall effective creep strain $E_e = 1.0$.

### 4.3.1. Evolution of the Void Volume Fraction

The void volume fraction is $f = (V_{cell} - V_M)/V_{cell}$ where $V_{cell}$ is the current cell volume and $V_M$ is the current material volume (sum of current elemental volumes). The quantity $f/f_0$ is the relative void volume fraction.

The evolution of $f/f_0$ with $E_e$ for the calculations with $f_0 = 0.01$ is shown in Fig. 4.3. The unit cells are characterized by the initial $x_3$ inter-void ligament to void radius ratio, $l_3^0/r_0$. With $L = -1$, Fig. 4.3(a), $f/f_0$ monotonically increases with decreasing slope for sufficiently closely spaced voids while for more widely spaced voids $f/f_0$ initially increases, then decreases slightly but remains greater than unity until the limiting value $E_e = 1$ is reached. As expected for $L = -1$, the value of $f/f_0$ at any given strain level increases with increasing value of creep exponent $n$ [81, 97, 84]. The effect of the value of the creep exponent $n$ on void growth is greater for more closely spaced voids (smaller values of $l_3^0/r_0$).

As shown in Fig. 4.3(b), for $L = 0$, there is a clear transition with initial void spacing between the tendency for void growth and void collapse. As shown for $l_3^0/r_0 = 0.94$ after an initial increase $f/f_0$ saturates to $f/f_0 \approx 1.1$. For a smaller value of $l_3^0/r_0$, $f/f_0$ increases monotonically whereas for a greater value of $l_3^0/r_0$, $f/f_0$ decreases monotonically. For $L = 0$ there is a relatively small effect of the value of creep exponent $n$ on the evolution of $f/f_0$.

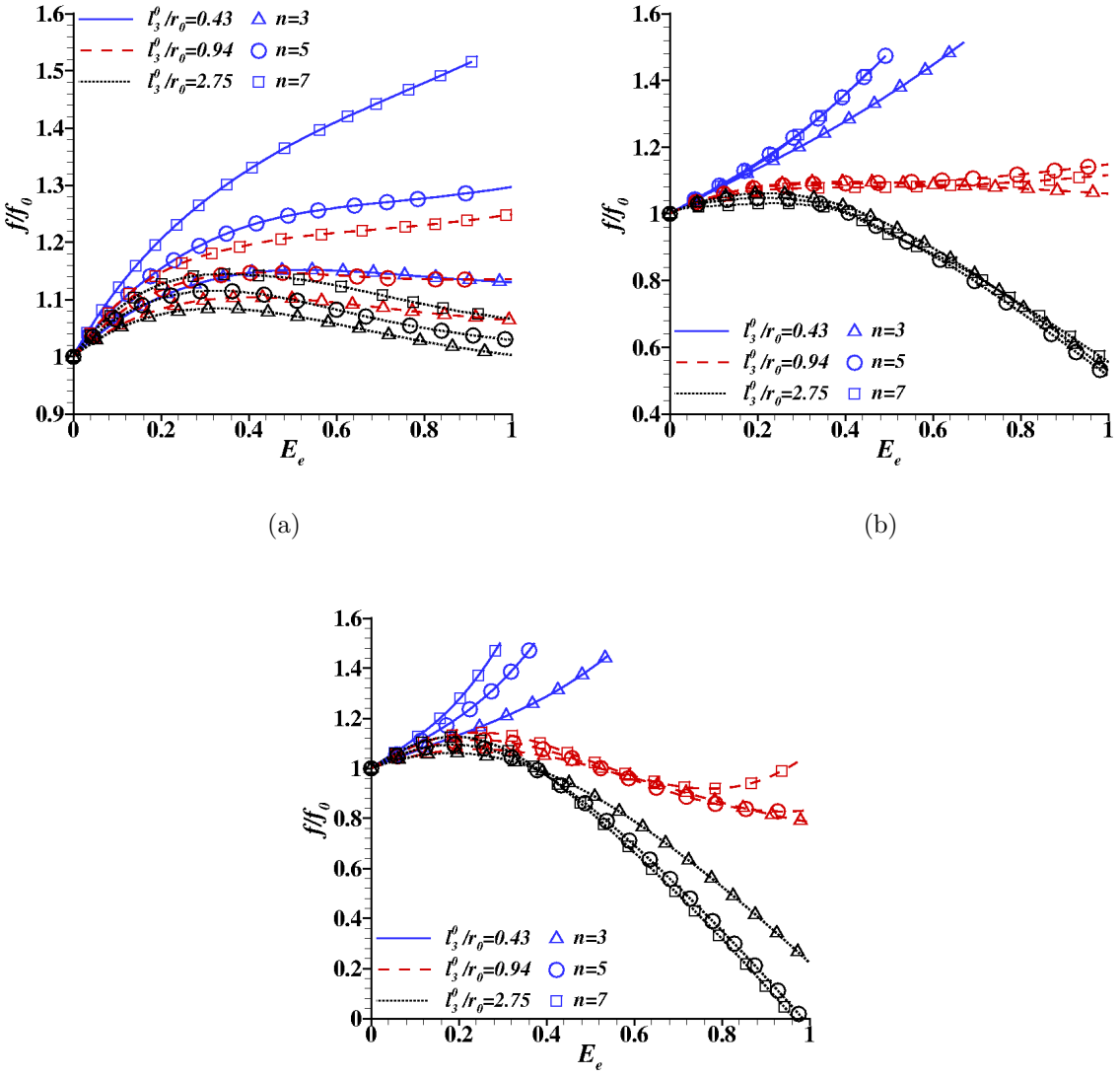


FIGURE 4.3. Evolution of the relative void volume fraction $f/f_0$ as a function of overall effective creep strain $E_e$ for three Lode parameter values (a) $L = -1$, (b) $L = 0$ and (c) $L = 1$. The initial void volume fraction $f_0 = 0.01$ and stress triaxiality $\chi = 1/3$.

Similar to $L = 0$, for $L = 1$, Fig. 4.3(c), the evolution of $f/f_0$ with $E_e$ shows a transition from void growth to void collapse (monotonically decreasing $f/f_0$) with increasing values of $l_3^0/r_0$. In contrast to the calculations with $L = 0$, for $L = 1$ there is a significant

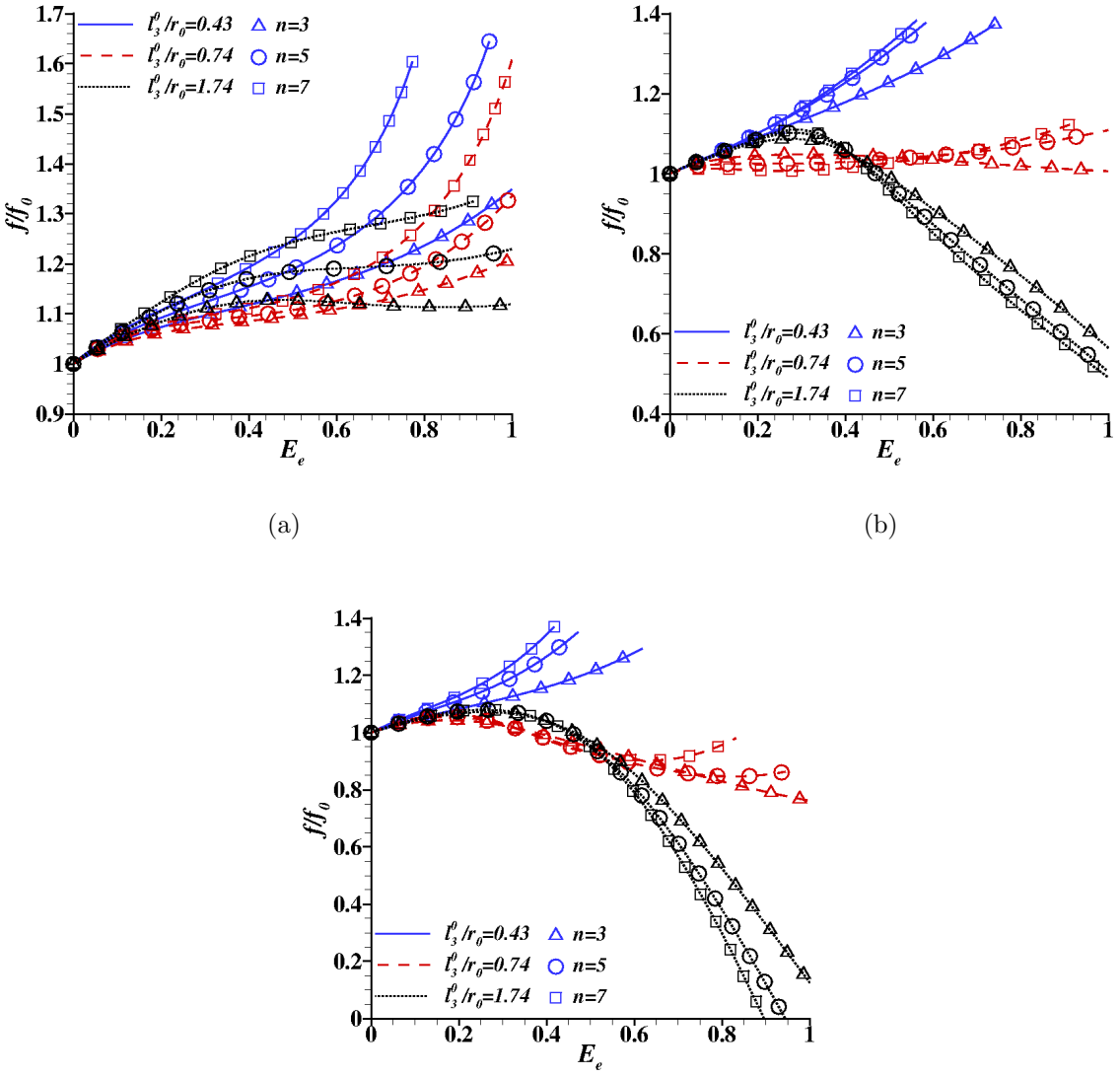


FIGURE 4.4. Evolution of the relative void volume fraction $f/f_0$ as a function of overall effective creep strain $E_e$ for three Lode parameter values (a) $L = -1$, (b) $L = 0$ and (c) $L = 1$. The initial void volume fraction $f_0 = 0.1$ and stress triaxiality $\chi = 1/3$.

effect of $n$ on the evolution of $f/f_0$ with $E_e$. For smaller $l_3^0/r_0$ values, the value of $f/f_0$ at a given strain level increases with increasing $n$ which is similar to $L = -1$. For intermediate values of $l_3^0/r_0$, depending on the value of $n$ a transition from void growth to void collapse is

seen. For larger values of $l_3^0/r_0$, where void collapse is observed for all three values of $n$, the value of $f/f_0$ decreases with increasing value of $n$. A similar but stronger effect of the value of $n$ on void collapse in isotropic viscous solids under far field compressive stresses (negative stress triaxiality) has been previously seen by [95, 97].

The evolution of $f/f_0$ with $E_e$ for the calculations with $f_0 = 0.1$ is shown in Fig. 4.4. The major difference between the results for $f_0 = 0.1$ and the results for $f_0 = 0.01$ is that with $L = -1$ and $f_0 = 0.1$, $f/f_0$ monotonically increases with increasing slope for relatively closely spaced voids, Fig. 4.4(a), showing a clear tendency toward coalescence. For $L = 0$ and $L = 1$, Figs. 4.4(b) and 4.4(c), the response is qualitatively similar to that for the cases with $f_0 = 0.01$. What is meant by $f/f_0$ decreasing sufficiently rapidly is illustrated in Fig. 4.4(b) where $L = 0$. With $n = 3$ and $l_3^0/r_0 = 0.74$, the red dashed curve with triangles, $f/f_0$ is decreasing monotonically for $0.5 \leq E_e \leq 1.0$ but not sufficiently rapidly. On the other hand, with $n = 3$ and $l_3^0/r_0 = 1.74$, the black dotted curve with triangles, $f/f_0$ is decreasing sufficiently rapidly to be regarded as tending to void collapse.

Figure 4.5 compares the evolution of $f/f_0$ with $E_e$ for $f_0 = 0.01$ and 0.1 for two $l_3^0/r_0$ values. The comparison is shown for a creep exponent $n = 5$, the behavior is qualitatively the same for creep exponents $n = 3$ and 7. For $L = -1$, the value of $f/f_0$ for $f_0 = 0.01$ is greater than the value of $f/f_0$ for $f_0 = 0.1$ until $E_e \approx 0.65$ for $l_3^0/r_0 = 0.43$, Fig. 4.5(a), and until $E_e \approx 0.75$ for $l_3^0/r_0 = 1.0$, Fig. 4.5(b). The rapid increase in the value of $f/f_0$ for smaller values of $f_0$ as compared to the greater values of $f_0$ for $\chi = 1/3$ and $L = -1$ has also been observed by Sangyul and Kim [78] in their analyses for increasing tensile loading. Regardless of the value of $l_3^0/r_0$ for $L = 0$ and $L = 1$, the value of $f/f_0$ for the unit cell with $f_0 = 0.01$ is always greater than the value for $f/f_0$ for the corresponding unit cell with $f_0 = 0.1$. As shown in Fig. 4.5(a) for $l_3^0/r_0 = 0.43$, the value of $f/f_0$ for $L = 1$ at a given overall strain is greater than the corresponding value of $f/f_0$ for $L = -1$ for both $f_0 = 0.01$ and 0.1. On the other hand, for greater values of $l_3^0/r_0$, Fig. 4.5(b), the value of $f/f_0$ at a given strain for $L = 1$ is always less than the corresponding value for $f/f_0$ for $L = -1$.

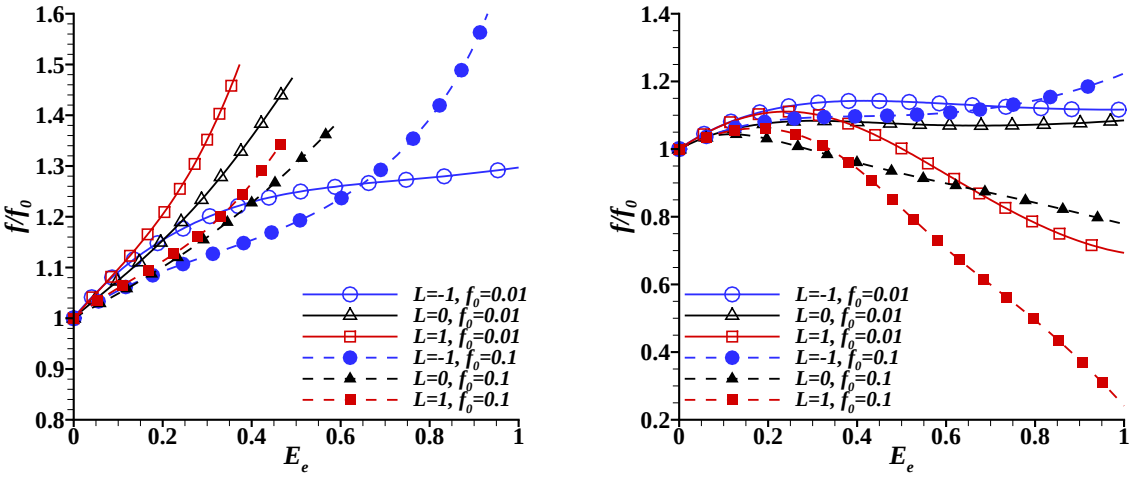


(a) (b)

FIGURE 4.5. Evolution of the relative void volume fraction $f/f_0$ as a function of overall effective creep strain $E_e$ for two initial inter-void ligament to initial void radius ratio (a) $l_3^0/r_0 = 0.43$ and (b) $l_3^0/r_0 = 1.0$. The creep exponent $n = 5$ and stress triaxiality $\chi = 1/3$.

### 4.3.2. Evolution of the Inter-Void Ligament

For the calculations with $f_0 = 0.01$ the evolution of the relative ligament size in the $x_3$ direction i.e. $l_3^r = l_3/l_3^0 = (a_3 - r_3)/(a_3^0 - r_0)$ is used to exhibit inter-void interaction as it is the direction of minimum applied stress (see Table 4.1) as well as is the direction of minimum initial inter-void spacing (see Table 4.2). Hence, the greatest reduction in ligament size generally occurs in the $x_3$ direction. The evolution of $l_3^r$ with $E_e$ for three void spacings with $f_0 = 0.01$ is shown in Fig. 4.6. For $L = -1$, Fig. 4.6(a), there is a gradual decrease in $l_3^r$ for all the values of $l_3^0/r_0$ until the limiting condition $l_3^r = 0.2$ or $E_e = 1$ is reached. For $L = 0$, Fig. 4.6(b), and $L = 1$, Fig. 4.6(c), a rapid decrease in $l_3^r$ occurs for smaller values of $l_3^0/r_0$. The effect of creep exponent $n$ on the evolution of $l_3^r$ with $E_e$ reduces with increasing $l_3^0/r_0$ and basically no effect of $n$ on the evolution of $l_3^r$ with $E_e$ is seen for $l_3^0/r_0 = 2.75$ for all three Lode parameter values.

The evolution of $l_3^r$ with $f_0 = 0.1$ is qualitatively similar to that for $f_0 = 0.01$. But for

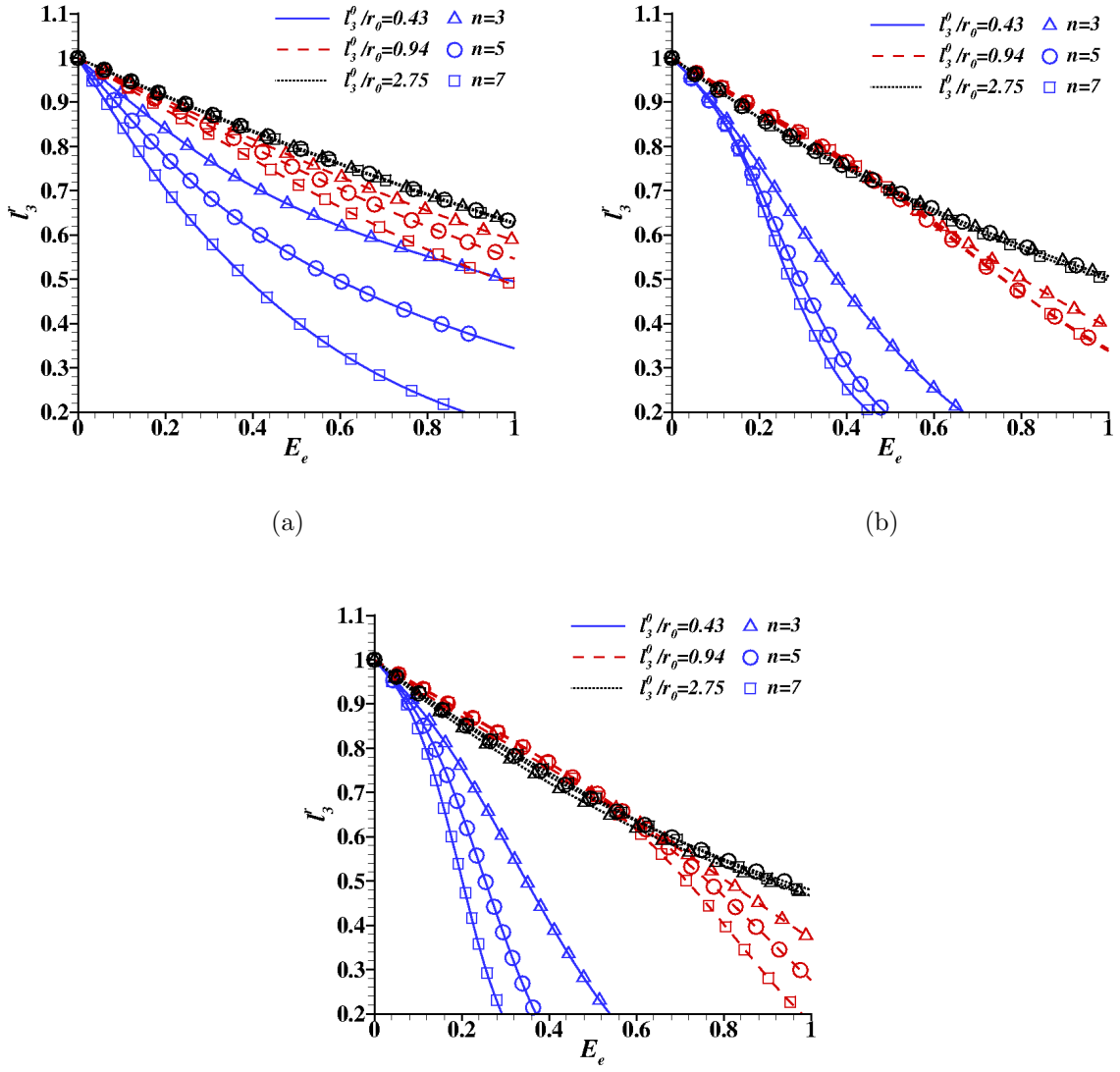


(a)

(b)

(c)

FIGURE 4.6. Evolution of the relative inter-void ligament $l_3^r = l_3/l_3^0$ as a function of overall effective creep strain $E_e$ for three Lode parameter values (a) $L = -1$, (b) $L = 0$ and (c) $L = 1$. The initial void volume fraction $f_0 = 0.01$ and stress triaxiality $\chi = 1/3$.

the calculations with $f_0 = 0.1$, $x_3$ is not always the direction of minimum initial inter-void spacing (see Table 4.2). Hence for $L = -1$ where $\Sigma_1 > \Sigma_2 = \Sigma_3$ the tendency to coalescence can occur along either the $x_2$ or $x_3$ direction. For the unit cells with $f_0 = 0.1$ the evolution

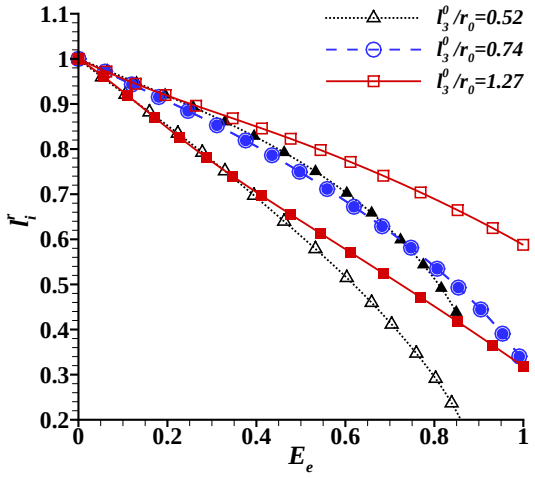


FIGURE 4.7. Evolution of the relative inter-void ligament $l_3^r = l_3/l_3^0$ (open symbols) and $l_2^r = l_2/l_2^0$ (closed symbols) as a function of overall effective creep strain $E_e$ for a Lode parameter value $L = -1$. The initial void volume fraction $f_0 = 0.1$, creep exponent $n = 7$ and stress triaxiality $\chi = 1/3$.

of $l_3^r$ and of $l_2^r = l_2/l_2^0$ for $L = -1$ and $n = 7$ are shown in Fig. 4.7. The evolution of $l_3^r$ for the unit cell with $l_3^0/r_0 = 0.52$ and the evolution of $l_2^r$ for the unit cell with $l_3^0/r_0 = 1.27$ (where $l_2^0/r_0 = 0.52$) are the same until $E_e \approx 0.4$. For $E_e >\approx 0.4$, $l_3^r$ for $l_3^0/r_0 = 0.52$ decreases more rapidly than $l_2^r$ for $l_3^0/r_0 = 1.27$ leading to earlier void coalescence. This may be due to the fact that the initial area fraction of the void ($\pi {r_0}^2/4a_2^0a_3^0$) on the $x_2 - x_3$ plane for the unit cell with $l_3^0/r_0 = 0.52$ is $\approx 0.060$ which is larger than that for the unit cell with $l_3^0/r_0 = 1.27$ ($\approx 0.049$). For $l_3^0/r_0 = 0.74$ where $l_1^0/r_0 = l_2^0/r_0 = l_3^0/r_0 = 0.74$, the evolution of both $l_3^r$ and $l_2^r$ with $E_e$ is the same.

The relative inter void ligament $l_3^r = l_3/l_3^0$ depends on the current cell dimension $a_3$ and on the current void radius $r_3$. For nearly rate independent materials at stress triaxiality values greater than $\approx 1$ the onset of void coalescence is associated with flow localization in the ligament between adjacent voids leading to an overall uniaxial straining mode, [58], which in the calculations here would correspond to $da_3/dE_e \approx 0$. In Fig. 4.8(a) for $f_0 = 0.01$ and in Fig. 4.8(b) for $f_0 = 0.1$, even when the voids are extremely close to each other for $l_3^0/r_0 = 0.43$, $a_3/a_3^0$ decreases monotonically for both $L = -1$ and $L = 1$ without a transition

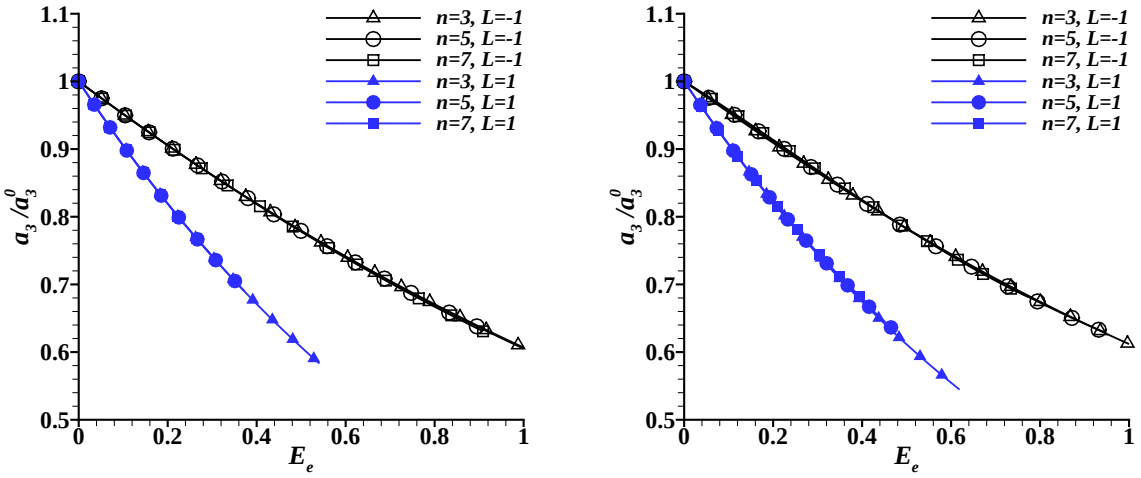


(a)




(b)

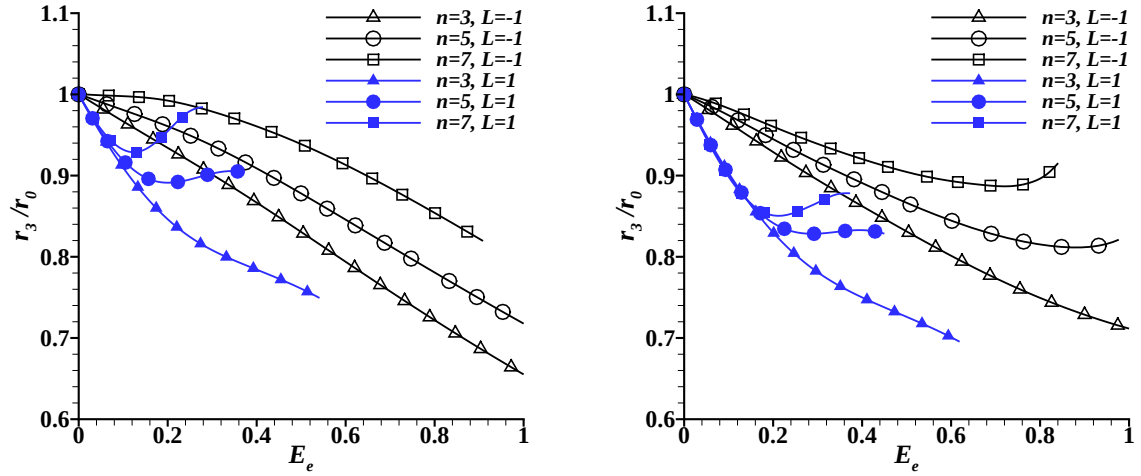


(c)




(d)

FIGURE 4.8. Evolution of the normalized unit cell dimension (a) $a_3/a_3^0$ for a unit cell with $f/f_0 = 0.01$ and (b) $a_3/a_3^0$ for a unit cell with $f/f_0 = 0.1$; and evolution of normalized void radius (c) $r_3/r_0$ for a unit cell with $f/f_0 = 0.01$ and (d) $r_3/r_0$ for a unit cell with $f/f_0 = 0.1$ as a function of $E_e$ for $l_3^0/r_0 = 0.43$. The stress triaxiality $\chi = 1/3$.

to an overall uniaxial straining mode for all three creep exponent values. For $f_0 = 0.01$ and $L = -1$, Fig. 4.8(c), $r_3/r_0$ gradually decreases until $E_e = 1$. On the other hand, for

$f_0 = 0.1$ and $L = -1$, Fig. 4.8(d), $r_3/r_0$ gradually decreases until a creep exponent dependent strain value and then increases. The value of $r_3/r_0$ at any given strain level decreases with a decreasing value of $n$ for $L = -1$. For $L = 1$, regardless of the value of $n$, $r_3/r_0$ initially decreases until a critical value of $E_e$ is reached and then $r_3/r_0$ increases rapidly for $n = 7$. The value of $r_3/r_0$ remains nearly constant for $n = 5$ while for $n = 3$ the slope of the $r_3/r_0$ versus $E_e$ curve decreases. This is true for both the unit cells with $f_0 = 0.01$, Fig. 4.8(c), and $f_0 = 0.1$, Fig. 4.8(d). The change in the evolution of $r_3/r_0$ beyond a critical $E_e$ leads to the transition from a gradual reduction in the inter-void ligament to a rapid decrease leading to accelerated void coalescence.

Figure 4.9 shows the critical strain to coalescence, $E_e^c$ (the value of $E_e$ at which $l_3^r = 0.2$) for the cases where void coalescence occurred. In general the value of $E_e^c$ increases linearly as a function of $l_3^0/r_0$. As expected the value of $E_e^c$ decreases with increasing values of $n$ so that with increasing value of $n$ the void coalescence condition is met for unit cells with greater values of $l_3^0/r_0$. For $L = 1$, the value of $E_e^c$ for $f_0 = 0.1$ is slightly greater than the value of $E_e^c$ for $f_0 = 0.01$. Whereas for $L = -1$, the value of $E_e^c$ for $f_0 = 0.1$ is slightly smaller than the value of $E_e^c$ for $f_0 = 0.01$ as shown in Fig. 4.9(c) for $n = 7$ and $l_3^0/r_0 = 0.43$. For $L = 0$, the value of $E_e^c$ for $f_0 = 0.1$ is greater than the value of $E_e^c$ for $f_0 = 0.01$ for smaller values of $l_3^0/r_0$, whereas for greater values of $l_3^0/r_0$ the value of $E_e^c$ for $f_0 = 0.1$ is smaller than the value of $E_e^c$ for $f_0 = 0.01$, as shown in Fig. 4.9(b) for $n = 5$ and in Fig. 4.9(c) for $n = 7$. For relatively higher values of $\chi$, Pardoen and Hutchinson [61] also found a smaller strain to coalescence with a smaller $f_0$ for a fixed initial void spacing but with $L = -1$.

### 4.3.3. Stress Distributions

Figs. 4.10 and 4.11 show stress concentrations, the ratio of $\sigma_{11}$ to Mises effective stress $\Sigma_e$ for several calculations. With $N_1$ constant, the values of $\Sigma_i$ and $\Sigma_e$ increase with the increasing creep strain due to the change in cross-sectional area.

The distribution of $\sigma_{11}/\Sigma_e$ is shown in Fig. 4.10(a) for $L = -1$ and for a unit cell with $f_0 = 0.01$ and $l_3^0/r_0 = 0.43$. After the first elastic step where $E_e = 0$, the maximum value of

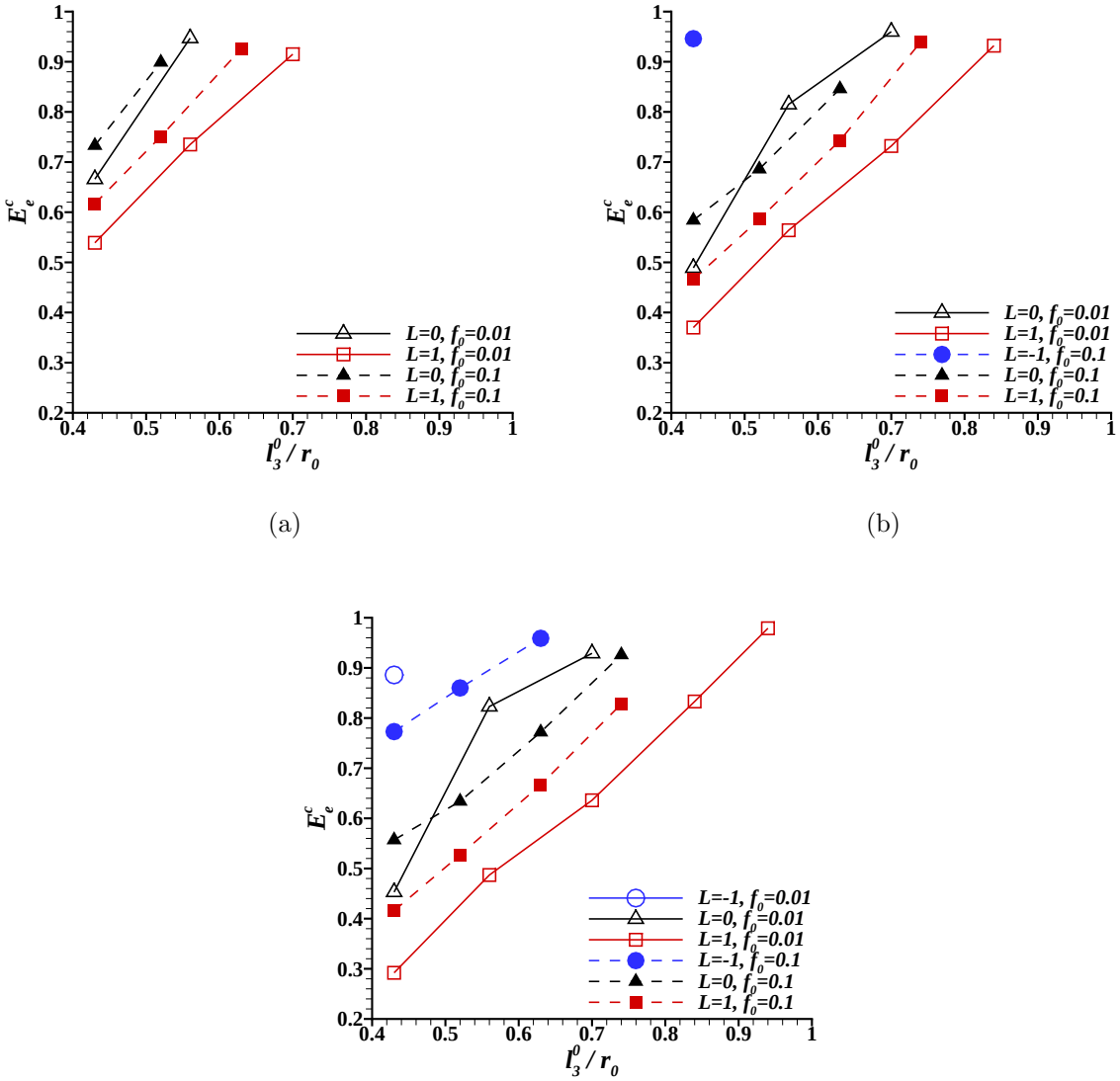


FIGURE 4.9. Critical strain to coalescence, $E_e^c$, for initial void volume fraction $f_0 = 0.1$ (open symbols); $f_0 = 0.01$ (closed symbols); for various initial inter-void ligament to void radius ratio $l_3^0/r_0$ for creep exponents (a) $n = 3$, (b) $n = 5$ and (c) $n = 7$. Stress triaxiality $\chi = 1/3$.

$\sigma_{11}/\Sigma_e$ occurs at the circumference of the void on $x_2 - x_3$ plane and is 1.89. Initially, creep deformation gives rise to stress relaxation so that $\sigma_{11}/\Sigma_e = 1.55$ at $E_e = 0.3$. At $E_e = 0.8$ $\sigma_{11}/\Sigma_e = 1.59$ but the location of the maximum stress concentration has now shifted towards

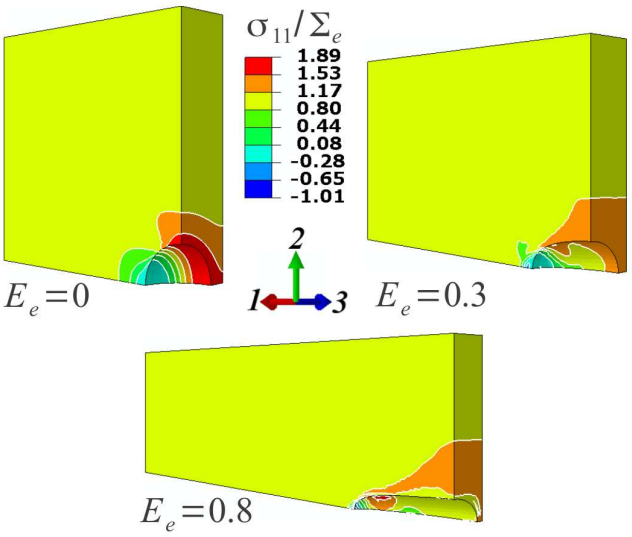


(a)

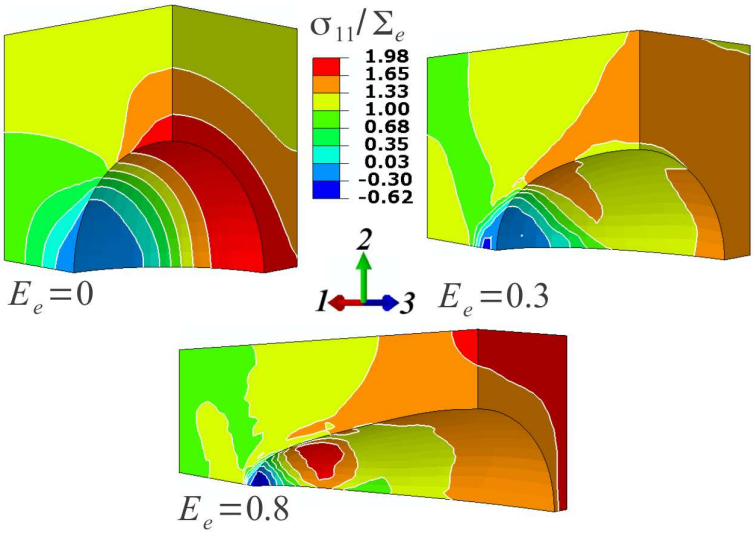


(b)

FIGURE 4.10. Distribution of normalized stress $\sigma_{11}/\Sigma_e$ after the first elastic step and at $E_e = 0.3$ and 0.8 for Lode parameter $L = -1$ and creep exponent $n = 5$. (a) Unit cell with $f_0 = 0.01$ and $l_3^0/r_0 = 0.43$. (b) Unit cell with $f_0 = 0.1$ and $l_3^0/r_0 = 0.43$. Stress triaxiality $\chi = 1/3$.

the tip of the void which has taken on a needle-like shape.

The corresponding evolution of the stress concentration with $f_0 = 0.1$ is shown in Fig. 4.10(b). Here, $\sigma_{11}/\Sigma_e = 1.98$ after the first elastic step, decreases to $\sigma_{11}/\Sigma_e = 1.59$ at

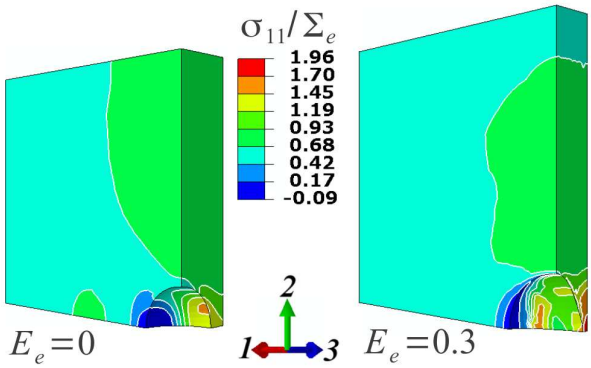


(a)

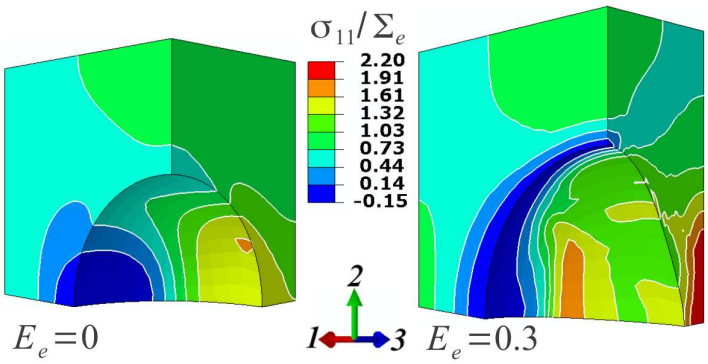


(b)

FIGURE 4.11. Distribution of normalized stress $\sigma_{11}/\Sigma_e$ after the first elastic step and at $E_e = 0.3$ for Lode parameter $L = 1$ and creep exponent $n = 5$. (a) Unit cell with $f_0 = 0.01$ and $l_3^0/r_0 = 0.43$. (b) Unit cell with $f_0 = 0.1$ and $l_3^0/r_0 = 0.43$. Stress triaxiality $\chi = 1/3$.

$E_e = 0.3$ and then increases to $\sigma_{11}/\Sigma_e = 1.82$ at $E_e = 0.8$ where the initially spherical void has evolved into a prolate spheroid and the stress concentration is nearly constant over much of the $x_2 - x_3$ cross section. For both $f_0 = 0.01$ and $f_0 = 0.1$, $\sigma_{11}/\Sigma_e$ is compressive at the tip of the elongated void.

For more widely spaced voids with $f_0 = 0.01$ the evolution of the void shape and the corresponding stress distributions for $L = -1$ are similar to those in Chapter 3 where the initially spherical void evolves into a needle-like shape and the maximum value of $\sigma_{11}/\Sigma_e$ is near, but not at, the tip of the needle-like void. On the other hand, for more widely spaced voids with $f_0 = 0.1$ the evolution of the void shape and the corresponding stress distributions

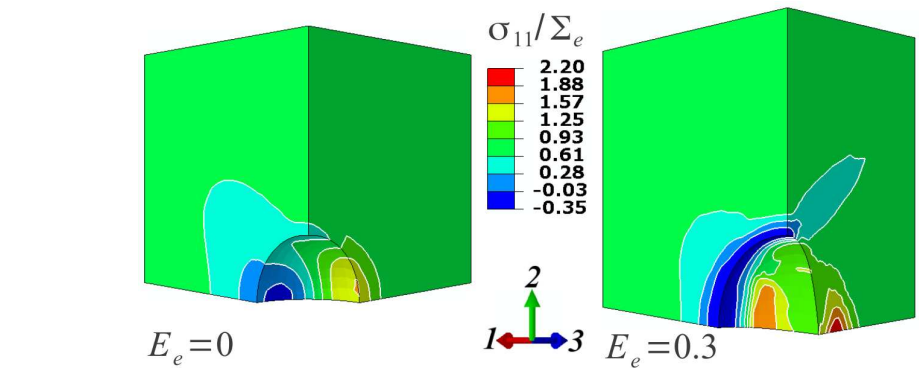


(a)

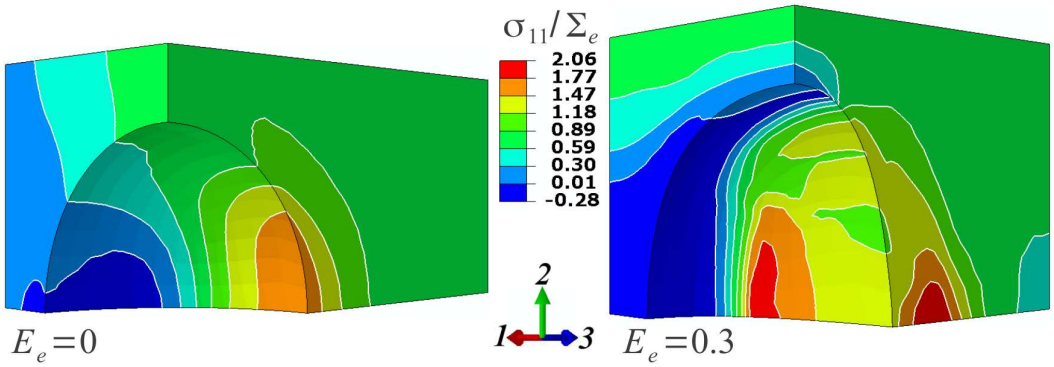


(b)

FIGURE 4.12. Distribution of normalized stress $\sigma_{11}/\Sigma_e$ after the first elastic step and at $E_e = 0.3$ for Lode parameter $L = 1$ and creep exponent $n = 5$. (a) Unit cell with $f_0 = 0.01$ and $l_3^0/r_0 = 2.75$. (b) Unit cell with $f_0 = 0.1$ and $l_3^0/r_0 = 1.74$. Stress triaxiality $\chi = 1/3$.

are qualitatively similar to those in Fig. 4.10.

For $L = 1$ and $l_3^0/r_0 = 0.43$, distributions of $\sigma_{11}/\Sigma_e$ are shown in Fig. 4.11(a) for the calculations with $f_0 = 0.01$. After the first elastic step the maximum value of $\sigma_{11}/\Sigma_e$ is 1.49 at the circumference of the void on $x_2 - x_3$ plane. At $E_e = 0.3$ the maximum stress concentration is 1.96 and is near the center of the ligament between adjacent voids along $x_3$ direction. In Fig. 4.11(b) where $f_0 = 0.1$ the initial value of the maximum stress concentration and the value at $E_e = 0.3$ are 1.62 and 2.2, respectively. Thus, in this case the evolving void shape leads to a stress concentration that is greater than the initial elastic

one. As shown in Fig. 4.11, $\sigma_{11}/\Sigma_e$ at $E_e = 0.3$ is compressive at the void circumference on $x_1 - x_2$ plane.

Figure 4.12(a) shows distributions of $\sigma_{11}/\Sigma_e$ for $f_0 = 0.01$ and $l_3^0/r_0 = 2.75$ while Fig. 4.12(b) shows corresponding distributions for $f_0 = 0.1$ and $l_3^0/r_0 = 1.74$. After first elastic step the maximum value of $\sigma_{11}/\Sigma_e$ is 1.58 in Fig. 4.12(a) and 1.65 in Fig. 4.12(b). For both the unit cells the maximum value occurs at the void circumference on $x_2 - x_3$ plane as in Fig. 4.11 for $l_3^0/r_0 = 0.43$. At $E_e = 0.3$ the maximum value of $\sigma_{11}/\Sigma_e$ is 2.20 for $f_0 = 0.01$ and $l_3^0/r_0 = 2.75$, and is 2.06 for $f_0 = 0.1$ and $l_3^0/r_0 = 1.74$. For $L = 1$ and larger values of $l_3^0/r_0$, the void collapses in the $x_3$ direction and the maximum value of $\sigma_{11}/\Sigma_e$ occurs on the $x_2 - x_3$ plane but has slightly shifted away from the void surface. As the void collapses, the void shape tends toward a penny-shaped crack and the stress concentration increases near, but not at, the tip of the collapsing void.

## 4.4. Discussion

With void coalescence and void collapse as defined in Section 4.3, the results for void coalescence and void collapse are summarized for an initial void volume fraction $f_0 = 0.01$ in Fig. 4.13 and for $f_0 = 0.1$ in Fig. 4.14. For $L = 1$ and $L = 0$, a transition from void coalescence to void collapse takes place with increasing initial inter-void spacing, $l_3^0/r_0$. There is a sharper transition from void coalescence to void collapse for $L = 1$ than for $L = 0$. Also, for $L = 1$ and $L = 0$ an increase in the value of the creep exponent $n$ results in void coalescence occurring at a larger value of $l_3^0/r_0$. As a consequence, the transition to void collapse takes place at a larger value of $l_3^0/r_0$. Void collapse did not occur for $L = -1$ in the calculations here. Indeed, void collapse did not occur for an isolated void in the analyses of Budiansky at al. [81] for $\chi = 1/3$ and $L = -1$. For a unit cell with $f_0 = 0.1$ and $l_3^0/r_0 = 1.74$ (where $l_2^0/r_0 = 0.38$) void coalescence for $L = -1$ and $n = 7$ occurred in the $x_2$ direction and this case is marked with a solid triangle in Fig. 4.14(c). In this calculation, the minimum value of $l_i^0/r_0$ which is $l_2^0/r_0$ falls within the range of values for which coalescence is expected.

In axisymmetric analyses for a nearly rate independent viscoplastic solid Koplik and Needleman [58] found that a transition to an overall uniaxial straining mode could occur

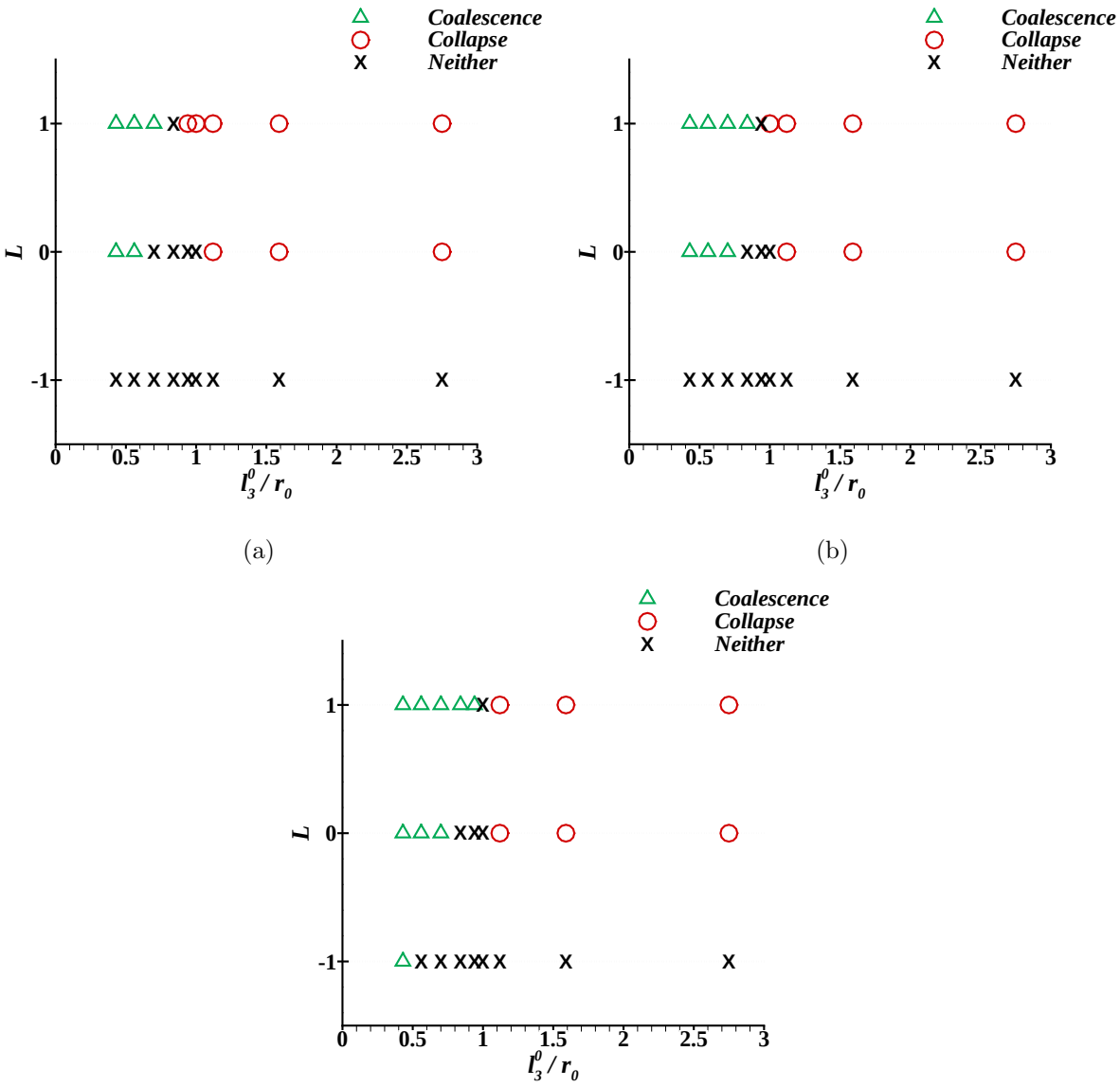


FIGURE 4.13. The dependence of void collapse or coalescence on initial void spacing and Lode parameter $L$ for an initial void volume fraction of $f_0 = 0.01$; stress triaxiality $\chi = 1/3$; and three creep exponents (a)$n = 3$, (b)$n = 5$ and (c)$n = 7$. Here $l_3^0/r_0 = a_3^0/r_0 - 1$ is the initial inter-void ligament (in $x_3$ direction) to void radius ratio.

and that was associated with the onset of void coalescence. Such a transition to an overall uniaxial straining mode was not obtained for low stress triaxiality values at least for small

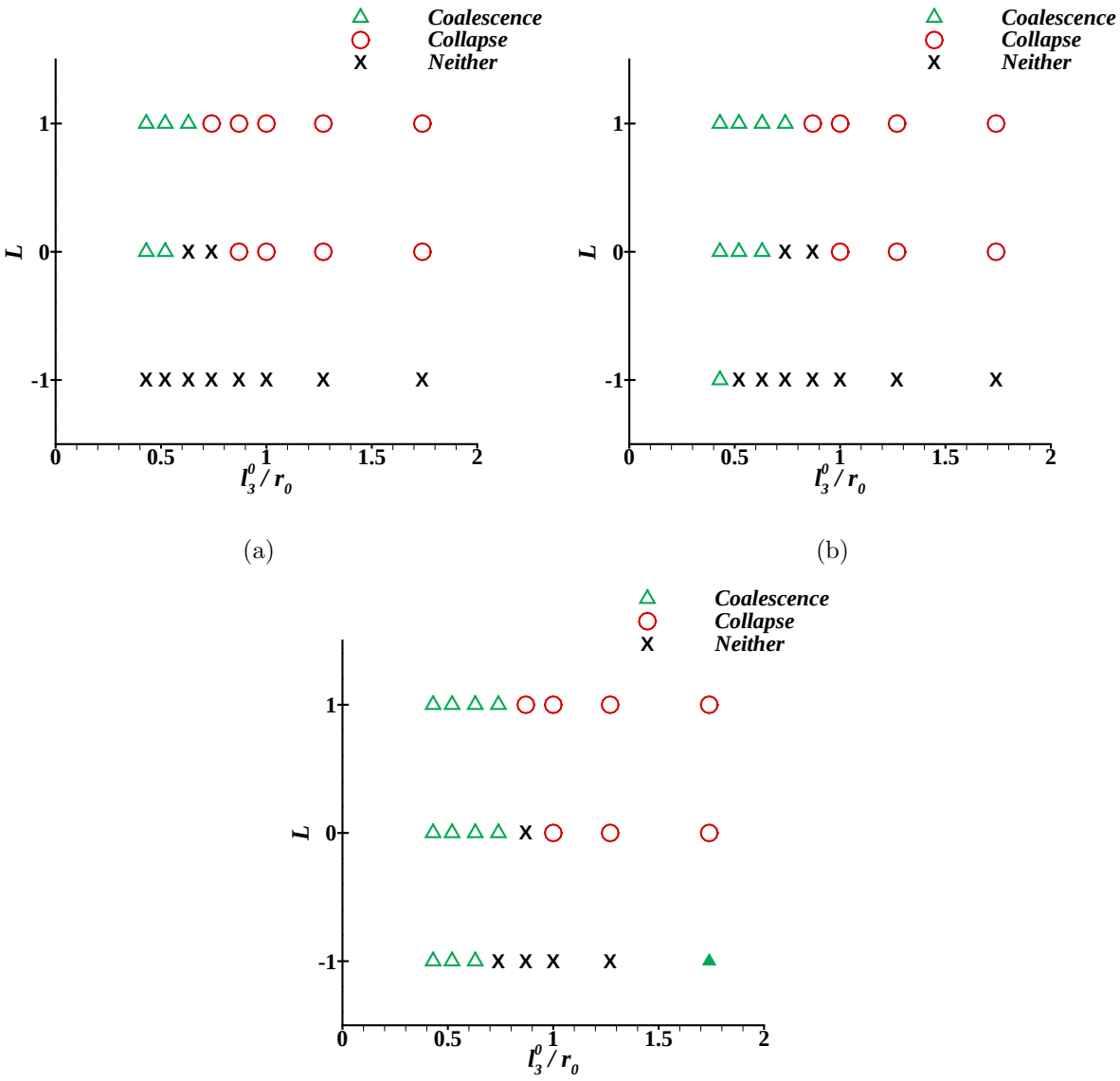


(a)

(b)

(c)

FIGURE 4.14. The dependence of void collapse or coalescence on initial void spacing and Lode parameter $L$ for an initial void volume fraction of $f_0 = 0.1$; stress triaxiality $\chi = 1/3$; and three creep exponents (a)$n = 3$, (b)$n = 5$ and (c)$n = 7$. Here $l_3^0/r_0 = a_3^0/r_0 - 1$ is the initial inter-void ligament (in $x_3$ direction) to void radius ratio.

initial void volume fractions, e.g. [58, 61, 102, 103, 64, 94]. In the calculations here a transition to such an overall uniaxial straining mode (i.e., $da_3/dE_3 \approx 0$) did not occur

even for an initial void volume fraction of $f_0 = 0.1$ and with an initial inter-void spacing of $l_3^0/r_0 = 0.43$. This can probably be attributed to the highly rate dependent material response in the calculations here which significantly delays localization [104]. In the calculations here coalescence is defined in terms of a reduction in ligament size. In some cases although $r_3/r_0$ initially decreases, it increases beyond some overall strain value leading to coalescence. This occurs mainly in calculations with $L = 1$ and $L = 0$ but also occurred for $L = -1$ for sufficiently closely spaced voids with $f_0 = 0.1$.

For $L = 1$ and $L = 0$ when void coalescence occurred, it occurred in the direction of the minimum applied stress ($x_3$), regardless of the initial inter-void spacing in the other directions. For $L = -1$ ($\Sigma_1 > \Sigma_2 = \Sigma_3$), void coalescence occurred in either the $x_2$ or the $x_3$ direction depending on which initial inter-void spacing was smaller. Gologanu et al. [102] refer to the mode of coalescence with $L = -1$ as coalescence in layers whereas Gologanu et al. [103] refer to the mode of coalescence with $L = 1$ as coalescence in columns. In [81, 103, 101] and in Chapter 3 void collapse was seen along the direction of the minimum applied stress for $\chi = 1/3$ and $L > -1$. In the calculations here, when void collapse occurred, it occurred along the direction of the minimum applied stress ($x_3$ in the calculations here), regardless of the initial inter-void ligament size in the other directions. Here, both void coalescence and void collapse occurred along the ligament with the minimum applied stress for $L > -1$. Hence the transition from void coalescence to void collapse depends on the void spacing in the minimum applied stress direction.

Danas and Aravas [100] (also see [101]) proposed a failure criterion involving void collapse based on a void aspect ratio where the smallest void radius was in the denominator becoming unbounded in the plane normal to the collapse direction (the $x_3$ direction here). The voids then link up parallel to the major loading direction leading to a loss of load carrying capacity. Recently, in an analysis of a rate independent solid subject to a monotonically increasing load [105] noted that the average stress continues to increase even after void collapse ($f \approx 0$) so that void collapse is not associated with a loss of load carrying capacity. In the cell model calculations here the stresses in the $x_1 - x_2$ plane along the mid-section

of the collapsing void are generally compressive. However, as the void collapses, a stress concentration develops near, but not at, the tip of the collapsing void which can then trigger cracking as seen in the experiments in Chapter 2.

## 4.5. Summary and Conclusions

Three dimensional cell model analyses for an array of initially spherical voids in an fcc single crystal has been carried out. The crystals were subjected to creep loading with a constant nominal tensile stress and with the stress triaxiality fixed at 1/3. Calculations were carried out for Lode parameter values of $-1, 0$ and 1; creep exponent values of $3, 5$ and 7; initial void volume fractions of 0.01 and 0.1; and for a range of initial void spacings. The calculations were continued until one of the following conditions was met: (i) void coalescence; a minimum relative void spacing of $l_i^r = l_i/l_i^0 < 0.2$; (ii) void collapse; a relative void volume fraction $f/f_0 \approx 0$ or $f/f_0$ decreasing monotonically and sufficiently rapidly between $E_e \approx 0.5$ and $E_e = 1$; or (iii) neither void coalescence or void collapse up to an overall effective creep strain $E_e = 1.0$.

The calculations showed that:

- For Lode parameter values $L = 0$ and $L = 1$ a transition between void collapse for widely spaced voids to coalescence for closely spaced voids occurred.
  - This transition was observed for all three values of the creep exponent and both initial void volume fractions.
  - This transition is rather sharp and occurs at an initial relative void spacing, $l_3^0/r_0$, in the range of $0.7 - 1.0$.
  - Larger values of the creep exponent gave rise to void coalescence for larger initial void spacings. Consequently this transition occurred at larger initial void spacings for greater values of the creep exponent.
- For $L = -1$ a transition between void growth and void collapse was not observed for the range of initial void spacings considered. Indeed, void collapse for $L = -1$ was not observed for an isolated void in [81].

  - For $f_0 = 0.01$ and $n = 7$, void coalescence occurred due to a gradual reduction in the inter-void ligament size for very closely spaced voids.
  - For $f_0 = 0.10$ and $n = 5, 7$ values, accelerated void coalescence occurred for very closely spaced voids.
  - The effect of the creep exponent on the evolution of void volume fraction decreases with increasing initial void spacings.
- An abrupt transition to an overall plane strain mode of deformation in the ligament between coalescing voids did not occur. However, for closely spaced voids a rapid increase in the void radius along the direction of minimum applied stress (or along the direction of minimum initial void spacing for $L = -1$) could occur resulting in an accelerated reduction in ligament size.
- The strain to void coalescence is smaller with $f_0 = 0.01$ than with $f_0 = 0.10$ for $L = 1$. On the other hand, for $L = -1$ the situation is reversed. For $L = 0$ the strain to coalescence is smaller with $f_0 = 0.01$ for sufficiently closely spaced voids while for voids that are sufficiently far apart the strain to coalescence is smaller with $f_0 = 0.10$.
- The strain to coalescence as well as the strain to collapse decreases with increasing creep exponent.
- Stress concentrations develop due to the change in void shape that can promote crack initiation from the void surface as shown in Chapter 2. In some cases the stress concentration that develops due to the evolving void shape is greater than the initial elastic stress concentration.

# CHAPTER 5

# PHENOMENOLOGICAL MODELING OF THE EFFECT OF SPECIMEN THICKNESS ON THE CREEP RESPONSE OF NI-BASED SUPERALLOY SINGLE CRYSTALS

## 5.1. Introduction

As discussed in Chapter 2 creep tests on single crystal Ni-based superalloys show increased creep strain rates and/or decreased creep rupture strains and times for thinner specimens. This is known as the thickness debit effect. Also it is shown in Chapter 2 that depending on the creep test condition both bulk and/or surface damage mechanisms can contribute to the thickness debit effect.

A quantitative mechanistic model that can account for both bulk and surface damage effects and that assesses their relative roles is not currently available. Here, a simple phenomenological nonlinear parallel spring model for uniaxial creep with springs representing the bulk and possible surface damage layers is proposed. The nonlinear spring constitutive relations model both material creep and evolving damage. The model draws on the experimental observations in Chapter 2 and the detailed finite element calculations in Chapters 3 and 4. Numerical results are presented and a quantitative comparison is made with the experimental results in Chapter 2 and Ref. [10] for the thickness dependence of the creep strain rate and/or the creep rupture strain and time under two loading conditions; a low temperature high stress condition, 760°C/758MPa; and a high temperature low stress condition, 982°C/248MPa.

## 5.2. Model Formulation

In this chapter a tensile specimen subjected to a fixed applied force $F$ is analyzed. The deformation and strain state is assumed to be uniform along the length of the specimen which, until near final fracture, is consistent with the results in Chapter 2. Hence, only a single cross section is considered. The average nominal stress acting on the cross section is $s = F/A_0$, with $A_0$ the initial cross sectional area, and the average true stress is $\sigma = F/A$, with $A$ the current cross sectional area. Elasticity is neglected and the creep strain rate $\dot{\varepsilon}$

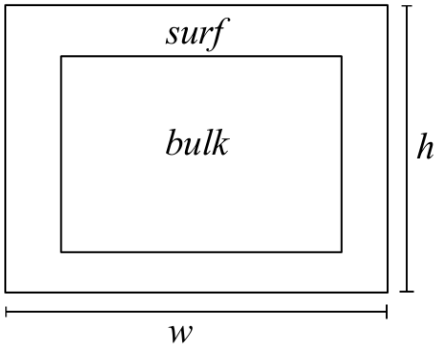


FIGURE 5.1. Schematic of the cross section of the specimen showing the bulk and the surface region (surf); $w$ and $h$ are the initial dimensions of the cross section.

is taken to be uniform in the cross section. The cross section is taken to consists of a bulk region and a surface region as shown in Fig. 5.1.

The current load bearing cross sectional area $A$ evolves as

$$\dot{A} = \dot{A}_{\text{bulk}} + \dot{A}_{\text{surf}} \tag{49}$$

where $A_{\text{bulk}} = A_0$ and $A_{\text{surf}} = 0$ at $t = 0$. The evolution equations for the bulk and surface area need to be specified which strongly depend on the active damage mechanisms.

The creep strain rate is given by

$$\dot{\varepsilon} = (1 - \beta)\, C_p \sigma^m + \beta C_s \sigma^n \tag{50}$$

and the quantity $\beta$ evolves as

$$\dot{\beta} = \frac{1}{t_0}\,(1 - \beta) \tag{51}$$

with initial condition that $\beta = 0$ at $t = 0$ and $t_0$ a time constant that governs the transition from primary to secondary creep.

In Eq. (50) $m$ is the primary creep exponent, $n$ is the secondary creep exponent and $C_p$ and $C_s$ are parameters of the cross section that characterize the creep resistance in primary and secondary creep, respectively. For specifying parameter values it is convenient

to write

$$C_p = \dot{\varepsilon}_p \left(\frac{1}{\sigma_p}\right)^m, \; C_s = \dot{\varepsilon}_s \left(\frac{1}{\sigma_s}\right)^n \tag{52}$$

and to specify the values of $\dot{\varepsilon}_p$, $\sigma_p$ and $\dot{\varepsilon}_s$, $\sigma_s$ individually.

The calculations proceeds as follows: a fixed tensile force $F$ is applied and a time step $\Delta t$ is chosen. At each time step, the strain increment $\Delta\varepsilon = \dot{\varepsilon}\Delta t$ and the area changes $\Delta A_{\text{bulk}} = \dot{A}_{\text{bulk}}\Delta t$ and $\Delta A_{\text{surf}} = \dot{A}_{\text{surf}}\Delta t$ are calculated and the average true stress $\sigma$ is updated. The evolution equations for $C_p$ and $C_s$ differ for the low temperature high stress and high temperature low stress cases.

5.2.1. Low Temperature High Stress

Since no surface damage was observed at 760°C, $\dot{A}_{\text{surf}} = 0$ so that $\dot{A} = \dot{A}_{\text{bulk}}$ in Eq. (49). The damage mechanism modeled is loss of bulk area due to cleavage-like cracking emanating from the preexisting voids.

The bulk crystal material is regarded as incompressible, $\dot{A}_{\text{bulk}}/A_{\text{bulk}} = -\dot{\varepsilon}$, the rate of change of load bearing bulk cross sectional area is written as,

$$\dot{A}_{\text{bulk}} = -\dot{\varepsilon}A_{\text{bulk}} - \dot{D}_{\text{clv}} \tag{53}$$

where $\dot{D}_{\text{clv}}$ is the rate of loss of area due to cleavage-like cracking. It is assumed here that the nucleation of cleavage-like cracks follows Weibull statistics, Ref. [106], and that a crack of fixed length nucleates. The cumulative distribution function for the Weibull distribution as a function of true stress $\sigma$ is

$$p(\sigma) = 1 - \exp\left[-\left(\frac{\sigma}{\lambda}\right)^k\right] \tag{54}$$

where $\lambda$ is the scale factor and $k$ is the shape factor of the distribution.

The cleavage-like cracking is assumed to begin in the secondary creep regime which is approximately $\varepsilon > 0.07$, Chapter 2. Then, at each strain increment $\Delta\varepsilon = \dot{\varepsilon}\Delta t = 0.001$ a random number $R$ is generated where $R \in [0, 1]$ and

$$\dot{D}_{\rm clv} = \begin{cases} a_c\dot{\varepsilon} & \text{for} \quad R \le p \\ 0 & \text{for} \quad R > p \end{cases} \tag{55}$$

so that the reduction in cross sectional area due to cleavage-like cracking for a given time step in the secondary creep regime is $\Delta D_{\rm clv} = \dot{D}_{\rm clv}\Delta t = a_c\Delta\varepsilon$ if $R \le p$ or else no loss of area due to damage occurs in that increment.

The parameter $a_c$ in Eq. (55) is taken such that $\Delta D_{\rm clv} = 0.03{\rm mm}^2$ per $\Delta\varepsilon = 0.001$ if $R \le p$. This corresponds to the nucleation of about 100 annular cracks extending $\approx 7\mu$m from the void surface. The initial void volume fraction in the undeformed specimen corresponds to several hundred micro-voids, Refs. [53, 107], and, multiple cracks can initiate from each micro-void.

The parameter values defining $C_p$ and $C_s$ in Eq. (52) are $\sigma_p = \sigma_s = 900$MPa, $\dot{\varepsilon}_p = 5 \times 10^{-6}{\rm sec}^{-1}$, $m = 1$, $\dot{\varepsilon}_s = 4.5 \times 10^{-8}{\rm sec}^{-1}$ and $n = 5$. The time constant in Eq. (51) is $t_0 = 1.48{\times}10^4$sec. These values are chosen to give a good representation of the experimentally observed primary and secondary creep strain versus time response given in Chapter 2.

The observations in Chapter 2 do not give a direct basis for choosing the parameters in Eq. (54). Here, $\lambda = \sigma_p = \sigma_s$ is taken, which is about 0.9 times the effective yield strength of PWA1484 at 760°C reported in Ref. [15]. For the specified value of $\lambda$, $k \approx 10$ gives a value of $p$ that tends to one as $\sigma$ approaches the effective yield strength and leads to a reasonably good fit to the experimental data for the evolution of the creep strain.

5.2.2. High Temperature Low Stress

Surface damage due to oxidation, nucleation of new voids and cleavage-like cracking emanating from the deformed voids are active damage mechanisms in the high temperature low stress loading condition. The oxide layer is taken to carry no load so that only the cross sectional areas of the $\gamma'$-precipitate free region, $A_{\rm L1}$, and of the $\gamma'$-precipitate reduced region, $A_{\rm L2}$, contribute to the load bearing surface cross sectional area, $A_{\rm surf}$ in Eq. (49). Hence,

$$\dot{A}_{\rm surf} = \dot{A}_{\rm L1} + \dot{A}_{\rm L2} \tag{56}$$

where $A_{\mathrm{L1}} = A_{\mathrm{L2}} = 0$ at $t = 0$.

The depletion of the $\gamma'$-precipitate is due to surface oxidation as noted in Chapter 2 hence the cross sectional area of these two layers can be assumed to be proportional to the cross sectional area of the oxide layer, $A_{\mathrm{oxide}}$. As shown in Chapter 2, void nucleation was seen in both the $\gamma'$-precipitate free and in the $\gamma'$-precipitate reduced regions. Hence, the load carrying cross sectional area of these two regions evolve as

$$\dot{A}_{\mathrm{L1}} = \alpha^{\mathrm{L1}} \dot{A}_{\mathrm{oxide}} - A_{\mathrm{L1}} \dot{D}_{\mathrm{void}} \quad , \quad \dot{A}_{\mathrm{L2}} = \alpha^{\mathrm{L2}} \dot{A}_{\mathrm{oxide}} - A_{\mathrm{L2}} \dot{D}_{\mathrm{void}} \tag{57}$$

where $\alpha^{\mathrm{L1}}$ and $\alpha^{\mathrm{L2}}$ are the proportionality constants; and $\dot{D}_{\mathrm{void}}$ is the rate of homogeneous nucleation of voids.

The void nucleation rate is taken to be strain controlled and to have a normal distribution about a mean nucleation strain $\varepsilon_N$ as in Ref. [108]

$$\dot{D}_{\mathrm{void}} = \frac{D_N}{s_N \sqrt{2\pi}} \exp\left[ -\frac{1}{2} \left( \frac{\varepsilon - \varepsilon_N}{s_N} \right)^2 \right] \dot{\varepsilon} \tag{58}$$

where $D_N$ is the maximum area fraction of cross sectional area that can be lost due to void nucleation and $s_N$ is the standard deviation.

The solid state diffusion is in general the rate limiting step for oxidation reactions and the oxidation kinetics are reasonably well approximated using a parabolic fit, Refs. [109, 110], so that the thickness $x$ of the oxide layer at any given time $t$ is

$$x = k_p t^{1/2} \tag{59}$$

The cross sectional area $A_{\mathrm{oxide}}$ evolves as

$$\dot{A}_{\mathrm{oxide}} = \dot{x} P_0 - 8 x \dot{x} \tag{60}$$

Here, $P_0 = 2\,(w + h)$ is the initial perimeter of the cross section with initial dimensions $w$ and $h$, see Fig. 5.1.

With the bulk crystal material regarded as incompressible, the time rate of change of the load bearing bulk cross sectional area is given by

$$\dot{A}_{\mathrm{bulk}} = -\dot{\varepsilon} A_{\mathrm{bulk}} - A_{\mathrm{bulk}} \dot{D}_{\mathrm{void}} - \dot{D}_{\mathrm{clv}} - \dot{A}_{\mathrm{oxide}} \left( 1 + \alpha^{\mathrm{L1}} + \alpha^{\mathrm{L2}} \right) \tag{61}$$

where $A_{\text{bulk}} = A_0$ at $t = 0$, $\dot{D}_{\text{void}}$ is given by Eq. (58) and $\dot{D}_{\text{clv}}$ is given by Eqs. (54) and (55) and $\dot{A}_{\text{oxide}}$ is given by Eq. 60.

Thus, the time rate of change of the total load bearing cross sectional area $A$ is

$$\dot{A} = \dot{A}_{\text{L1}} + \dot{A}_{\text{L2}} + \dot{A}_{\text{bulk}} \tag{62}$$

In the high temperature low stress loading condition primary creep was negligible hence $\beta = 1$ in Eq. (51). A power law creep relation is then taken to hold for each of $A_{\text{L1}}$, $A_{\text{L2}}$ and $A_{\text{bulk}}$. Since each sub-area is assumed to undergo power law creep with the same creep exponent $n$, the overall creep relation has the form

$$\dot{\varepsilon} = C_s \sigma^n \tag{63}$$

where $C_s$ is the collective creep resistance of the total load bearing cross section.

Each sub-area is regarded as deforming homogeneously with each planar cross section remaining planar so that $\dot{\varepsilon}_{\text{L1}} = \dot{\varepsilon}_{\text{L2}} = \dot{\varepsilon}_{\text{bulk}} = \dot{\varepsilon}$. The overall stress in each of the sub-areas is related to the strain rate by

$$\sigma_{\text{bulk}} = \left(\frac{\dot{\varepsilon}}{C_s^{\text{bulk}}}\right)^{1/n} \ , \ \sigma_{\text{L1}} = \left(\frac{\dot{\varepsilon}}{C_s^{\text{L1}}}\right)^{1/n} \ , \ \sigma_{\text{L2}} = \left(\frac{\dot{\varepsilon}}{C_s^{\text{L2}}}\right)^{1/n} \tag{64}$$

where $C_s^{\text{bulk}}$ is the creep resistance of the bulk region, $C_s^{\text{L1}}$ is the creep resistance of the $\gamma'$-precipitate free region and $C_s^{\text{L2}}$ is the creep resistance of the $\gamma'$-precipitate reduced region.

The total force acting on the cross sectional area is $F = A_{\text{bulk}}\sigma_{\text{bulk}} + A_{\text{L1}}\sigma_{\text{L1}} + A_{\text{L2}}\sigma_{\text{L2}}$. The overall response is regarded as three non-linear springs in parallel so that average true stress $\sigma$ is given by

$$\sigma = \frac{A_{\text{bulk}}}{A}\sigma_{\text{bulk}} + \frac{A_{\text{L1}}}{A}\sigma_{\text{L1}} + \frac{A_{\text{L2}}}{A}\sigma_{\text{L2}} \tag{65}$$

From Eqs. (63), (64) and (65), the overall section creep resistance $C_s$ is

$$\frac{1}{C_s} = \left[\frac{A_{\text{L1}}}{A\left(C_s^{\text{L1}}\right)^{1/n}} + \frac{A_{\text{L2}}}{A\left(C_s^{\text{L2}}\right)^{1/n}} + \frac{A_{\text{bulk}}}{A\left(C_s^{\text{bulk}}\right)^{1/n}}\right]^n \tag{66}$$

The creep exponent $n = 5$ and the other parameters defining $C_s^{\text{L1}}$, $C_s^{\text{L2}}$ and $C_s^{\text{bulk}}$ are $\dot{\varepsilon}_s^{\text{L1}} = \dot{\varepsilon}_s^{\text{L2}} = \dot{\varepsilon}_s^{\text{bulk}} = 1.6 \times 10^{-6}\text{sec}^{-1}$ and $\sigma_s^{\text{L1}} = 150\text{MPa}$, $\sigma_s^{\text{L2}} = 300\text{MPa}$ and $\sigma_s^{\text{bulk}} =$

600MPa respectively. The value of $C_s^{\text{bulk}}$ was chosen to give a good representation of the experimentally observed creep strain versus time response up to 1% creep strain in Ref. [10]. The values of $C_s^{\text{L1}}$ and $C_s^{\text{L2}}$ were chosen to represent a decrease in creep strength with precipitate depletion as also presumed in Ref. [37].

The values used in the calculations for $k_p = 4 \times 10^{-5}$mm sec$^{-1/2}$, $\alpha^{\text{L1}} = 0.5$ and $\alpha^{\text{L2}} = 0.25$ give oxide layer, $\gamma'$-precipitate free layer and $\gamma'$-precipitate reduced layer sizes close to those seen in Chapter 2. Also, the values $D_N = 0.5$, $s_N = 0.01$ and $\varepsilon_N = 0.012$ used in Eq. (58) give an increase in porosity similar to that observed in Chapter 2. As in the low temperature high stress calculations, $\lambda = \sigma_s^{\text{bulk}}$ is taken, which is about 0.9 times the effective yield strength of the PWA1484 Ni-based single crystal superalloy at 982°C reported in Ref. [15], and $k = 10$ in Eq. (54). However, here the parameter $a_c$ in Eq. (55) is taken as $\Delta D_{\text{clv}} = 0.01\text{mm}^2$ per $\Delta\varepsilon = 0.001$ if $R \leq p$ because smaller length cracks were seen to nucleate at high temperature low stress creep in Chapter 2, as expected with the lower applied stress.

## 5.3. Results

The model formulation given in Section 5.2 was coded in a MATLAB [111] program. As in the experiments reported in Ref. [10] and in Chapter 2, five initial specimen thicknesses $h$ (see Fig. 5.1), 0.38mm, 0.51mm, 0.76mm, 1.52mm and 3.18mm are analyzed for low temperature high stress creep and four initial specimen thicknesses $h = 0.51$mm, 0.76mm, 1.52mm and 3.18mm for high temperature low stress creep. The initial specimen width $w = 4.75$mm is the same for all cases. The low temperature high stress creep calculations are carried out under a constant applied nominal stress of $s = 758$MPa and the high temperature low stress creep calculations are carried out under $s = 248$MPa as in Chapter 2. For each specimen thickness and creep condition 50 calculations are carried out. For given conditions, the results of each calculation depends on the random number generated at each step for Eq. (55) to determine the damage due to cleavage. The average values presented subsequently are averages over the 50 calculations and the error bars indicate the minimum and maximum values from the 50 calculations. In all calculations, the time step $\Delta t$ is adjusted to give a

fixed strain increment $\Delta\varepsilon = 0.001$. The time step $\Delta t$ varied from $0.05 - 0.06$hrs in the primary and tertiary creep regimes to a maximum of $8 - 9$hrs in the steady state creep regime.

The calculations are continued until one of two conditions is met: (i) a critical strain rate is attained; or (ii) there is a critical loss of area due to cleavage-like cracking. The critical strain rate condition is taken to be $\dot{\varepsilon} > \dot{\varepsilon}_{\text{fail}}$ where $\dot{\varepsilon}_{\text{fail}}$ is the maximum strain rate that can be sustained and the critical loss of area due to cleavage-like cracking is taken as $D_{\text{clv}} \geq D_{\text{fail}}$. In the calculations here the value of $\dot{\varepsilon}_{\text{fail}}$ differs for the low temperature high stress and the high temperature low stress conditions while $D_{\text{fail}} = 2\text{mm}^2$ for both loading conditions. It is assumed that this much loss of load bearing area due to crack nucleation will result in crack growth and crack coalescence leading to fracture. There is no basis from the experiments in Chapter 2 for choosing $\dot{\varepsilon}_{\text{fail}}$ or $D_{\text{fail}}$. The values used give a reasonable quantitative fit to the failure data shown in Chapter 2.

5.3.1. Low Temperature High Stress

The value of $\dot{\varepsilon}_{\text{fail}}$ is taken to be $10\dot{\varepsilon}_{ss}$ where $\dot{\varepsilon}_{ss}$ is the creep rate taken at the beginning of steady state/secondary creep, which is taken as $\varepsilon = 0.07$.

The calculated creep strain, $\varepsilon$, versus time, $t$, curves for specimen thicknesses $h =$ 3.18mm and 0.38mm are shown in Fig. 5.2 together with the experimental curves from Ref. [10]. The average value for both specimen thicknesses shows a very good correlation with the experimental curve. As seen in Fig. 5.2 the spread in the evolution of creep strain with time for the thinner specimens can be seen when $\varepsilon > 0.07$. For the thicker specimens the spread in the evolution of creep strain is small until $\varepsilon \approx 0.1$. The calculations for the specimens with thickness $h = 3.18$ and 1.52mm are terminated after attaining $D_{\text{fail}}$ for all 50 calculations whereas the calculations for the specimens with $h = 0.76$, 0.51, and 0.38mm are terminated after attaining $\dot{\varepsilon}_{\text{fail}}$.

Figure 5.3 shows the time evolution of the Weibull cumulative distribution function, $p$, i.e. the probability of crack nucleation and the cumulative loss of area normalized by the initial cross sectional area, $D_{\text{clv}}/A_0$, for all specimen thicknesses $h$ analyzed. In Fig. 5.3a,

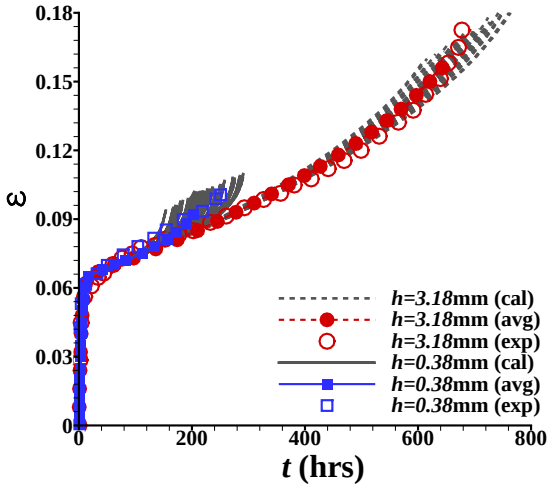


FIGURE 5.2. Comparison of the calculated creep curves for 50 calculations (cal) and their average (avg) with the experimental (exp) creep curves from Ref. [10] of specimens with thickness $h = 3.18$mm and 0.38mm at low temperature high stress creep. Where $\varepsilon$ is the logarithmic creep strain.

$p$ starts with a small initial value of 0.3 at $t \approx 62.5$hrs (crack nucleation begins in the secondary creep regime). In Fig. 5.3b, $D_{\text{clv}}/A_0$ increases with time, which raises the stress level on the remaining intact area and hence increases the probability, $p$, of further crack nucleation. This deleterious effect is more detrimental for thinner specimens leading to an increased fraction of the cross sectional area being lost by cleavage-like cracks as observed experimentally in Chapter 2. Regardless of the criterion by which the specimen fails, the probability of crack nucleation for all specimens is near unity prior to final failure.

Figure 5.4 shows the effect of specimen thickness on the creep strain to fracture, $\varepsilon_f$, and on the time to fracture, $t_f$, for the low temperature high stress creep loading condition. Both the results of the model predictions and the experimental data from Ref. [10] and Chapter 2 are shown. The average values of $\varepsilon_f$ and $t_f$ follow a $1/\sqrt{h}$ dependence as also seen in the experimental results of Chapter 2.

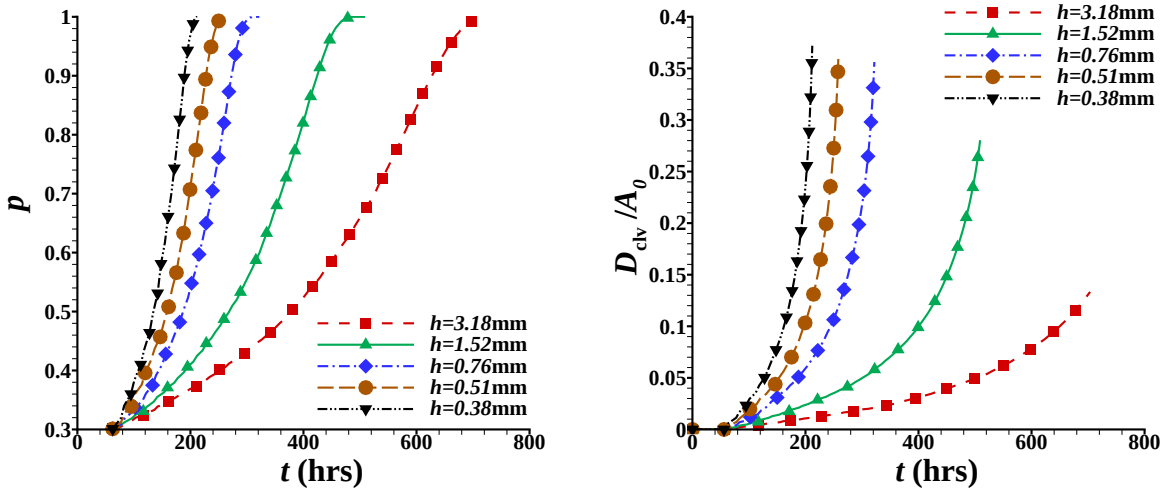


(a) (b)

FIGURE 5.3. Evolution of (a) Weibull cumulative distribution function ($p$) and (b) cumulative loss of area due to cleavage-like cracking normalized with the initial cross sectional area of the specimen ($D_{\text{clv}}/A_0$) at low temperature high stress creep for various specimens with thickness $h$. The values are averaged over 50 calculations.

### 5.3.2. High Temperature Low Stress

In the high temperature low stress creep condition there is no primary creep and $\dot{\varepsilon}_{\text{fail}}$ is taken to be $10\dot{\varepsilon}_N$ where $\varepsilon_N$ is the mean strain for void nucleation in Eq. (58).

The calculated creep strain, $\varepsilon$, versus time, $t$, curves for specimen thicknesses $h =$ 3.18mm and 0.76mm together with the experimental results from Ref. [10] are shown in Fig. 5.5. The average values for the specimens show a very good correlation with the experimental curve. In contrast to the low temperature high stress creep case, the deviation of each of the 50 calculations from the mean creep strain versus time curve is small. All specimens failed by attaining $\dot{\varepsilon}_{\text{fail}}$.

The evolution of the oxide layer thickness, $x$, with time, $t$, is shown in Fig. 5.6a. The evolution of the $\gamma'$-precipitate free and $\gamma'$-precipitate reduced regions are proportional to the evolution of the oxide layer. The evolution of $x$ only depends on time and hence at any

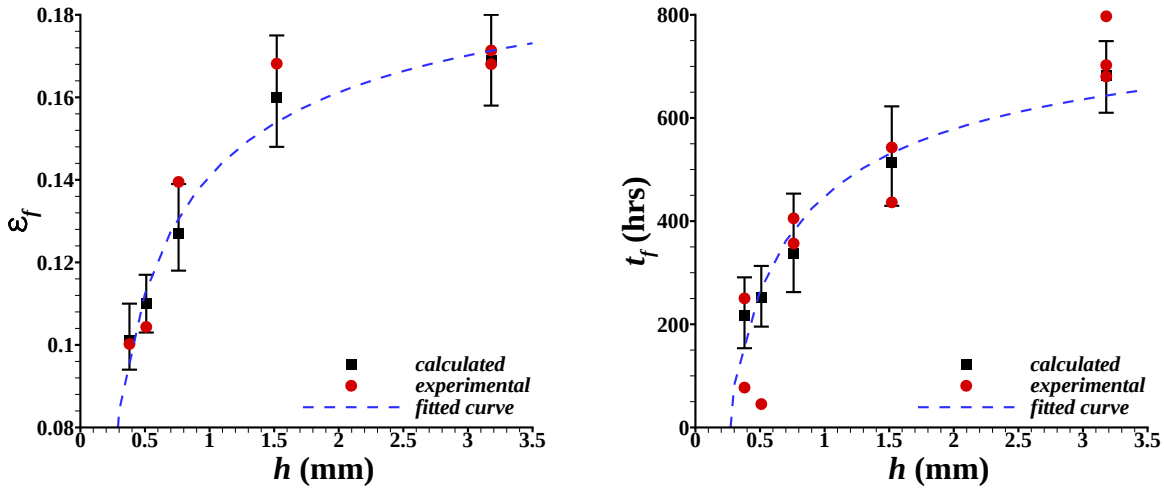


(a) (b)

FIGURE 5.4. The effect of specimen thickness ($h$) on (a) the creep strain to fracture ($\varepsilon_f$) and (b) the time to fracture ($t_f$, hrs) at low temperature high stress creep. Experimental data is taken from Ref. [10] and Chapter 2. The dashed line is a least-square fit of $a - b/\sqrt{h}$ to the mean value of the calculated $\varepsilon_f$ and $t_f$ data, where $a$ and $b$ are positive fitting constants and their values differ for $\varepsilon_f$ and $t_f$. The error bars show the maximum and minimum deviation over the mean value of 50 calculations.

given time $t$ the thickness of the oxide layer is the same for all the specimens resulting in a relatively greater loss of load bearing cross sectional area for thinner specimens than for thicker specimens. Also, the final thickness of the oxide layer depends on the failure time so that the specimens with longer creep life develop a thicker oxide scale. The extent of oxidation in Fig. 5.6a shows a very good correlation with the total thickness of oxide layers observed experimentally in Chapter 2.

The loss of area fraction of the bulk cross section due to homogeneous void nucleation, $D_{\text{void}}$, with time, $t$ is shown in Fig. 5.6b. There is an increase in void nucleation in the bulk of the thinner specimens prior to achieving a thickness independent saturation value of $D_{\text{void}}$ as shown in Fig. 5.6b. The dependence of $D_{\text{void}}$ on strain $\varepsilon$ is independent of the specimen

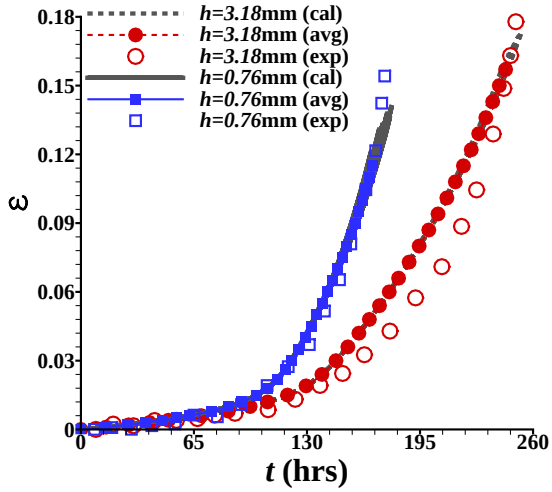


FIGURE 5.5. Comparison of the calculated creep curves for 50 calculations (cal) and their average (avg) with the experimental (exp) creep curves from Ref. [10] of specimens with thickness $h = 3.18$mm and 0.76mm at high temperature low stress creep. Where $\varepsilon$ is the logarithmic creep strain.

thickness since void nucleation is strain controlled, Eq. (58).

The time evolution of Weibull cumulative distribution function, $p$, i.e. the probability of crack nucleation is shown in Fig. 5.7a and the cumulative loss of area normalized with the initial cross sectional area of the specimen, $D_{\text{clv}}/A_0$, is shown in Fig. 5.7b. In the high temperature low stress calculations the value of $p$ is near zero until $t \approx 100$hrs, Fig. 5.7a. The increase in $\sigma$ in the high temperature low stress calculations, not only depends on $D_{\text{clv}}$ but also on $A_{\text{oxide}}$ and $D_{\text{void}}$. The probability of cleavage-like crack nucleation is smaller than in the low temperature high stress calculations because of the smaller applied nominal stress. As shown in Fig. 5.7b, the loss of area fraction due to cleavage-like cracking, $D_{\text{clv}}/A_0$, is slightly greater for thinner specimen than for thicker specimens.

Figure 5.8 shows the effect of specimen thickness on the creep strain to fracture, $\varepsilon_f$, and on the time to fracture, $t_f$, for the high temperature low stress creep loading condition. Both the model predictions and the experimental data from Ref. [10] and Chapter 2 are plotted. In the experimental data there is no systematic dependence of $\varepsilon_f$ on specimen

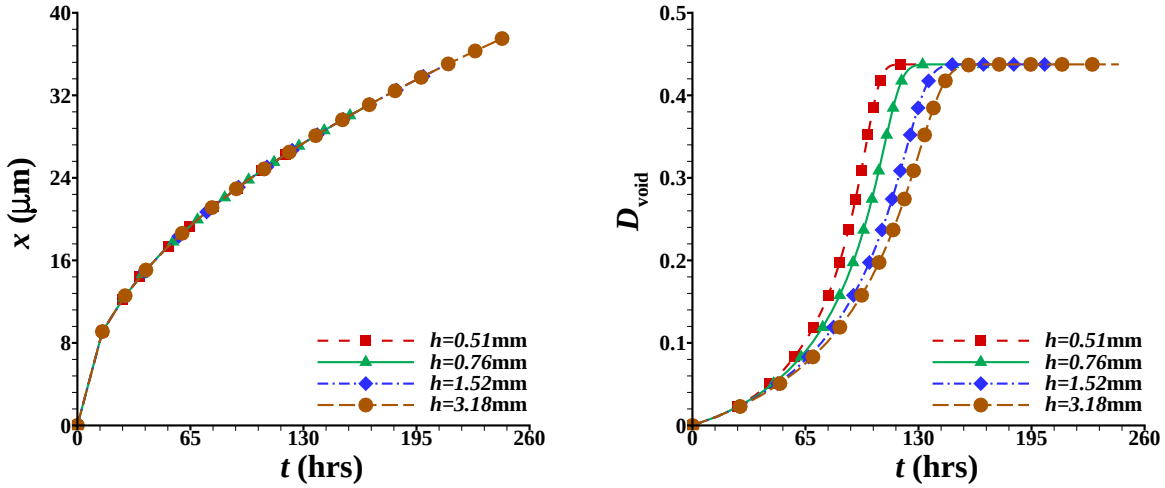


(a) (b)

FIGURE 5.6. Evolution of (a) oxide layer thickness $x$ and (b) cumulative loss of area fraction of the bulk cross section due to void nucleation ($D_{\text{void}}$) at high temperature low stress creep for various specimens with thickness $h$. The values are averaged over 50 calculations.

thickness $h$ whereas the calculations show some dependence of $\varepsilon_f$ on $h$. The time to fracture, $t_f$, shows a good correlation with the experimental data and follows the $1/\sqrt{h}$ dependence seen in the experimental results in Chapter 2. Compared with the low temperature high stress loading condition results in Fig. 5.4, there is a relative lack of scatter among the 50 computations for each specimen thickness $h$ in Fig. 5.8. This is a consequence of strain controlled void nucleation rather than cleavage-like cracking being the dominant damage mechanism in the bulk.

## 5.4. Discussion

With this simple model the relative contributions of surface damage and bulk damage can also be compared. Figure 5.9 shows a comparison of calculated and experimental curves of creep strain versus time for specimens with thicknesses $h = 0.76$mm and 3.18mm in the high temperature low stress creep loading condition. In Fig, 5.9a only surface damage is modeled, $\dot{D}_{\text{void}} = 0$ and $\dot{D}_{\text{clv}} = 0$ in Eq. (61). Surface damage alone does not lead to the

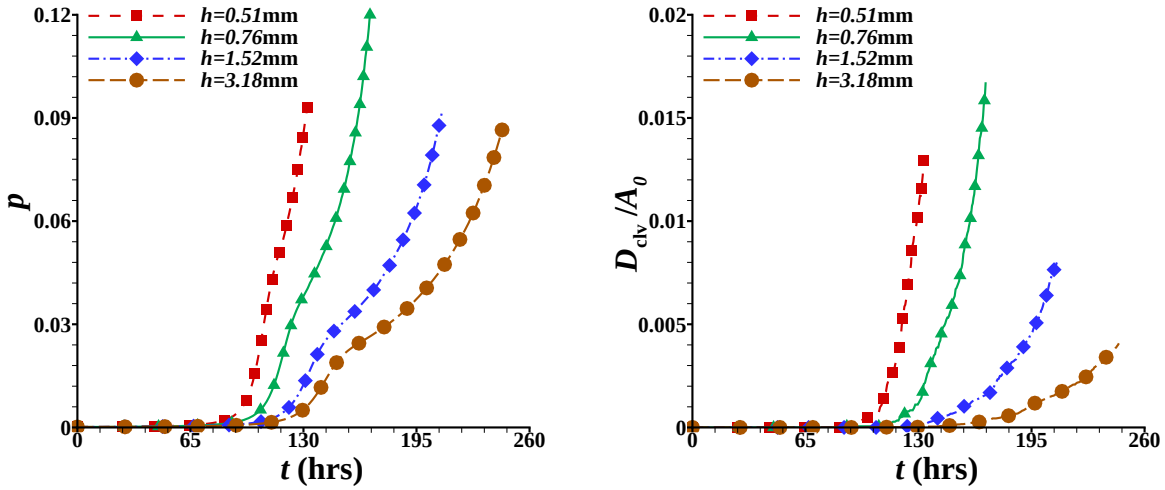


(a) (b)

FIGURE 5.7. Evolution of (a) Weibull cumulative distribution function ($p$) and (b) cumulative loss of area due to cleavage-like cracking normalized with the initial cross sectional area of the specimen ($D_{\text{clv}}/A_0$) at high temperature low stress creep calculations for various specimens with thickness $h$. The values are averaged over 50 calculations.

rapid increase in the creep strain seen experimentally. The calculated creep curves assuming no surface damage, $\dot{A}_{\text{oxide}} = 0$ in Eqs. (57) and (61), are compared with the experimental creep curves in Fig. 5.9b. The evolution of creep strain for the calculations with only bulk damage also do not show rapid increase seen in the experimental data. Hence, the model indicates that in the high temperature low stress loading condition both surface and bulk damage play significant roles. On the other hand, in the low temperature high stress loading condition bulk damage alone can give a rather good representation of the evolution of creep strain. The results here indicate that, much like Baldan [9] suggested, the loss of load carrying area due to bulk damage is a major contributor to the thickness debit effect.

Previous models of the thickness debit effect at a high temperature low stress loading condition focused on a surface damage mechanism [35, 36, 37]. Although surface damage alone can reproduce the thickness debit effect, the surface damage layer thickness that needs

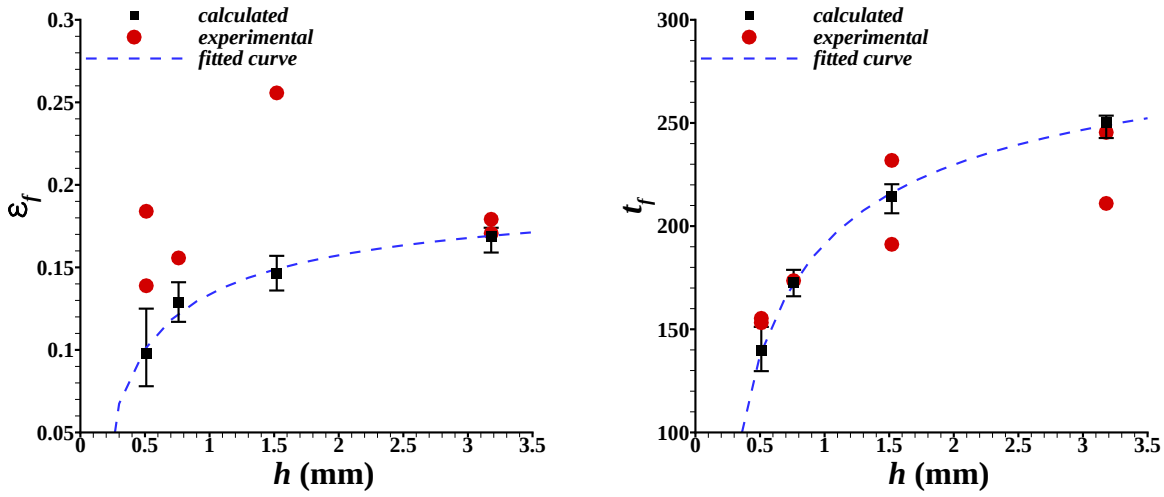


(a) (b)

FIGURE 5.8. The effect of specimen thickness ($h$) on (a) the creep strain to fracture ($\varepsilon_f$) and (b) the time to fracture ($t_f$, hrs) at high temperature low stress creep. Experimental data is taken from Ref. [10] and Chapter 2. The dashed line is a least-square fit of $a - b/\sqrt{h}$ to the mean value of calculated $\varepsilon_f$ and $t_f$ data, where $a$ and $b$ are positive fitting constants and their values differ for $\varepsilon_f$ and $t_f$. The error bars show the maximum and minimum deviation over the mean value of 50 calculations.

to be assumed is much greater than observed. For example, in Gullickson et al. [35], a good representation of the experimental creep curve for a specimen with $h = 0.38$mm was obtained with only surface damage with a surface layer thickness of 152$\mu$m which is more than three times the thickness, $x(1+\alpha^{\mathrm{L1}}+\alpha^{\mathrm{L2}})$, of the surface damage layer observed in the experiments reported in Chapter 2 or in the calculations, Fig. 5.6.

The simple phenomenological model presented here gives a quite good prediction of the evolution of creep strain with time for various specimen thicknesses at both the creep test conditions. However, the quantitative agreement of strain to failure and time to failure with experiment depends to some extent on the more or less arbitrary choice of the values of $D_{\mathrm{fail}}$ and $\dot{\varepsilon}_{\mathrm{fail}}$. In most of the calculations here, failure is associated with attaining $\dot{\varepsilon}_{\mathrm{fail}}$. Of

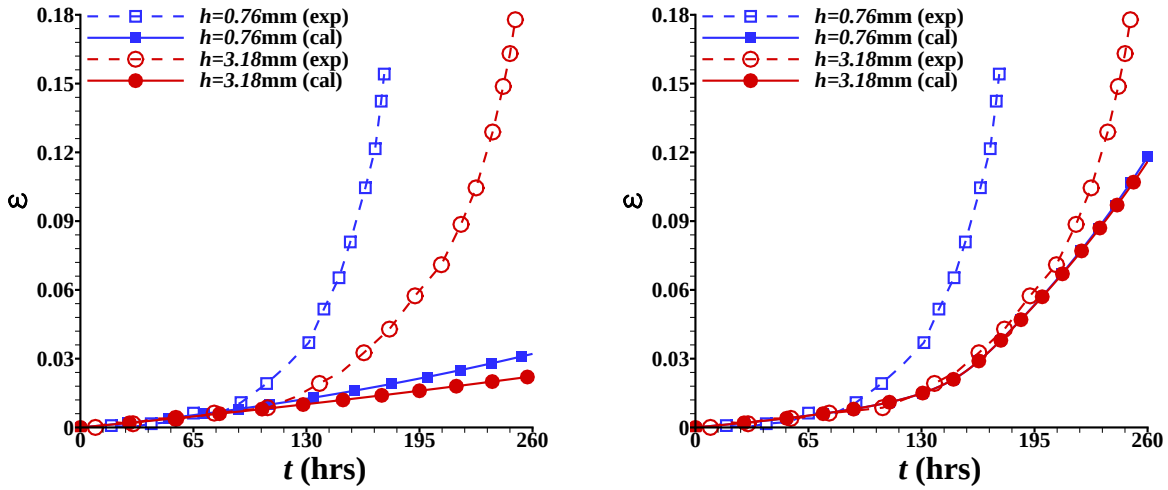


(a) (b)

FIGURE 5.9. Comparison of the calculated (cal) creep curves (a) considering only surface damage ($\dot{D}_{\text{void}} = \dot{D}_{\text{clv}} = 0$) and (b) considering only bulk damage mechanism ($\dot{A}_{\text{oxide}} = 0$) with the experimental (exp) creep curves from Ref. [10] of specimens with thickness $h = 3.18$mm and 0.76mm in the high temperature low stress loading condition.

course, physically attaining a certain strain rate does not imply loss of load carrying ability. The presumption in using such a criterion is that the strain rate increase is due to the loss of load carrying area and that a large strain rate corresponds to a high density of defects that will interact and coalesce; a process not accounted for in the simple model.

Both the experiments and the calculations exhibit a square root dependence on specimen thickness, Figs. 5.4 and 5.8. The fit for the calculations is even better than for the experimental data. Nevertheless, a mechanistic reason for the $1/\sqrt{h}$ dependence for both the strain to failure and the time to failure can not be found. Indeed, the $1/\sqrt{h}$ dependence fits the results for the two thicknesses, $h = 1.52$mm and $h = 3.18$mm, in the low temperature high stress loading condition where the failure is associated with a loss of area due to cracking as well as for all the remaining calculations under both loading conditions where failure is associated with the strain rate reaching $\dot{\varepsilon}_{\text{fail}}$.

In addition to the fit of the creep curve and creep failure data, the model predicts some features of the failure process that are in very good qualitative agreement with the experimental observations, such as the increased fraction of cleavage-like cracks on the failure surfaces of thinner specimens and the thickness of the surface damage layer in the high temperature low stress loading condition. The model also points out the important role played by void nucleation in the high temperature low stress loading condition. Indeed, calculations (not shown here) for the high-temperature low stress loading conditions with no cleavage-like crack formation give only a small change in the creep strain evolution from that in Fig. 5.7. On the other hand, calculations for this loading condition (also not shown here) that neglect void nucleation but account for cleavage-like cracking give the evolution of creep strain to be much like the results computed for surface damage only in Fig. 5.9a.

The failure mechanism that emerges from the model is a damage percolation process similar to that in Ref. [112] except that in the circumstances here the process is nucleation dominated. Depending on temperature and stress level, the main damage mechanism is either the nucleation of cleavage-like cracks or void nucleation. At the low value of stress triaxiality in uniaxial tension, void growth does not contribute, as shown in Chapters 3 and ch4. The surface damage at high temperature low stress in the experiments of Ref. [10] and of Chapter 2 plays a secondary role and exaggerates the bulk damage in thinner specimens. The loss of area associated with defect nucleation leads to increased stress and an increased strain rate on the remaining intact area which then leads to increased defect nucleation further reducing the load carrying area and so on. This mechanism eventually leads to a cascade of defect nucleation that is more detrimental for thinner specimens than for thicker specimens so giving rise to the thickness debit effect.

## 5.5. Summary and Conclusions

A simple phenomenological model to analyze the effect of specimen thickness on the uniaxial tensile creep response of Ni-based single crystal superalloys has been developed. The main features of the model draw on the experimental observations in Chapter 2 and the finite element calculations of void evolution in Chapters 3 and 4. However, the model does contain

failure parameters that were chosen to fit experimental data. Although the quantitative fit to the experimental data does depend on the specific value of these parameters, key qualitative features do not.

- In the low temperature high stress loading condition the main contribution to the thickness debit effect comes from bulk damage due to the nucleation of cleavage-like cracks from the surface of pre-existing voids.
- In the high temperature low stress loading condition bulk damage, mainly void nucleation, and surface damage due to oxidation contribute to the thickness debit effect.
- A thickness debit effect, in good quantitative agreement with the experimental data in Ref. [10] and Chapter 2, is obtained under both the low temperature high stress loading condition and the high temperature low stress loading condition.
- The model also predicts several features of the failure process in very good qualitative agreement with the experimental observations such as the $a - b/\sqrt{h}$ fit to failure times and strains, and the increased area fraction of cleavage for thinner specimens.
- Parameter studies indicate that void nucleation plays a major role in creep failure in the high temperature low stress loading condition.

# CHAPTER 6

# CORRELATING TOUGHNESS AND ROUGHNESS IN DUCTILE FRACTURE

## 6.1. Introduction

Thirty years ago, Mandelbrot and coworkers revealed the self-affine nature of fracture surfaces [113]. Their hope was to relate the roughness of fracture surfaces via the exponents characterizing their scale invariance properties to the material's crack growth resistance. This hope has remained unfulfilled. Indeed, later studies showed that the value of the roughness exponent was not only independent of the material toughness but also of the material considered, as long as the failure mechanism remained the same [114, 115]. Indeed, the scaling exponent measured along the propagation direction was observed to take a value $\beta^{\text{brittle}} \simeq 0.5$ rather independent of the considered material for brittle failure while another value around $\beta^{\text{damage}} \simeq 0.6$ was observed for damage accompanying failure [116, 117].

The universality of fracture surface roughness exponents limits the applicability of quantitative fractography based on statistical analyses for the characterization of microscopic failure mechanisms and toughness. On the other hand, it has paved the way for a unified theoretical framework based on critical transition theory to describe the failure properties of disordered materials. By interpreting the onset of material failure as a dynamic phase transition, many aspects of the behavior of cracks in disordered materials has thus been rationalized, such as the intermittent dynamics of cracks [118], their scale invariant roughness [119], their average dynamics [120] and their effective toughness [121]. Most of these successes have been achieved in the context of brittle failure, but our understanding of the scaling properties of ductile fracture surfaces is still limited.

The process that governs the ductile fracture of structural materials at room temperature is one of nucleation, growth and coalescence of micron scale voids, and involves large plastic deformations. Quantitative models of crack growth by the progressive coalescence of voids with a crack have been available since the 1970s [122, 123, 124, 125], and calculations have provided reasonable agreement with experimental toughness measurements [126]. How-

ever, only recently has the capability been developed to calculate sufficient amounts of three dimensional ductile crack growth in heterogeneous microstructures to obtain a statistical characterization of the predicted fracture surfaces [127, 128]. This enables us to explore the microscopic mechanisms governing the fracture surface roughness as well as the relation, if any, to a material's crack growth resistance.

The present work capitalizes on these new developments and show that the scaling properties of ductile cracks can correlate with the material's toughness. However, the relation is not with the value of the roughness exponent, but with the cut-off length of the scale invariant regime. In particular, it is shown that the cut-off length scale of the self-affine behavior of ductile cracks can be quantitatively related to a measure of fracture toughness. This correlation is shown for ductile crack growth with a range of densities of randomly distributed void nucleation sites and with fixed material properties.

Quite generally, length scales extracted from scale invariant properties of disordered systems such as power law amplitudes or boundaries of the scale invariant domain are not universal and depend on the detailed characteristics of the system. In the context of the failure of heterogeneous materials, the microstructure of the material and the failure mechanism play this role. Varying the microstructure in a controlled manner is the key to identifying the quantities that determine the roughness associated length scales. Experimentally, it is difficult if not impossible to change one microstructural parameter without affecting others. However, numerical simulations permit this. Here one parameter, the density of randomly distributed large particles is varied, to analyze a family of ductile materials with a broad range of toughness. The results reveal a length scale extracted from the statistics of the crack roughness that is linked to a measure of the macroscopic toughness, hence correlating roughness and toughness in ductile fracture.

## 6.2. Problem Formulation and Numerical Method

The full three dimensional analyses of ductile fracture are carried out using a data parallel implementation of the progressively cavitating ductile material model in a transient finite element program. The boundary value problem analyzed here is the same as in Needle-

man et al. [127] (also see [129]). For completeness, the formulation and constitutive relation are briefly stated here.

A convected coordinate Lagrangian formulation is used with transient calculations carried out for numerical convenience. The finite element calculations are based on the dynamic principle of virtual work written as

$$\int_V \tau^{ij}\delta E_{ij}dV = \int_S T^i \delta u_i dS - \int_V \rho\frac{\partial^2 u^i}{\partial t^2}\delta u_i dV \tag{67}$$

with

$$T^i = \left(\tau^{ij} + \tau^{kj}u^i_{,k}\right)v_j \tag{68}$$

$$E_{ij} = \frac{1}{2}\left(u_{i,j} + u_{j,i} + u^k_{,i}u_{k,j}\right) \tag{69}$$

where $\tau^{ij}$ are the contravariant components of the Kirchhoff stress on the deformed convected coordinate net ($\tau^{ij} = J\sigma^{ij}$, with $\sigma^{ij}$ being the contravariant components of the Cauchy stress and $J$ being the ratio of the current to reference volume), $v_j$ and $u_j$ are the covariant components of the reference surface normal and displacement vectors, respectively, $\rho$ is the mass density, $V$ and $S$ are the volume and surface of the body in the reference configuration, and $()_{,i}$ denotes covariant differentiation in the reference $(y^1, y^2, y^3)$ Cartesian frame. All field quantities are taken to be functions of the convected coordinates, $y^i$, and time, $t$. In presenting the results the notations, $x$, $y$ and $z$ for $y^1$, $y^2$ and $y^3$, respectively are used.

A mode I small scale yielding boundary value problem is analyzed with symmetry conditions corresponding to an overall plane strain constraint. The analyses are carried out for a slice of material orthogonal to the initial crack plane (the $y^1 - y^3$-plane), with the in-plane dimensions $h_x \times h_y$ and the slice occupying $0 \leq y^3 \leq h_z$, Fig. 6.1. The initial crack front lies along $(0, 0, y^3)$ and the boundary conditions imposed are

$$u_3(y^1, y^2, 0) = 0 \ , \ u_3(y^1, y^2, h_z) = 0 \tag{70}$$

together with

$$T^1\left(y^1, y^2, 0\right) = T^2\left(y^1, y^2, 0\right) = 0$$

$$T^1\left(y^1, y^2, h_z\right) = T^2\left(y^1, y^2, h_z\right) = 0 \tag{71}$$

In the $y^1 - y^2$-plane remote displacement boundary conditions that correspond to the quasi-static linear isotropic elastic mode I crack tip field are prescribed. The crack has an initial opening $b_0$ with traction free crack faces.

Although dynamic analyses are carried out, the focus is on quasi-static crack growth. In essence, the formulation can be regarded as dynamic relaxation to approach a quasi-static solution. The initial conditions and the time dependence of the loading are prescribed in order to minimize inertia effect (see [129] for further details on the prescription of the loading). As in [127], the in-plane block (see Fig. 6.1) dimensions are $h_x = h_y = 0.4$m with an initial crack tip with an opening of $b_0 = 1.875 \times 10^{-4}$m. The finite element mesh consists of 428,256 twenty node brick elements giving 1,868,230 nodes and 5,604,690 degree of freedom. Ten uniformly spaced elements are used through the thickness $h_z$ of 0.005m, with 10 elements through the thickness, and a uniform $208 \times 64$ in-plane ($x - y$ plane) mesh is used in a 0.02m $\times$ 0.006m region immediately in front of the initial crack tip with in-plane elements of dimension $e_x \approx e_y \approx 1.0 \times 10^{-4}$m. The element dimension, $e_x$, also serves as a normalization length. The results of the calculations are interpreted as modeling the quasi-static response so that, the absolute magnitude of geometric dimensions or units do not matter; what matters is the ratio of geometric lengths.

The constitutive framework is the modified Gurson constitutive relation (for more details see [93]) with the rate of deformation tensor written as the sum of an elastic part, $\mathbf{d}^e = \mathbf{L}^{-1} : \hat{\boldsymbol{\sigma}}$, a viscoplastic part, $\mathbf{d}^p$, and a part due to thermal straining, $\mathbf{d}^\Theta = \alpha\dot{\Theta}\mathbf{I}$, so that

$$\mathbf{d} = \mathbf{L}^{-1} : \hat{\boldsymbol{\sigma}} + \alpha\dot{\Theta}\mathbf{I} + \mathbf{d}^p \tag{72}$$

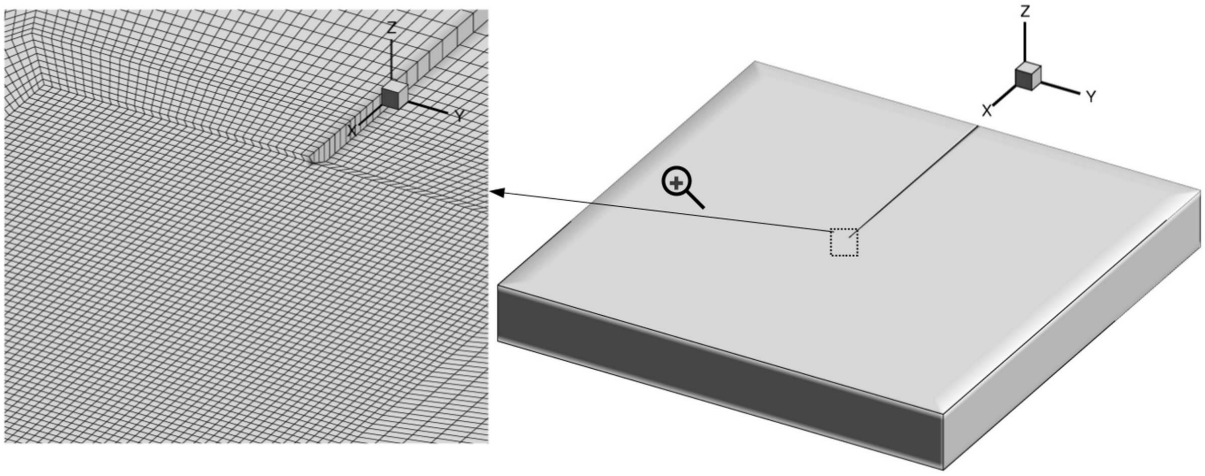


FIGURE 6.1. Full three dimensional specimen with an initial crack and the finite element mesh in the vicinity of the initial crack tip. Here and in subsequent figures, x, y and z denote the coordinates $y^1$, $y^2$ and $y^3$, respectively.

Here, small elastic strains are assumed, $\hat{\boldsymbol{\sigma}}$ is the Jaumann rate of Cauchy stress, $\Theta$ is the temperature, $\alpha = 1 \times 10^{-5}/\mathrm{K}$ is the thermal expansion coefficient and $\mathbf{L}$ is the tensor of isotropic elastic moduli.

The plastic part of the strain rate, $\mathbf{d}^p$, is given by [130]

$$\mathbf{d}^p = \left[\frac{(1-f)\bar{\sigma}\dot{\bar{\epsilon}}}{\boldsymbol{\sigma} : \frac{\partial \phi}{\partial \boldsymbol{\sigma}}}\right] \frac{\partial \phi}{\partial \boldsymbol{\sigma}} \tag{73}$$

with the flow potential having the form [131]

$$\Phi = \frac{\sigma_e^2}{\bar{\sigma}^2} + 2q_1 f^* \cosh\left(\frac{3q_2\sigma_h}{2\bar{\sigma}}\right) - 1 - (q_1 f^*)^2 = 0 \tag{74}$$

where $q_1 = 1.25$, $q_2 = 1.0$ are parameters introduced in [132, 133], $f$ is the void volume fraction, $\bar{\sigma}$ is the matrix flow strength, and

$${\sigma_e}^2 = \frac{3}{2}\boldsymbol{\sigma}' : \boldsymbol{\sigma}' \quad , \quad \sigma_h = \frac{1}{3}\boldsymbol{\sigma} : \mathbf{I} \quad , \quad \boldsymbol{\sigma}' = \boldsymbol{\sigma} - \sigma_h \mathbf{I} \tag{75}$$

The function $f^*$, introduced in [134], is given by

$$f^* = \begin{cases} f, & f < f_c \\ f_c + (1/q_1 - f_c)(f - f_c)/(f_f - f_c), & f \geq f_c \end{cases} \tag{76}$$

where the values $f_c = 0.12$ and $f_f = 0.25$ are used.

The matrix plastic strain rate, $\dot{\bar{\epsilon}}$, is given by

$$\dot{\bar{\epsilon}} = \dot{\epsilon}_0 \left[ \frac{\bar{\sigma}}{g(\bar{\epsilon}, \Theta)} \right]^{1/m} \quad , \quad g(\bar{\epsilon}, \Theta) = \sigma_0 G(\Theta) \left[ 1 + \bar{\epsilon}/\epsilon_0 \right]^N \tag{77}$$

with $\bar{\epsilon} = \int \dot{\bar{\epsilon}} dt$ and $\epsilon_0 = \sigma_0/E$. In the calculations here $E = 70$GPa, $\nu = 0.3$, $\sigma_0 = 300$MPa ($\epsilon_0 = \sigma_0/E = 0.00429$), $N = 0.1$, $m = 0.01$ and $\dot{\epsilon}_0 = 10^3 \text{s}^{-1}$.

Adiabatic conditions are assumed so that

$$\rho c_p \frac{\partial \Theta}{\partial t} = \chi \boldsymbol{\tau} : \mathbf{d}^p \tag{78}$$

with $\rho = 7600\text{kg/m}^3 = 7.6 \times 10^{-3}\text{MPa/(m/s)}^2$, $c_p = 465\text{J/(kg }^\circ\text{K)}$, $\chi = 0.9$, and the temperature-dependence of the flow strength is given by

$$G(\Theta) = 1 + b_G \exp(-c[\Theta_0 - 273]) \left[ \exp(-c[\Theta - \Theta_0]) - 1 \right] \tag{79}$$

with $b_G = 0.1406$ and $c = 0.00793/\text{K}$. In Eq. (79), $\Theta$ and $\Theta_0$ are in K and $\Theta_0 = 293$K. Also, the initial temperature is taken to be uniform and 293K.

The initial void volume fraction is taken to be zero and the evolution of the void volume fraction is governed by

$$\dot{f} = (1 - f)\mathbf{d}^p : \mathbf{I} + \dot{f}_{nucl} \tag{80}$$

where the first term on the right hand side of Eq. (80) accounts for void growth and the second term accounts for void nucleation.

Eight point Gaussian integration is used in each twenty-node element for integrating the internal force contributions and twenty-seven point Gaussian integration is used for the

element mass matrix. Lumped masses are used so that the mass matrix is diagonal. The discretized equations are integrated using the explicit Newmark $\beta$-method ($\beta = 0$) [135]. The constitutive updating is based on the rate tangent modulus method in [136], while material failure is implemented via the element vanish technique in [137]. Just before final failure, when the void volume fraction $f$ in an integration point reaches $0.9f_f$, the value of $f$ is kept fixed so that the material deforms with a very small flow stress, and the entire element is taken to vanish when three of the eight integration points have reached this stage.

6.3. Inclusion Distributions

In the calculations the material microstructure is characterized by two populations of void nucleating second phase particles: (i) uniformly distributed small particles that are modeled by plastic strain controlled void nucleation; and (ii) large, low strength inclusions that are modeled as "islands" of stress controlled nucleation. In each case, void nucleation is assumed to be described by a normal distribution [108].

For plastic strain nucleation

$$\dot{f}_{nucl} = D\dot{\bar{\epsilon}} \ , \ D = \frac{f_N}{s_N\sqrt{2\pi}} exp\left[-\frac{1}{2}\left(\frac{\bar{\epsilon} - \epsilon_N}{s_N}\right)^2\right] \tag{81}$$

with $f_N = 0.04$, $\epsilon_N = 0.3$ and $s_N = 0.1$.

For stress controlled nucleation

$$\dot{f}_{nucl} = A\left[\dot{\bar{\sigma}} + \dot{\sigma}_h\right] \ , \ A = \frac{f_N}{s_N\sqrt{2\pi}} \exp\left[-\frac{1}{2}\left(\frac{\bar{\sigma} + \sigma_h - \sigma_N}{s_N}\right)^2\right] \tag{82}$$

The large, low strength inclusions will simply be referred to as inclusions now onwards in this manuscript. The value of $f_N$ in Eq. 82 at a point $(x, y, z)$ for an inclusion centered at $(x_0, y_0, z_0)$ is

$$f_N = \begin{cases} \bar{f}_N & \text{for } \sqrt{(x-x_0)^2 + (y-y_0)^2 + (z-z_0)^2} \leq r_0 \\ \\ 0 & \text{for } \sqrt{(x-x_0)^2 + (y-y_0)^2 + (z-z_0)^2} > r_0 \end{cases} \tag{83}$$

The values of $\bar{f}_N = 0.04$, $\sigma_N/\sigma_0 = 1.5$ and $s_N/\sigma_0 = 0.2$ are used in the calculations. The size and spacing of the inclusions introduce characteristic lengths into the formulation. The inclusion radius $r_0 = 1.5 \times 10^{-4}$m or in terms of in-plane element dimension $r_0 = 1.5e_x$ is kept fixed and the number of inclusions, $N_{incl}$, in the uniform mesh region in front of the initial crack tip is varied. As stated before the size of uniform mesh region in front of the initial crack tip is $V = 0.02\text{m} \times 0.006\text{m} \times 0.005\text{m}$. Varying the number of inclusions in the uniform mesh region of volume, $V$, varies both inclusion volume fraction, $n$, and mean (center to center) inclusion spacing, $l_0$. The inclusion volume fraction, $n = \left(N_{incl} \times \frac{4}{3}\pi r_0^3\right)/V$, and the mean inclusion spacing, $l_0 = (V/N_{incl})^{1/3}$. The calculations are carried out for eight inclusion volume fractions varying from $n = 0.012$ to $n = 0.19$ corresponding to mean inclusion spacings (in terms of in-plane element dimension) $l_0 = 10.6e_x$ and $l_0 = 4.21e_x$, respectively. The location of the inclusion centers within the uniform mesh region in front of the initial crack tip is determined using a random number generator with the condition that the center to center distance of two neighboring inclusions are at least greater than twice the inclusion radius. The parallel implementation of the formulation given in Section 6.2 in a transient finite element program permits us to perform large number of parametric studies in a reasonable amount of time. For each inclusion volume fraction seven random distributions of inclusion centers are considered. For the distribution with smallest inclusion volume fraction, $n = 0.012$, the results are based on five distributions because for two distributions, no inclusions were sufficiently close to the initial crack tip for void nucleation to occur under small scale yielding conditions. Figure 6.2a and 6.2b show the distribution of the inclusions on the plane $z = h_z$ for inclusion volume fractions, $n = 0.024$ ($l_0/e_x = 8.41$) and $n = 0.143$ ($l_0/e_x = 4.63$), respectively for one random distribution.

## 6.4. Numerical Results

### 6.4.1. Crack Initiation, Growth and Toughness

The attention here is focused on quasi-static crack growth under remote mode I small scale yielding boundary condition. The contours of constant equivalent plastic strain , $\bar{\epsilon}^p$, shown in Fig. 6.3 very closely resemble the shape of the contours as expected for small scale

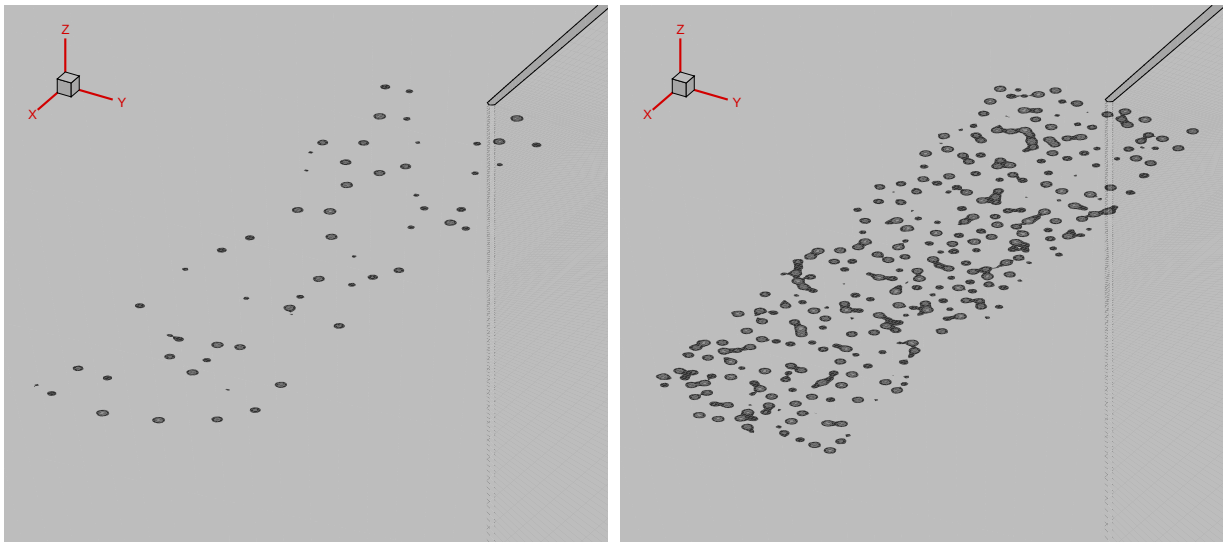


(a) (b)

FIGURE 6.2. Initial inclusion distribution for inclusion volume fractions, (a) $n = 0.024$ $(l_0/e_x = 8.41)$ and (b) $n = 0.143$ $(l_0/e_x = 4.63)$ for one random distribution.

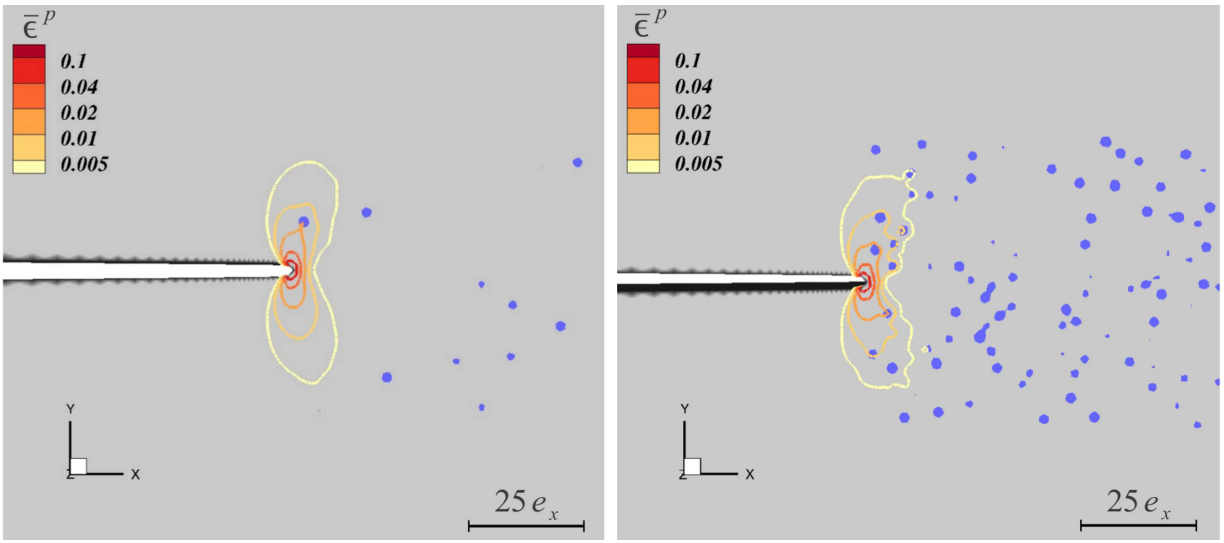


(a) (b)

FIGURE 6.3. Contours of constant equivalent plastic strain, $\bar{\epsilon}^p$, for inclusion volume fractions, (a) $n = 0.024$ $(l_0/e_x = 8.41)$ and (b) $n = 0.143$ $(l_0/e_x = 4.63)$ for one random distribution at $J/(\sigma_0 e_x) = 1.61$.

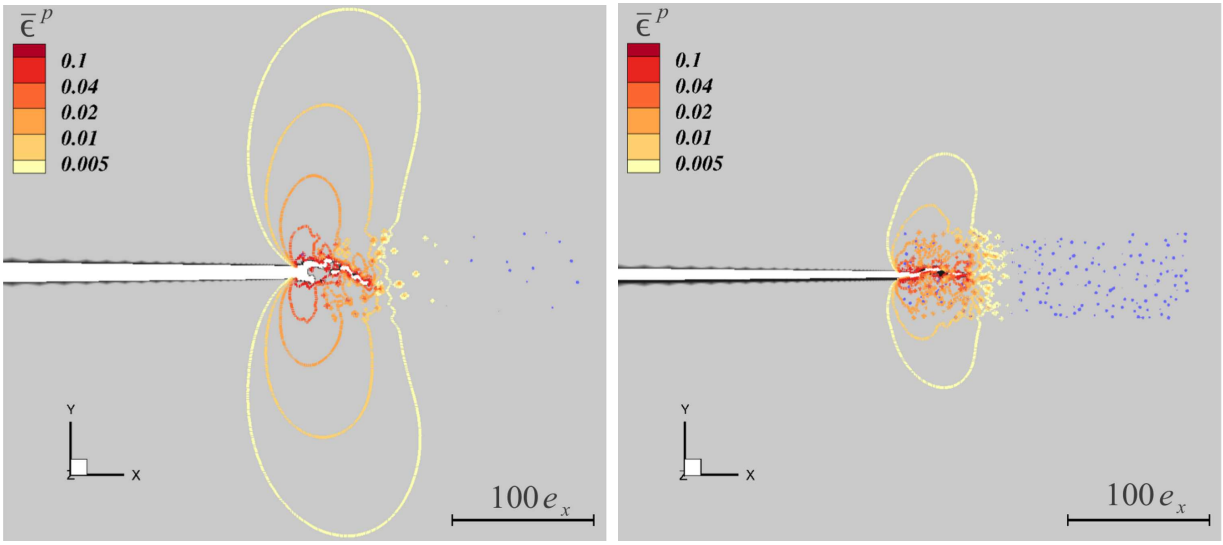


(a) (b)

FIGURE 6.4. Contours of constant equivalent plastic strain, $\bar{\epsilon}^p$, for inclusion volume fractions, (a) $n = 0.024$ ($l_0/e_x = 8.41$) and (b) $n = 0.143$ ($l_0/e_x = 4.63$) for one random distribution after a crack growth of $\Delta a = 50e_x$.

quasi-static yielding condition. The contours of $\bar{\epsilon}^p$ are plotted for applied normalized $J$, $J/(\sigma_0 e_x) = 1.61$, for inclusion volume fractions $n = 0.024$ and $n = 0.143$. Where $\sigma_0$ is the initial yield strength and $e_x$ is the representative dimension of mesh size. The value of $J$ is computed from the applied stress intensity factor $K_I$ using the small scale yielding relation, $J = K_I^2 (1 - \nu^2)/E$ [138]. At this point no crack initiation has occurred for both the cases shown in Fig. 6.3. The initiation of crack growth is assumed when elements at the initial crack tip achieve a void volume fraction, $f \geq 0.1$, throughout the thickness (along $z$-axis). At the same applied $J$ the half height of the area enclosed by the same value of $\bar{\epsilon}^p$ is roughly the same for both inclusion volume fractions as evident in Fig. 6.3. Local perturbation in the strain field due to the presence of inclusions can be seen even at a very small value of $\bar{\epsilon}^p$ as early nucleation of voids occur following a stress based criteria.

Similar contours of $\bar{\epsilon}^p$ for the same inclusion volume fractions but after a crack growth of $\Delta a = 50e_x$ are shown in Fig. 6.4a for $n = 0.024$ and in Fig. 6.4b for $n = 0.143$. The crack length $\Delta a$ is defined as the projected length of the $f = 0.1$ void volume fraction contour

on the initial crack mid plane averaged along the specimen thickness. At $\Delta a = 50e_x$, the value of $J/(\sigma_0 e_x) = 16.15$ for $n = 0.024$ and $J/(\sigma_0 e_x) = 7.6$ for $n = 0.143$. Figures 6.4a and 6.4b illustrate the change in strain pattern due to crack growth off the initial crack line. Compared to the shape of the $\bar{\epsilon}^p$ contours shown in Fig. 6.3 here the shape of the $\bar{\epsilon}^p$ contour is noticeably perturbed by the advancing crack, which is even more pronounced in Fig. 6.4b for $n = 0.143$.

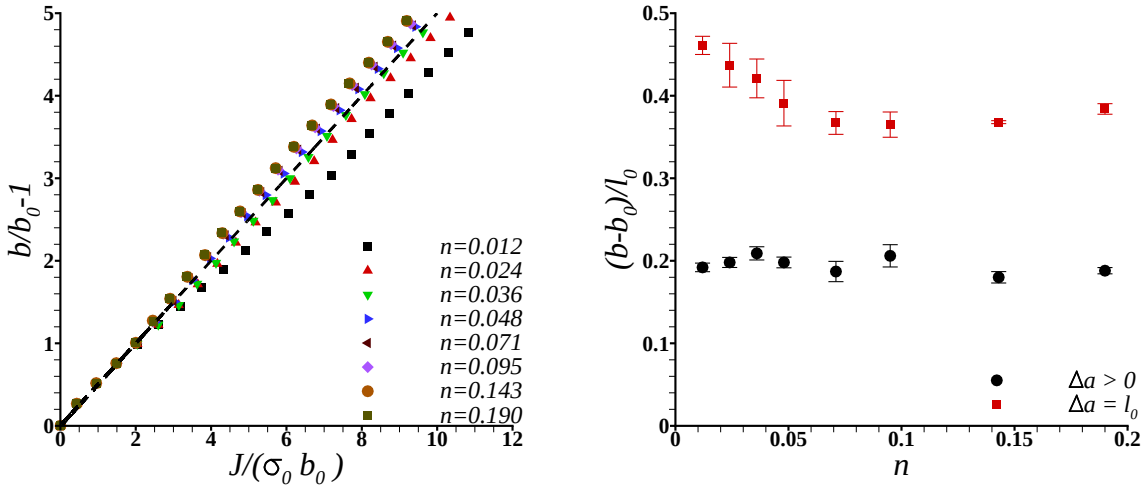


(a) (b)

FIGURE 6.5. (a) Curves of crack opening displacement normalized with initial crack opening, $b/b_0 - 1$, versus normalized applied $J$, $J/(\sigma_0 b_0)$, for one random distribution of all eight values of $n$. (b) Effect of inclusion volume fraction, $n$, on the crack opening displacement normalized with mean inclusion spacing, $(b - b_0)/l_0$.

Curves of crack opening displacement normalized with initial crack opening, $b/b_0 - 1$, versus normalized applied $J$, $J/(\sigma_0 b_0)$ for one random distributions of all eight inclusion volume fractions, $n$, considered here are shown in Fig. 6.5a, where $b$ is the current crack opening at $x = -2.82e_x$ (initial crack tip is at $x = 0$). For small scale yielding under quasi-static loading conditions the slope of curves should be 1/2. The dashed line in Fig. 6.5a is $b/b_0 - 1 = 0.5\,(J/(\sigma_0 b_0))$ and correlates very well with the computed values of $b$ and $J$ prior

to the onset of crack growth. This again confirms that the quasi-static loading conditions are reasonably well approximated. The variation of crack opening displacement normalized with mean inclusion spacing, $(b - b_0)/l_0$, with $n$ at the crack initiation where $\Delta a$ is slightly greater than zero and after a crack growth of $\Delta a = l_0$ is shown in Fig. 6.5b. The error bar in Fig. 6.5 is the standard error over seven random distributions for each $n$. The value of $b$ at crack initiation is mostly dependent on the distance of inclusions from the crack tip which can be roughly correlated to the mean inclusion spacing and hence the value of $(b - b_0)/l_0$ at initiation is roughly constant. Whereas the value of $(b - b_0)/l_0$ at $\Delta a = l_0$ roughly corresponds to the coalescence of the crack tip with the inclusions ahead. This indeed will depend on the overall distribution of the inclusions ahead of the crack tip as can be seen in Fig. 6.5b where the value of $(b - b_0)/l_0$ at $\Delta a = l_0$ is decreasing with increasing $n$ until $n \leq 0.071$ and later saturates.

Figure 6.6 shows the evolution of contour of void volume fraction $f = 0.1$ for one random distribution corresponding to $n = 0.024$ at various applied $J$. The void volume fraction in the area enclosed by the contour line corresponding to $f = 0.1$ is greater than 0.1. Although $f = 0.1$ has no special significance in the constitutive relation but it does give a more representative picture of the current crack tip and as stated earlier the extent of $f = 0.1$ contour is used to define the projected crack length. Similar procedure was adopted in [139, 126]. As shown in Fig. 6.6a, the crack is growing at an angle from the initial crack plane. For $n = 0.024$ ($l_0/e_x = 8.41$) the inclusions are far away from the initial crack tip and hence the initial crack growth is solely due to large plastic strain based void nucleation. In Fig. 6.6b nucleation of voids at the inclusions ahead of the main crack tip can be seen. These voids coalesce to form a micro-crack. The main crack then coalesces with theses voids/micro-cracks and subsequently zig-zag back to the initial crack plane, Figs. 6.6c and 6.6d. However in some cases micro-cracks unconnected to the main crack are left behind as the crack advances, Fig. 6.6d.

The evolution of contour of void volume fraction $f = 0.1$ for one random distribution corresponding to $n = 0.143$ is shown in Fig. 6.7. For $n = 0.143$, Fig. 6.7a, the crack starts

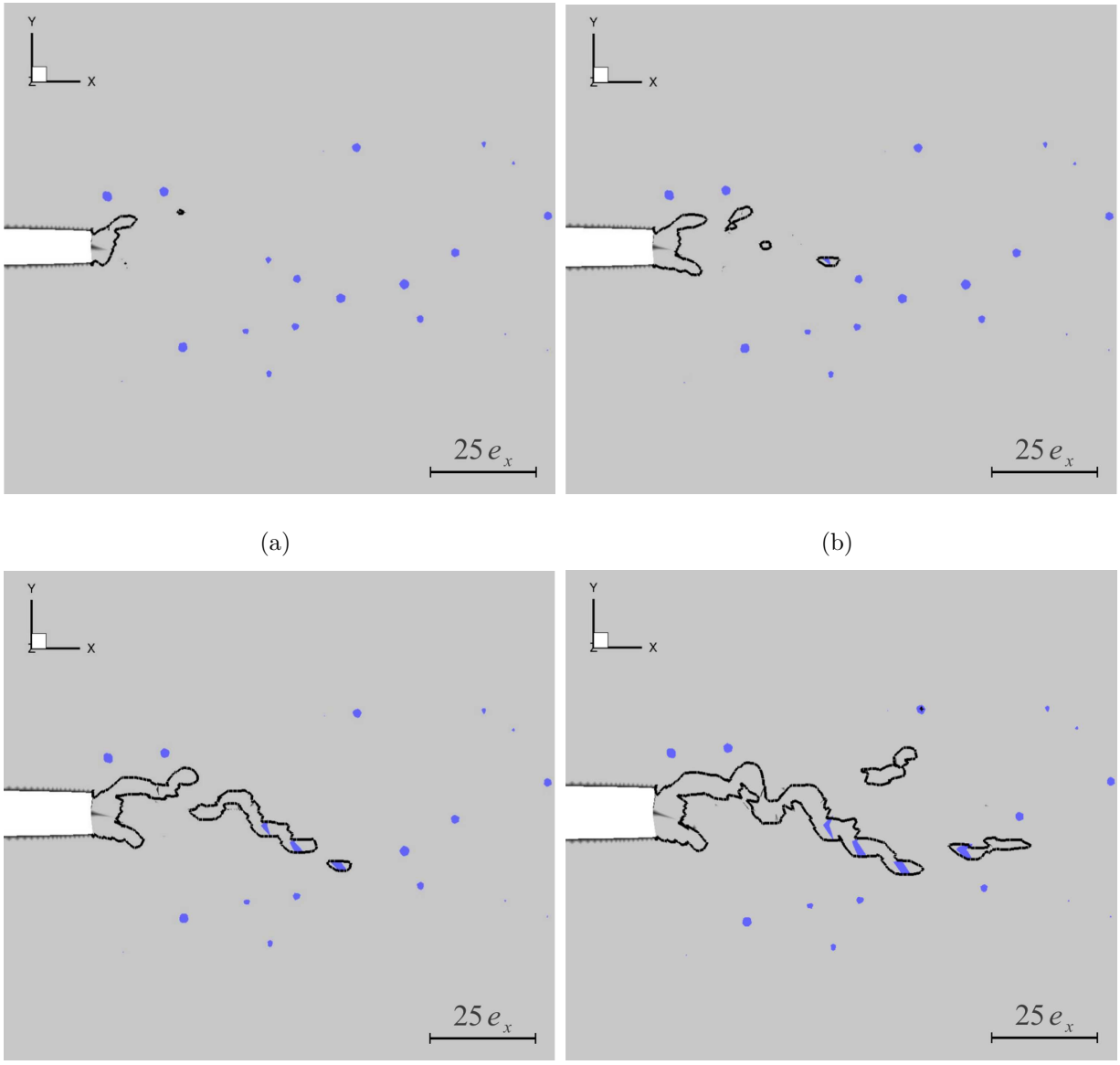


FIGURE 6.6. Evolution of contour of void volume fraction, $f = 0.1$, for, $n = 0.024$ ($l_0/e_x = 8.41$), at various applied $J$, (a) $J/(\sigma_0 e_x) = 12.63$, (b) $J/(\sigma_0 e_x) = 14.5$, (c) $J/(\sigma_0 e_x) = 17.9$ and (d) $J/(\sigma_0 e_x) = 21.65$.

growing along the initial crack plane due to the abundance of inclusions ahead of the crack tip. In Fig. 6.7b, the long micro-crack nucleating ahead of the main crack, which is now stationary, is slightly above the initial crack plane but indeed aligned along the initial crack plane. As shown in Figs. 6.7c and 6.7d, the crack roughly keeps growing along the initial

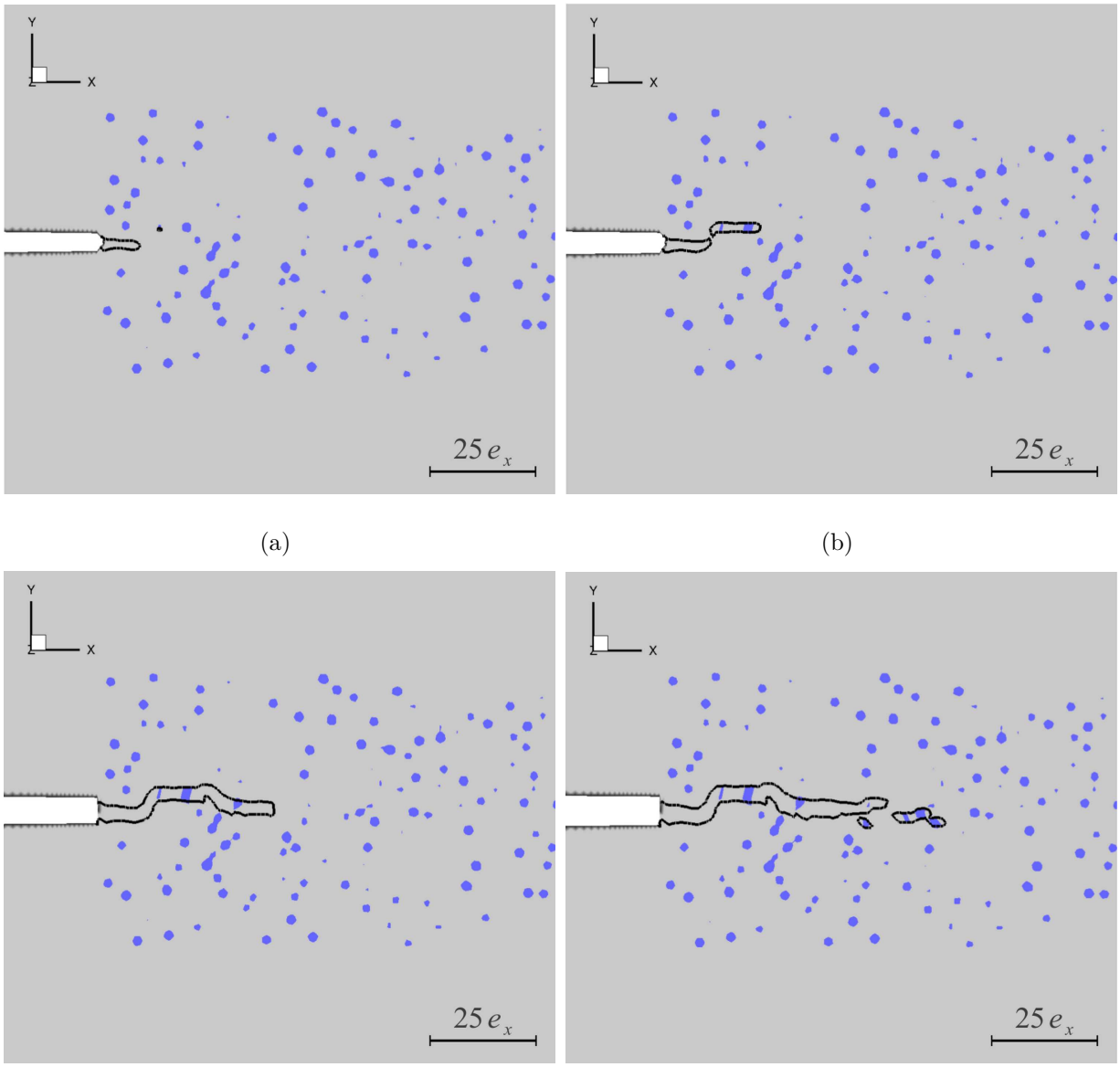


FIGURE 6.7. Evolution of contour of void volume fraction, $f = 0.1$, for inclusion volume fraction $n = 0.143$ ($l_0/e_x = 4.63$), at various applied $J$, (a) $J/(\sigma_0 e_x) = 4.5$, (b) $J/(\sigma_0 e_x) = 5.4$, (c) $J/(\sigma_0 e_x) = 7.56$ and (d) $J/(\sigma_0 e_x) = 8.8$.

crack plane. For large inclusion volume fractions, long micro-cracks aligned with the initial crack plane nucleate and the main crack grows by linking up with these micro-cracks.

The crack growth resistance curves or the J-R curves for seven random distributions of

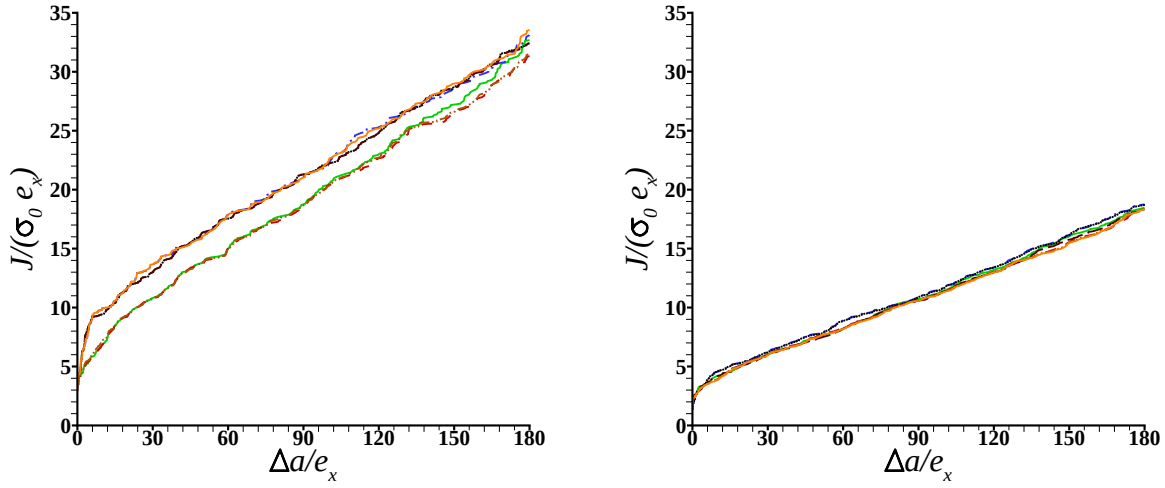


FIGURE 6.8. Applied normalized $J$, $J/(\sigma_0 e_x)$, versus normalized crack extension, $\Delta a/e_x$, for seven random distributions of inclusion volume fractions, (a) $n = 0.024$ ($l_0/e_x = 8.41$) and (b) $n = 0.143$ ($l_0/e_x = 4.63$).

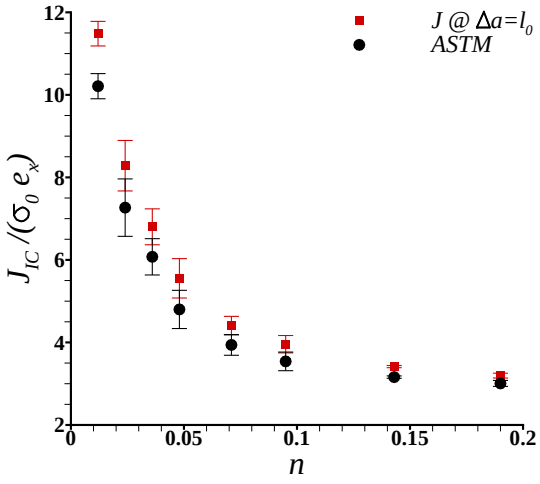


FIGURE 6.9. Effect of inclusion volume fraction, $n$, on the fracture toughness, $J_{IC}/(\sigma_0 e_x)$.

inclusions for inclusion volume fractions $n = 0.024$ and $n = 0.143$ are shown in Fig. 6.8. The value of $J$ is normalized by $\sigma_0 e_x$ and the crack length $\Delta a$ is normalized by $e_x$. The variation in the J-R curves for seven random distributions of inclusions for $n = 0.024$, Fig. 6.8a, mainly

stem from the nucleation event. For $n = 0.143$, Fig. 6.8b, the variation in the J-R curves for seven random distributions of inclusions is roughly insignificant due to the ease of crack nucleation. The slope of $J$ versus $\Delta a$ curve in the stable crack growth regime is significantly greater for $n = 0.024$ than $n = 0.143$.

The calculations here proceed until sufficient crack growth is observed hence the plane strain mode I fracture toughness $J_{IC}$, following the procedure recommended by ASTM [140] can be estimated. The single valued $J_{IC}$ determined by the method outlined in ASTM [140] standard marks the beginning stage of the material crack growth resistance. The variation of normalized $J_{IC}$ with inclusion volume fraction $n$ is shown in Fig. 6.9. Also shown is the value of $J$ at $\Delta a = l_0$ in Figs. 6.9. The crack length $\Delta a = l_0$ roughly corresponds to the coalescence of the crack tip with the inclusions ahead. The error bars in Fig. 6.9 show the standard errors for realizations of inclusion distributions having the same $n$. The value of $J_{IC}$ decreases rapidly with increasing $n$ until $n \leq 0.071$ and for greater values of $n$, $J_{IC}$ tends towards saturation. The similar behavior is shown by the value of $J$ at $\Delta a = l_0$. The value of $J$ at $\Delta a = l_0$ is slightly greater than the $J_IC$ value estimated using ASTM [140] standard for low inclusion volume fractions. The difference between ASTM $J_{IC}$ and $J$ at $\Delta a = l_0$ decreases with increasing value of $n$.

### 6.4.2. Statistical Analysis of Fracture Surfaces

As stated earlier the crack is defined as the region enclosed by the contour of $f = 0.1$. The value of $f \geq 0.1$ in the region enclosed by the contour of $f = 0.1$ and outside the contour of $f = 0.1$ the value of $f \leq 0.1$ as shown in Fig. 6.10. The boundary of these two regions define the fracture line for a given plane along the thickness of the specimen hence for each plane there are two fracture lines, top and bottom, Fig. 6.10, extending in the crack propagation direction ($x$-axis). In Fig. 6.10, the thresholded distribution of void volume fraction, black for $f \leq 0.1$ and white for $f \geq 0.1$, is shown for one plane along the thickness direction ($z$-axis). In the calculations ten uniformly spaced elements are used through the thickness leading to a resolution of ten planes along this direction. Following the procedure outlined in detail in [128] the fracture surface roughness, $h(x, z)$, is calculated for both top

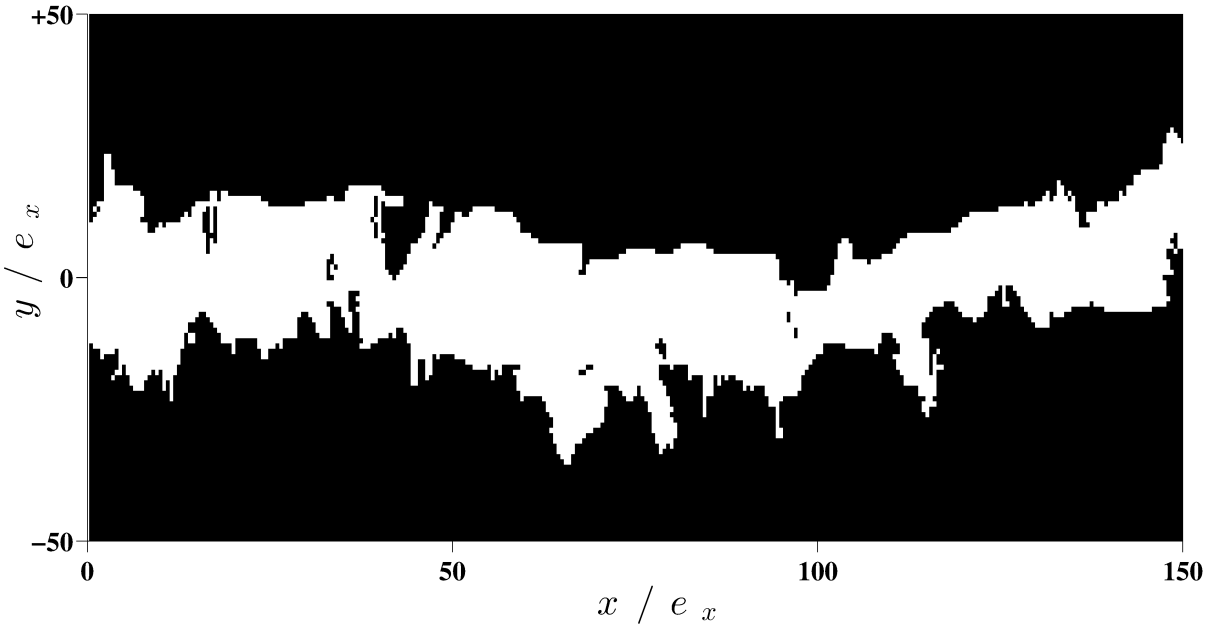


FIGURE 6.10. Distribution of the void volume fraction for one random distribution of inclusion volume fraction, $n = 0.024$ ($l_0/e_x = 8.41$), showing a propagating ductile crack. The white region corresponds to a void volume fraction, $f \geq 0.1$, and the black region corresponds to, $f < 0.1$.

and bottom fracture surfaces.

The fluctuations of heights of the fracture surface is characterized using the correlation function, $\Delta h$, defined as

$$\Delta h\left(\delta x\right) = \sqrt{\left\langle \left[h\left(x+\delta x, z\right) - h\left(x, z\right)\right]^2 \right\rangle_{x,z}} \tag{84}$$

Here, $\langle\rangle_{x,z}$ denotes the average over $x$ and $z$. The quantity $\Delta h\left(\delta x\right)$ can be interpreted as the typical difference of height between two points separated by a distance $\delta x$ along the mean fracture plane. The focus here is on the correlation of heights in the direction of crack propagation ($x$-axis) only, the width of the specimen in the perpendicular direction ($z$-axis) is too small to allow a statistical analysis of the roughness in that direction. The correlation function is computed for both top and bottom fracture surface but the final correlation function obtained by averaging over these statistically equivalent surfaces. Indeed, from symmetry arguments, the upper and lower fracture surfaces in each calculation share similar

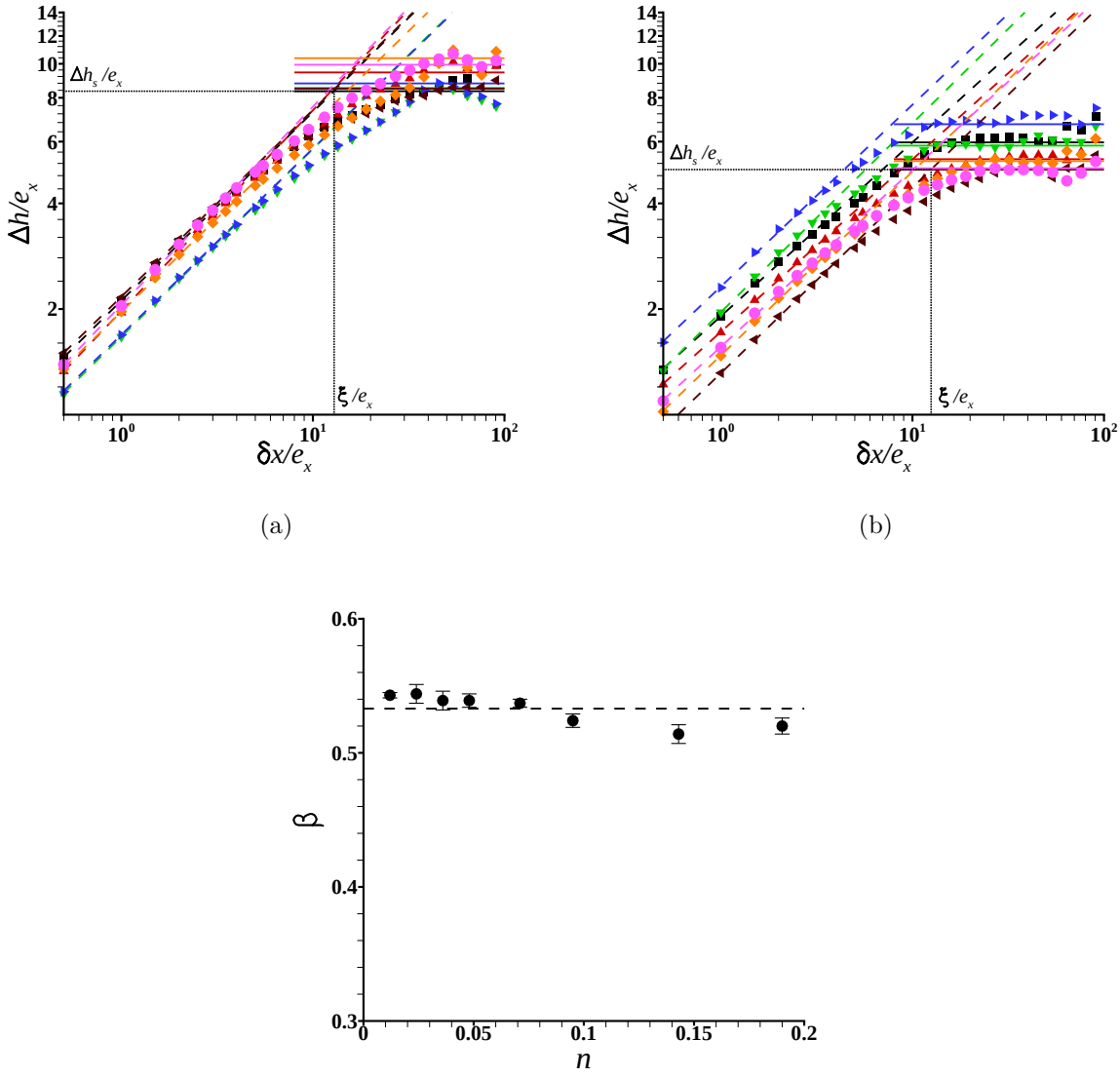


FIGURE 6.11. (a) Height-height correlation functions of the fracture surfaces for seven random distribution of inclusions corresponding to inclusion volume fraction $n = 0.024$. (b) Height-height correlation functions of the fracture surfaces for seven random distribution of inclusions corresponding to inclusion volume fraction $n = 0.143$. (c) Variation of roughness exponent $\beta$ with $n$.

statistical properties.

The correlation functions $\Delta h\,(\delta x)$ for seven random distribution corresponding to

inclusion volume fraction, $n = 0.024$, are shown in Fig. 6.11a and the same for $n = 0.143$ are shown in Fig. 6.11b on a logarithmic scale. The values of $\Delta h$ and $\delta x$ are normalized with $e_x$. Over more than two decades it has been shown that the correlation functions exhibit a power law behavior

$$\Delta h\left(\delta x\right) \propto \delta x^{\beta} \tag{85}$$

Regardless of the value of $n$ the correlation function follows a power law behavior at small scales and then saturates at a larger scale, indicating a self-affine behavior of the roughness up to some cut-off length $\xi$. The value of $\beta$ is estimated from the slope of the dashed line fitted to the initial linear portion of $\Delta h$ versus $\delta x$ curve on the log-log plot as shown in Figs. 6.11a and 6.11b. The values of $\beta$ for various $n$ are shown in Fig. 6.11c. The average roughness exponent $\beta = 0.53$ with an standard error of 0.0023 is roughly independent of the inclusion volume fraction and distribution. This captures rather well the universal self-affine nature of ductile fracture surfaces with $\beta \approx 0.6$ observed experimentally [116] and numerically [127, 128]. The correlation functions $\Delta h\left(\delta x\right)$ as shown in Figs. 6.11a and 6.11b show two roughness regimes i.e. $\beta \approx 0.53$ for $\delta x < \xi$ and $\beta \approx 0$ for $\delta x > \xi$, as marked schematically for one case in both the figures. The saturation value of the correlation function $\Delta h_s$ is also marked schematically for one case in both the Figs. 6.11a and 6.11b.

The dependence of the cut-off length, $\xi$, and the saturation value of the correlation function, $\Delta h_s$, on the inclusion volume fraction is shown in Figs. 6.12a and 6.12b. As can be seen in the figures the value of $\xi$ and $\Delta h_s$ do vary with $n$. The error bars shown in Fig. 6.12 are the standard errors estimated over seven random distributions of inclusions for a given inclusion volume fraction $n$ (for $n = 0.012$ error bars are over five random distributions). Interestingly the variation of $\xi$ as well as $\Delta h_s$ with $n$ is qualitatively similar to the variation of $J_{IC}$ with $n$ shown earlier.

In [142] the full statistics of fracture surface height fluctuations were obtained for cracks in variety of materials. It was found that the height fluctuations could be described by a distribution that differed from a Gaussian by having a power law tail. The deviation

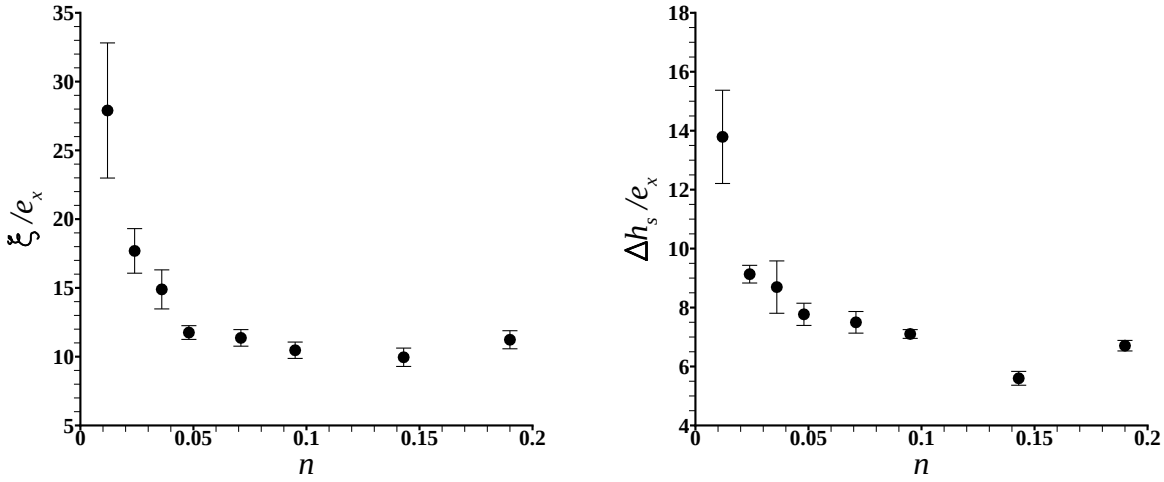


(a) (b)

FIGURE 6.12. (a) Variation of the cut-off length $\xi$ normalized with $e_x$ as a function of the inclusion volume fraction $n$. (b) Variation of the saturation value of the correlation function $\Delta h_s$ with $e_x$ as a function of the inclusion volume fraction $n$.

was found to be some what material dependent. Therefore in order to explore possible effects of inclusion volume fraction on the predicted fracture surface morphology, the full statistics of height variations $\delta h\,(x, y)$ defined by

$$\delta h\,(x, z) = h\,(x + \delta x, z) - h\,(x, z) \tag{86}$$

is also investigated.

In Eq. (86), the roughness $h\,(x, z)$ is the average roughness of the fracture surfaces obtained from all random distribution of inclusions for a given inclusion volume fraction. Hence in total eight cases corresponding to eight inclusion volume fractions have been analyzed. Also as expected the top and bottom fracture surfaces are roughly symmetric hence the focus here is confined on the top fracture surfaces only. For a fixed length scale $\delta x$, a histogram of $\delta h$ is generated and from the histogram a probability density $p\,(\delta h \mid \delta x)$ is obtained. The histogram of $\delta h$ is calculated by placing the values of $\delta h$ into bins where the histogram bins are homogeneously distributed between $\min[\delta h]$ and $\max[\delta h]$. A detailed procedure of gen-

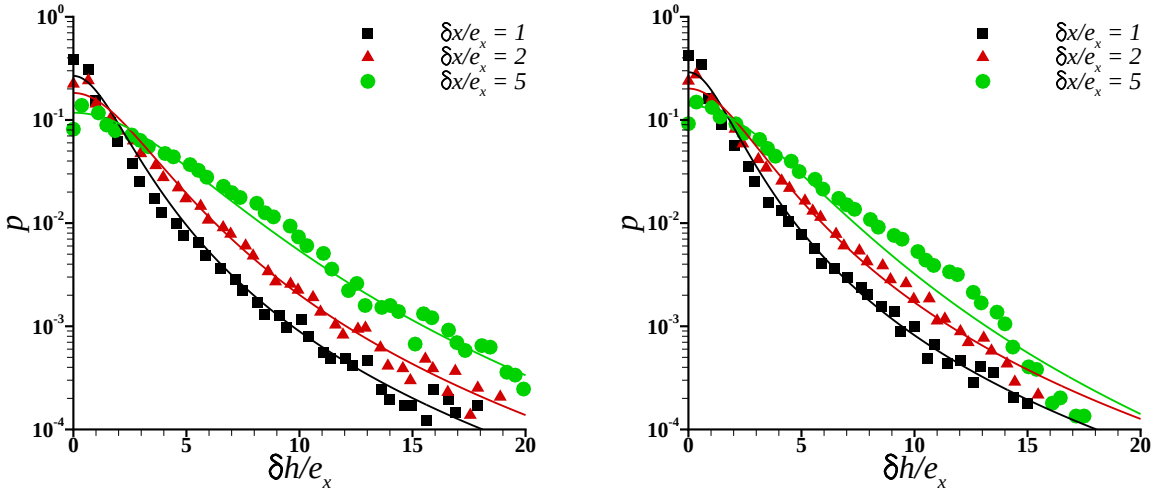


FIGURE 6.13. Histograms $p\,(\delta h \mid \delta x)$ of height variations $\delta h$, see Eq. (86), for various values of $\delta x$, (a) for inclusion volume fraction $n = 0.024$ and (b) for inclusion volume fraction $n = 0.143$. The solid lines are the fit based on the Student's t-distribution in Eq. (87) using various values of the parameter $k$.

erating the probability densities is outlined in [128]. In order to study the scaling behavior of the fracture surface roughness, this procedure is repeated for various scales $\delta x$. An important property is that the standard deviation of the distributions $p\,(\delta h \mid \delta x)$ corresponds to the correlation function $\Delta h\,(\delta x)$ of the fracture surfaces.

The distribution $p\,(\delta h \mid \delta x)$ is shown for three values of $\delta x$ in Fig. 6.13a for inclusion volume fraction $n = 0.024$ and in Fig. 6.13b for inclusion volume fraction $n = 0.143$. It can be seen in both the figures that the larger the value of $\delta x$, the broader the distribution, as expected from the scaling of the correlation function $\Delta h\,(\delta x) \propto \delta x^{\beta}$. It is quite evident that the distribution of height variations computed on numerical fracture surfaces are not Gaussian, but exhibit fat tails with power law behavior $p\,(\delta h) \propto \delta h^{(k+1)/2}$ for larger values of $\delta h$. this means that the large fluctuations are not exponentially rare on ductile fracture surfaces as is the case for brittle fracture surfaces [141]. To describe this effect more quantitatively, the distribution $p\,(\delta h)$ are described using a family of probability distributions referred to

as Student's t-distributions

$$p_{k,\delta h_c}(\delta h) \propto \frac{1}{\delta h_c}\left(1+\frac{1}{k}\left(\frac{\delta h}{\delta h_c}\right)^2\right)^{-(k+1)/2} \tag{87}$$

with parameters $k$ and $\delta h_c$, and the fits of Student's t-distribution function are represented by solid lines in Fig. 6.13. The fit of the Student's t-distribution function in Fig. 6.13 reveals that the scaling of the roughness distribution of ductile fracture surfaces can be described using Student' $t_{k,\delta h_c}$-distribution function.

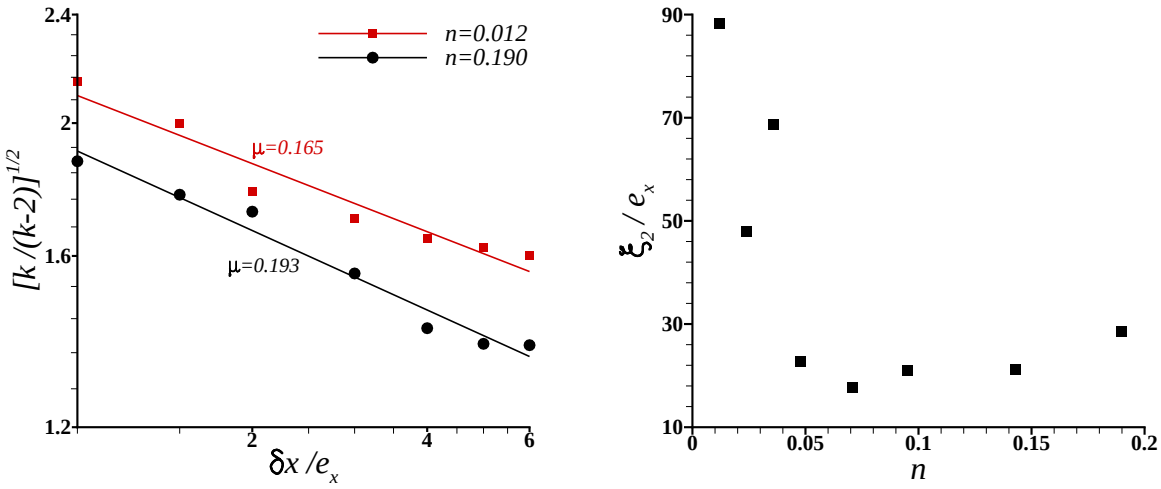


(a) (b)

FIGURE 6.14. (a) Variations of the parameter $\sqrt{k/(k-2)}$ obtained from the fit of Student's t-distribution function to $P(\delta h_c)$ versus $\delta h$ plots as shown in Fig. 6.13 with length scale $\delta x$. (b) Variation of $\xi_2$ with inclusion volume fraction $n$, where $\xi_2$ is the value of $\delta x$ at which $\sqrt{k/(k-2)} \simeq 1$.

The parameter $k$ in Eq. (87) characterizes the shape of the distribution function. For a finite value of $k$, the Student's t-distribution displays fat tails while the distribution approaches Gaussian as $k$ tends to infinity. Hence this family of distributions is well suited to describe a transition from power law to Gaussian statistics which is in general observed for brittle materials [141]. In this context it is more appropriate to consider the parameter

$\sqrt{k/(k-2)}$ instead of $k$ [128]. The variation of the parameter $\sqrt{k/(k-2)}$ with the scale $\delta x$ for two inclusion volume fractions $n = 0.012$ and $n = 0.190$ are shown in Fig. 6.14a on a logarithmic scale. As shown in Fig. 6.14a, $\sqrt{k/(k-2)} \propto \delta x^{-\mu}$ with $\mu = 0.165$ for $n = 0.012$ and $\mu = 0.193$ for $n = 0.190$. As stated earlier for Gaussian distribution $k$ tends to infinity or equivalently $\sqrt{k/(k-2)} \simeq 1$. Extrapolating the power law behavior $\sqrt{k/(k-2)} \propto \delta x^{-\mu}$ towards larger values of $\delta x$, predicts that it will reach $\sqrt{k/(k-2)}_{(\delta x=\xi_2)} \simeq 1$ at the cross over length $\delta x \simeq \xi_2$. It suggests that for $\delta x > \xi_2$, the fracture surface might recover Gaussian statistics. The dependence of this cross over length $\xi_2$ with inclusion volume fraction is shown in Fig. 6.14b. Interestingly a generally decreasing trend of $\xi_2$ with inclusion volume fraction can be seen in Fig. 6.14b. Indeed it has been shown earlier that the fracture toughness decreases with increasing inclusion volume fraction $n$ i.e. the material tends to loose ductility with increasing $n$. Here Fig. 6.14b, shows that with increasing $n$, it is easier to reach a Gaussian statistics which correspond to brittle fracture.

6.5. Toughness-Roughness Correlation

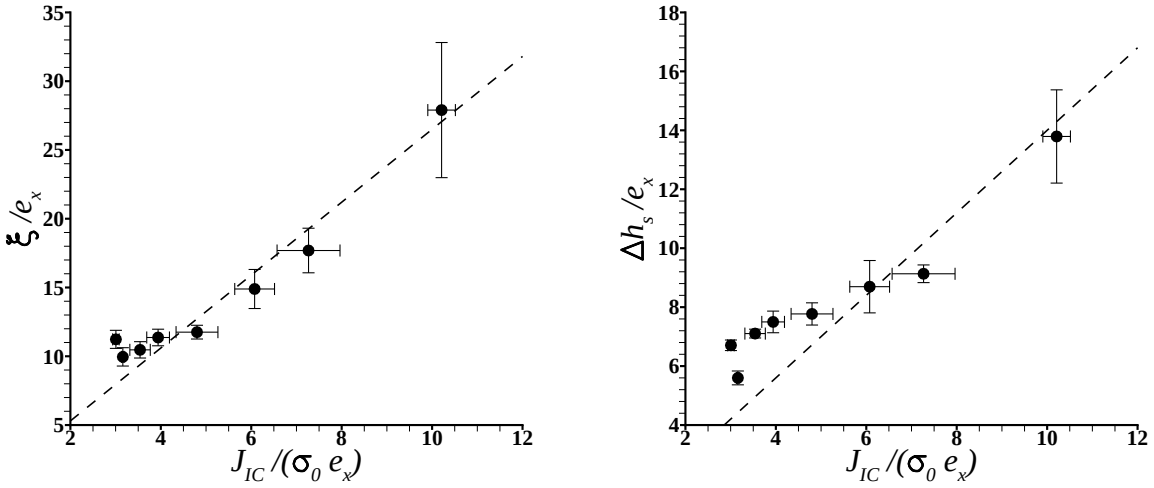


(a) (b)

FIGURE 6.15. (a) Variation of the normalized cut-off length $\xi/e_x$ with the normalized fracture toughness $J_{IC}/(\sigma_0 e_x)$. (b) Variation of the saturation value of the correlation function $\Delta h_s$ normalized with $e_x$ with $J_{IC}/(\sigma_0 e_x)$.

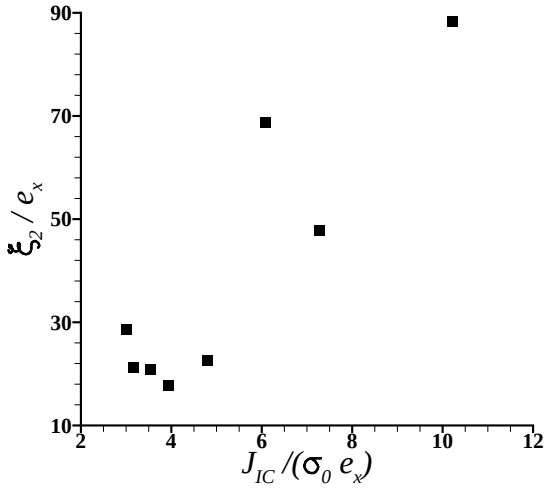


(a)

FIGURE 6.16. Variation of the cross-over length $\xi_2$ normalized with $e_x$ with the normalized fracture toughness $J_{IC}/(\sigma_0 e_x)$.

The variation of the normalized cut-off length $\xi/e_x$ with the normalized fracture toughness $J_{IC}/(\sigma_0 e_x)$, Fig. 6.15a, and the variation of the normalized saturation value of the correlation function $\Delta h_s/e_x$ with $J_{IC}/(\sigma_0 e_x)$, Fig. 6.15b, shows a clear correlation. The value of $J_{IC}$ in Fig. 6.15 is the one obtained using [140]. The straight dashed line $\xi/e_x = \alpha J_{IC}/(\sigma_0 e_x)$ illustrate the trend in Fig. 6.15. The value of $\alpha$ for $\xi$ versus $J_{IC}/\sigma_0$ correlation is 2.65 and that for $\Delta h_s$ versus $J_{IC}/\sigma_0$ correlation is 1.4 for $J_{IC}$ obtained using ASTM standard. The value of $\alpha$ decreases slightly when $\xi$ or $\Delta h_s$ are plotted with $J_{\Delta a=l_0}/\sigma_0$. Regardless of the value of $\alpha$ it is quite interesting that there exists a correlation between a measure of fracture surface roughness and fracture toughness. The linear correlation between fracture surface roughness and fracture toughness breaks down for large inclusion volume fractions especially for $n \geq 0.143$. The variation of the normalized cross over length $\xi_2/e_x$ with $J_{IC}/(\sigma_0 e_x)$ is shown in Fig. 6.16. There is no direct correlation between $\xi_2$ and $J_{IC}/\sigma_0$ but indeed a four fold drop in the value of $\xi_2/e_x$ with a roughly four fold drop in the value of $J_{IC}/(\sigma_0 e_x)$ can be seen in Fig. 6.16.

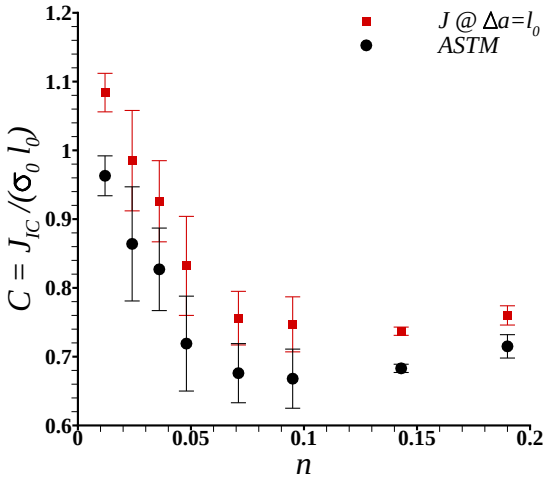


(a)

FIGURE 6.17. Variation of the normalized $J_{IC}$, $J_{IC}/(\sigma_0 l_0)$, with the inclusion volume fraction, $n$.

## 6.6. Discussion

To understand $\xi$ versus $J_{\mathrm{IC}}$ correlation, first the mechanisms that set the length scale $\xi$ is examined. Previous experimental studies on glass and mortar fracture surfaces have reported two scaling regimes $\Delta h \sim \delta x^{\beta}$, with $\beta^{\mathrm{damage}} \simeq 0.6$ at small length scales $\delta x < \xi$ and $\beta^{\mathrm{brittle}} \simeq 0.5$ at larger length scales $\delta x > \xi$ [143, 144]. In phase-separated glass samples, two regimes were also reported, but the second regime was characterized by logarithmic correlations of height fluctuations, coinciding with $\beta^{\mathrm{brittle}} \simeq 0$ [145]. These large scale behaviors could be captured quantitatively by linear elastic fracture mechanics based models of crack propagation within disordered brittle solids [146, 143], indicating that beyond the scale $\xi$, fracturing solids behave as a coarse-grained equivalent linear elastic medium. For brittle solids, this suggests an interpretation of the length $\xi$ in terms of process zone size, or extension of the zone in the crack tip vicinity where linear elasticity breaks down.

For ductile materials large plastic strains and crack tip blunting precede the initiation of crack growth. Also, the driving force for crack growth increases with progressive crack advance (stable crack growth). For a homogeneous elastic-plastic continuum in small scale

yielding the plastic zone size as well as crack tip opening displacement are linearly related to $J/\sigma_0$. In addition, if there is a single dominant length scale characterizing the micro-scale fracture process, dimensional considerations require that length scale to be linearly related to $J/\sigma_0$. For example, in models presuming an initial void near the crack tip [122, 123], that the crack tip opening displacement (a measure of crack tip blunting) required for the crack initiation is linearly related to the distance of the void from the crack tip. This leads to a linear relation between a micro-scale length, the distance of the void from the crack tip, and a macro-scale length $J_{Ic}/\sigma_0$. Alternatively, this can be expressed in terms of a relation between the distance of the initial void from the crack tip and the crack tip opening displacement at crack initiation. Also, in the model of Ref. [125] that considers a void by void ductile failure process, the length scale introduced to define the distance from the crack tip at which void nucleation is assumed to occur was proportional to $J/\sigma_0$.

In Fig. 6.15a, $J_{\mathrm{IC}}$ is a measure of resistance to the initiation of crack growth while $\xi$ relates to the deviation from self-affine roughness which occurs after a significant amount of crack growth and thus at a different value of $J$. However, both are related to the volume fraction of large particles $n$ or equivalently to the mean large particle spacing $X_0$ as seen in Figs. 6.12a and 6.9. Hence, as long as the fracture process and the fracture surfaces roughness are dominated by a single microstructural length scale, $\xi$ and $J_{\mathrm{IC}}/\sigma_0$ are expected to be linearly related as seen in Fig. 6.15a for the larger values of $n$. Also, since the plastic zone size scales with $J/\sigma_0$, $\xi$ is linearly related to the plastic zone size. The same argument explains the correlation of $\Delta h_s$, Fig. 6.15b, and $\xi_2$, Fig. 6.16, with $J_{IC}$.

The deviation from a linear relation seen for smaller values of $\xi$ or $\Delta h_s$, corresponding to higher volume fraction of large particles or smaller mean particle spacings, deviations from a linear relationship occur that may be interpreted in terms of the two limiting mechanisms discussed in [124]: void by void crack growth and multiple void (or more generally defect) interaction crack growth. While the calculations in [124] were idealized, the dimensionless parameter $C = J_{\mathrm{IC}}/\left(\sigma_0 X_0\right)$ introduced in [124] can provide a decent estimate of the transition between the two limiting mechanisms of ductile crack growth. In the calculations here,

Fig. 6.17, $C = 0.96$ for $n = 0.012$ and saturates to a value of $C \approx 0.68$ for $n \geq 0.071$(a saturation in the value of $J_{\rm IC}$, $\xi$, $\Delta h_s$ and $\xi_2$ for $n \geq 0.071$ can also be seen in Figs. 6.9, 6.12 and 6.14b). A rough comparison of the results here with those in [124] suggests that the void by void crack growth is the dominant mechanism for $n < 0.071$ and multiple defect interaction crack growth dominates for $n \geq 0.071$. Hence when multiple defect interactions become more prevalent the mean particle spacing is no longer the only relevant roughness length scale.

Nevertheless, for all cases considered here, as for brittle solids there are two roughness regimes of roughness exponent, i.e. $\beta^{\rm ductile} \simeq 0.55$ for $\delta x < \xi$ and $\beta^{\rm ductile} \simeq 0$ for $\delta x > \xi$, consistent with the experimental observations on aluminum alloys in [147]. However, unlike for brittle solids, this transition in the value of $\xi$ is not associated with linear elasticity breaking down near the crack tip since the crack tip stress and strain fields, and indeed those in the fracture process zone, lie within the continuum plastic zone.

Ductile fracture by void nucleation, growth and coalescence necessarily involves more than one length scale. For example in addition to the particle (or void) spacing there is the particle (or void) size, the size and spacing of micro-cracks nucleated away from the main crack, etc. Furthermore, in grid based numerical calculations, as carried out here, there is the grid spacing. The issue is when, or if, circumstances exist where a single length scale dominates. Studies of the effect of additional length scales on the correlation of toughness and roughness can be carried out using the same theoretical and computational framework as in the present analyses. In addition, a quite realistic description of the large particles could be obtained by assuming different particle sizes and by taking the parameters governing void nucleation from a statistical distribution.

## 6.7. Summary and Conclusions

The calculations show:

- that with a random distribution of void nucleating particles and fixed material properties, the mean spacing of particles is the dominant length scale;

- that an appropriate statistical length scale is the one, $\xi$, marking the deviation from self-affine roughness;
- $\xi$ is linearly related to $J_{\mathrm{IC}}$ as long as one length scale characterizes the fracture process and the fracture surface roughness.

This provides a step toward fulfilling the hope that the statistical characterization of ductile fracture surface roughness may be used for a post-mortem estimate of fracture toughness.

# CHAPTER 7

# CONCLUDING REMARKS AND FUTURE WORK

## 7.1. Concluding Remarks

The thickness debit effect in the creep response of single crystal Ni-based superalloys was investigated experimentally. The experimental observations of the creep response of single crystal Ni-based superalloys supplemented by microstructural analyses and finite element calculations rationalized the probable mechanisms leading to the debit effect. These observations also motivated a basic mechanics studies of porosity evolution in single crystals subjected to creep loading. The study was performed using three-dimensional finite deformation finite element analyses of unit cells containing a single initially spherical void in a single crystal matrix. These calculations uncovered new insights into the response of voids in a single crystal matrix under various stress states. Based on the experimental observations and results of finite element calculations a quantitative mechanistic model accounting for both bulk and surface damage effects to assess their relative roles in the observed thickness debit effect was formulated. The model showed very good correlation with the experimental results and also correlated several features of the material's microstructure such as initial voids and nucleation of new voids at high temperatures that if controlled could lead to better properties. Another set of calculations aimed at relating the crack growth resistance and fracture surface morphology of ductile materials. For thirty years, the hope to relate the statistical characterization of fracture surfaces to a measure of a materials crack growth resistance remained unfulfilled. Remarkably for the first time a correlation between fracture surface roughness and fracture toughness was shown in this work.

## 7.2. Future Work

In light of the work presented in this dissertation, several directions might be investigated in the future.

- The role of initial voids at low temperatures and the role of nucleation of new voids at high temperatures in the observed thickness debit effect in the creep response of

single crystal superalloys is one key finding of the current work. Eliminating the initial voids in the single crystal superalloys by hot isostatic pressing (HIP) and then exploring the creep response and the effect of specimen thickness on the creep response at least at low temperatures can be carried out in the immediate future. On the other hand there is a very limited understanding of void nucleation in single crystal superalloys at high temperature. In the model proposed here the void nucleation was assumed to follow a Gaussian statistics which is not phenomenological but brings out the role of void nucleation on creep rupture. A better understanding of void nucleation will not only improve the model but will also help industry in reducing the extent of void nucleation.

- The key findings of the basic mechanistic study of porosity evolution in a single crystal matrix carried out in the current work is the evolution of void shape and the stress concentrations associated with the evolving void shape. Additional parameter studies are needed to determine the orientation dependence of the porosity evolution. The results of such analyses together with the results obtained here could provide the background for developing a phenomenological constitutive relation for evolution of damage in a creeping single crystal. Such a constitutive relation will be of great industrial importance and will significantly improve the life time prediction scheme of jet engine turbine blades.
- In the other set of calculations the focus was confined to simulating ductile fracture due to void nucleation, growth and coalescence. It was chosen in the current work to let variations in the volume fraction of void nucleating second phase particles represent the variation of the microstructure that led to the variation in the crack growth resistance and fracture surface roughness. It could be interesting to also study the correlation of toughness and roughness corresponding to variations in the strength of these void nucleating second phase particles. Furthermore, changing the size of the second phase particles while keeping their volume fraction fixed would also change the microstructural length scale. Hence a more realistic description

of the second phase particles can be obtained from a statistical distribution and a detailed roughness-toughness correlation can be explored to achieve the dream of quantitative fractography.

# BIBLIOGRAPHY


[1] Gell M., Duhl D.N. and Giamei A.F., The development of single crystal superalloy turbine blades. Superalloys 1980, 205-214.

[2] Koff B.L., Gas turbine technology evolution: A designers perspective. Journal of Propulsion and Power 20 (2004), 577595.

[3] Pandey M.C., Dyson B.F. and Taplin D.M.R., Environmental, Stress-State and Section-size synergisms During Creep. Proc. R. Soc. Lond., Ser. A (1984), 117-131.

[4] Doner M. and Heckler J.A., Effects of section thickness and orientation on creep rupture properties of two advanced single crystal alloys. SAE technical paper 851785, Society of Automative Engineers Inc. (1985).

[5] Duhl D.N., Directionally solidified superalloys, in Superalloys II, C.T. Sims, N.S. Stoloff, and W.C. Hagel, (Eds.), John Wiley, New York (1987), 189-214.

[6] Doner M. and Heckler J.A., Identification of mechanism responsible for degradation in thin-wall stress rupture properties. Superalloys 1988, Proceedings of the $6^{th}$ international symposium on superalloys, The metallurgical society, Warrendale, PA (19880, 653-662.

[7] Duhl D.N., Single crystal superalloys, Superalloys, Supercomposites and Superceramics, J.K. Tien and T. Caulfield (Eds.), Academic Press, Inc. New York, NY (1989), 149-182.

[8] Pandey M.C. and Taplin D.M.R., Prediction of rupture lifetime in thin sections of a nickel base superalloy. Scripta Metallurgica et Materialia 31 (1994), 719-722.

[9] Baldan A., On the thin-section size dependent creep strength of a single crystal nickel-base superalloy. Journal of materials science 30 (1995), 6288-6298.

[10] Seetharaman V. and Cetel A.D., Thickness Debit in Creep Properties of PWA1484. Superalloys 2004, TMS, The Minerals, Metals and Materials Society (2004), 207-214.

[11] Henderson P.J., Creep of single crystal Ni-base superalloy in thick and thin section

forms. Creep and fracture of engineering materials and structures, ed. J.C. Earthman and F.A. Mohamed (1997), 697-706.

[12] Henderson P.J., Creep of coated and uncoated thin-section CMSX-4. Materials for advanced power engineering, Forschungszentrum Juelich GmbH (1998), 1559-1568.

[13] Hüttner R., Völkl R., Gabel J. and Glatzel U., Creep behavior of thick and thin walled structures of a single crystal Ni-base superalloy at high temperatures-Experimental method and results. Superalloys 2008, R.C. reed, K.A. Green, P. Carron, T.P. Gabb, M.G. Fahrmann, E.S. Huron and S.A. Woodard, TMS, The Minerals Metals and Materials Society (2008), 719-723.

[14] Hüttner R., Gabel J., Glatzel U. and Völkl R., First creep results on thin-walled single-crystal superalloys. Material science and engineering A 510-511 (2009), 307-311.

[15] Cetel A.D. and Duhl D.N., Second Generation Nickel Base Single Crystal Superalloy. Superalloys 1988, Proceedings of the 6th International Symposium on Superalloys, The Metallurgical Society, Warrendale, PA (1988), 235-244.

[16] Cane B.J. and Townsend R.D., Prediction of Remaining Life in Low-alloy Steels. In: Raj R. (Ed.), Flow and Fracture at Elevated Temperatures, American Society of Metals, Metals Park, Ohio 44703, USA (1985), 279-316.

[17] Storesund J. and Tu S.T., Geometrical effect on creep in cross weld specimens. Int. J. Pres. Ves. & Piping 62(1995), 179-193.

[18] Ueno A., Takami N. and Sato R., In: J. Pokluda (Ed.), Proceedings of the 17th European Conference of Fracture, Brno, Czech Republic (2008), 1120-1127.

[19] Villain J., Brueller O.S. and Qasim T., Creep behaviour of lead free and lead containing solder materials at high homologous temperatures with regard to small solder volumes. Sensors and Actuators A 99 (2002), 194-197.

[20] Ashby M.F., The deformation of plastically non-homogeneous materials. Philosophical Magazine 21 (1970), 399-424.

[21] Ma Q. and Clarke D.R., Size dependent hardness of silver single crystals. Journal of Materials Research 10 (1995), 853863.

[22] Lou J., Shrotriya P., Buchheit T., Yang D. and Soboyejo W.O., Nanoindentation study of plasticity length scale effects in LIGA Ni microelectromechanical systems structures. Journal of Materials Research 18 (2003), 719728.

[23] Poole W.J., Ashby, M.F. and Fleck N.A., Micro-hardness of annealed and work-hardened copper polycrystals. Scripta Materialia, 1996, 34, 559564.

[24] Nix W.D. and Gao H., Indentation size effects in crystalline materials: a law for strain gradient plasticity. Journal of the Mechanics and Physics of Solids 43 (1995), 411423.

[25] Uchic M.D., Dimiduk D.M., Florando J.N. and Nix W.D., Sample dimensions influence strength and crystal plasticity. Science (305) 2004, 986989.

[26] Greer J.R., Oliver W.C. and Nix W.D., Size dependence of mechanical properties of gold at the micron scale in the absence of strain gradients. Acta Materialia 53 (2005), 1821-1830.

[27] Nicola L., Xiang Y., Vlassak J.J., Van der Giessen E. and Needleman A., Plastic deformation of freestanding thin films: experiments and modeling. Journal of the Mechanics and Physics of Solids 54 (2006), 2089-2110.

[28] Kiener D., Guruprasad P.J., Keralavarma S.M., Dehm G. and Benzerga A.A., Work hardening in micropillar compression: In situ experiments and modeling, Acta Materialia 59 (2011), 3825-3840.

[29] Benzerga A.A., Micro-pillar plasticity: 2.5D mesoscopic simulations. Journal of the Mechanics and Physics of Solids 57 (2009), 1459-1469.

[30] Rao S.I., Dimiduk D.M., Parthasarathy T.A., Uchic M.D., Tang M. and Woodward C., Athermal mechanisms of size-dependent crystal flow gleaned from three-dimensional discrete dislocation simulations. Acta Materialia 56 (2008), 3245-3259.

[31] Kraft O., Gruber P.A., M önig R. and Weygand D., Plasticity in confined dimensions. Annual Review of Materials Research 40 (2010), 293-317.

[32] Greer J.R. and De Hosson J.Th.M., Plasticity in small-sized metallic systems: intrinsic versus extrinsic size effect. Progress in Materials Science 56 (2011), 654-724.

[33] Zupan M., Hayden M.J., Boehlert C.J. and Hemker K.J., Development of high temperature microsample testing. Experimental Mechanics 41 (2001), 242247.

[34] K.J. Hemker and W.N. Sharpe Jr., Microscale Characterization of Mechanical Properties. Annual Reviews of Materials Research 37 (2007), 93-126.

[35] Gullickson J., Needleman A., Staroselsky A. and Cassenti B., Boundary damage effects on the evolution of creep strain. Modelling and Simulation in Materials Science and Engineering 16 (2008), 075009.

[36] Cassenti B. and Staroselsky A., The effect of thickness on the creep response of thin-wall single crystal components. Materials Science and Engineering A 508 (2009), 183-189.

[37] Bensch M., Preußner J., Hüttner R., Obigodi G., Virtanen S., Gabel J. and Glatzel U., Modelling and analysis of the oxidation influence on creep behaviour of thin-walled strutures of the single-crystal nickel-base superalloy René N5 at 980°C. Acta Materialia 58 (2010), 1607-1617.

[38] Duhl D.N. and Cetel A.D., Advanced high strength single crystal superalloy compositions, U.S. Patent 4719080, January 12 (1988).

[39] Anton D.L. and Giamei A.F., Porosity distribution and growth during homogenization in single crystals of a nickel-base superalloy. Materials Science and Engineering 76 (1985), 173-180.

[40] Link T., Zabler S., Epishin A., Haibel A., Bansal M. and Thibault X., Synchrotron tomography of porosity in single-crystal nickel-base superalloys. Materials Science and Engineering A 425 (2006), 47-54.

[41] Li L. and Overfelt R.A., Influence of directional solidification variables on the cellular and primary dendrite arm spacings of PWA1484. Journal of Materials Science 37 (2002), 3521-3532.

[42] Rae C.M.F. and Reed R.C., Primary creep in single crystal superalloys: Origins, mechanisms and effects. Acta Materialia 55 (2007), 1067-1081.

[43] Wilson B. and Fuchs G., Primary creep: secondary gamma prime and the rhenium effect. JOM Journal of the Minerals, Metals and Materials Society 60 (2008), 43-48.

[44] Sherry A.H. and Pilkington R., The creep fracture of a single-crystal superalloy. Materials Science and Engineering A 173 (1993), 51-61.

[45] ASM Handbook, Fractography, Volume 12 (1987).

[46] MacKay R.A. and Ebert L.J., The development of $\gamma - \gamma'$ lamellar strutures in a Ni-base superalloy during elevated temperature mechanical testing. Metallurgical Transactions A 16A (1985), 19691982.

[47] Pollock T.M. and Argon A.S., Directional coarsening in nickel-base single crystals with high volume fractions of coherent precipitates. Acta Metallurgica Materialia 42 (1994), 1859-1874.

[48] Reed R.C., Matan N., Cox D.C., Rist M.A. and Rae C.M.F., Creep of CMSX-4 superalloy single crystals: Effects of rafting at high temperature. Acta Materialia 47 (1999), 3367-3381.

[49] Akhtar A., Hegde S. and Reed R.C., The oxidation of single-crystal nickel-based superalloys. JOM Journal of the Minerals, Metals and Materials Society 58 (2006), 37-42.

[50] Moverare J.J. and Johansson S. Damage mechanisms of a high-Cr single crystal superalloy during thermomechanical fatigue. Materials Science and Engineering: A 527 (2010), 553-558.

[51] Bond S.D. and Martin J.W., Surface recrystallization in a single crystal nickel-based superalloy. Journal of Materials Science 19 (1984), 3867-72.

[52] Meng J., Jin T., Sun X. and Hu Z., Surface recrystallization of a single crystal nickel-base superalloy. International Journal of Minerals, Matallurgy and Materials 18 (2011), 197-202.

[53] Epishin A. and Link T., Mechanisms of high-temperature creep of nickel-based superalloys under low applied stresses. Philosophical Magazine 84 (2004), 1979-2000.

[54] ABAQUS User's Manual, version 6.6 (2006), ABAQUS Inc., Providence, RI.

[55] Needleman A., Void growth in an elasticplastic medium. Journal of Applied Mechanics 39 (1972), 964970.

[56] Tvergaard V., Influence of voids on shear band instabilities under plane strain conditions. International Journal of Fracture 17 (1981), 389-407.

[57] Tvergaard V. On localization in ductile materials containing spherical voids. International Journal of Fracture 18 (1982), 237-252.

[58] Koplik J. and Needleman A., Void growth and coalescence in porous plastic solids. International Journal of Solids and Structures 24 (1988), 835853.

[59] Worswick M.J. and Pick P.J., Void growth and constitutive softening in a periodically voided solid. Journal of Mechanics and Physics of Solids 38 (1990), 601-625.

[60] Faleskog J. and Shih C.F., Micromechanics of coalescence-I. Synergistic effects of elasticity, plastic yielding, and multi-size-scale voids. Journal of Mechanics and Physics of Solids 45 (1997), 21-50.

[61] Pardoen T. and Hutchinson J.W., An extended model for void growth and coalescence. Journal of Mechanics and Physics of Solids 48 (2000), 2467-2512.

[62] Horstemeyer M.F. and Ramaswamy S., On factors affecting localization and void growth in ductile metals: a parametric study. International Journal of Damage Mechanics 9 (2000), 528.

[63] Zhang K.S., Bai J.B. and Francois D., Numerical analysis of the influence of the Lode parameter on void growth. International Journal of Solids and Structures 38 (2001), 58475856.

[64] Gao X. and Kim J., Modeling of ductile fracture: significance of void coalescence. International Journal of Solids and Structures 43 (2006), 62776293.

[65] Nahshon K. and Hutchinson J.W., Modification of the Gurson model for shear failure. European Journal of Mechanics A/Solids 27 (2008), 1-17.

[66] Barsoum I. and Faleskog J., Micromechanical analysis on the influence of the Lode parameter on void growth and coalescence. International Journal of Solids and Structures 48 (2011), 925-938.

[67] Bao Y. and Wierzbicki, T., On fracture locus in the equivalent strain and stress triaxiality space. International Journal of Mechanical Sciences 46 (2004), 81-98.

[68] Hori M. and Nemat-Nasser S., Mechanics of void growth and void collapse in crystals. Mechanics of Materials 7 (1988), 1-13.

[69] O'Regan T.L., Quinn D.F., Howe M.A. and McHugh P.E., Void growth simulations in single crystals. Computational Mechanics 20 (1997), 115121.

[70] Orsini V.C. and Zikry M.A., Void growth and interaction in crystalline materials. International Journal of Plasticity 17 (2001), 1393-1417.

[71] Potirniche G.P., Hearndon J.L., Horstemeyer M.F. and Ling X.W., Lattice orientation effects on void growth and coalescence in fcc single crystals. International Journal of Plasticity 22 (2006), 921-942.

[72] Kysar J.W., Gan Y.X. and Mendez-Arzuza G., Cylindrical void in a rigid-ideally plastic single crystal. Part I: Anisotropic slip line theory solution for face-centered cubic crystals. International Journal of Plasticity, 21 (2005), 1481-1520.

[73] Schacht T., Untermann N. and Steck E., The influence of crystallographic orientation on the deformation behavior of single crystals containing microvoids. International Journal of Plasticity 19 (2003), 1605-1626.

[74] Wan J.S., Yue Z.F. and Lu Z.Z., Casting microporosity growth in single-crystal superalloys by a three dimensional unit cell analysis. Modelling and Simulation in Material Science and Engineering 13 (2005), 875-892.

[75] Wan J.S., Lu Z.Z. and Yue Z.F., Growth of casting microcrack and micropore in single crystal superalloys analysed by three dimensional unit cell. Journal of Material Science and Technology 2 (2006), 183-189.

[76] Liu W.H., Zhang X.M., Tang J.G. and Du Y.X., Simulation of void growth and coalescence behavior with 3D crystal plasticity theory. Computational Materials Science 40 (2007), 130-139.

[77] Yang M. and Dong X., Simulation of lattice orientation effects on void growth and

coalescence by crystal plasticity. Acta Metallurgica Sinica (English Letters) 22 (2009), 40-50.

[78] Sangyul H. and Kim K., Void growth and coalescence in fcc single crystals. International Journal of Mechanical Sciences 52 (2010), 863-873.

[79] Yerra S.K., Tekoglu C., Scheyvaerts F., Delanny L., Van Houtte P. and Pardoen T., Void growth and coalescence in single crystals. International Journal of Solids and Structures 47 (2010), 1016-1029.

[80] Yu Q.M., Hou N.X. and Yue Z.F., Finite element analysis of void growth behavior in nickle-based single crystal superalloys. Comutational Materials Science 48 (2010), 597-608.

[81] Budiansky B., Hutchinson J.W. and Slutsky S., Void growth and collapse in viscous solids, Mechanics of solids (ed. H.G. Hopkins and M.J. Sewell), Oxford: Pregamon Press (1982), 13-45.

[82] Dennis R. J., Mechanistic modelling of deformation and void growth behaviour in superalloy single crystals, PhD thesis, Imperial College London (2000).

[83] Busso E.P., O'Dowd N.P. and Dennis R.J., A rate dependent formulation for void growth in single crystal materials. IUTAM Sympossium on Creep in Structurees (eds. S. Murakani and N.Ohno), Kluwer Academic Publishers ( 2001), 41-50.

[84] Needleman A., Tvergaard V., and Van der Giessen E., Evolution of void shape and size in creeping solids. International Journal of Damage Mechanics 4 (1995), 134-152.

[85] Needleman A. and Rice J.R., Plastic creep flow effects in the diffusive cavitation of grain boundaries. Acta Metallurgica, 28 (1980), 1315-1332.

[86] Cocks A.C.F. and Ashby M.F., On creep fracture by void growth. Progress in Materials Science 27 (1982), 189-244.

[87] Srivastava A., Void growth and collapse in a creeping single crystal. Masters Thesis, University of North Texas (2011).

[88] Huang Y., Harvard University Report Mech-178 (1991).

[89] Kysar J.W., unpublished report (1997).

[90] Asaro R.J. and Needleman A., Texture development and strain hardening in rate dependent polycrystals. Acta Metallurgica 33 (1985), 923-953.

[91] Asaro R.J., Crystal plasticity. Journal of Applied Mechanics 50 (1983), 921-934.

[92] Danas K. and Ponte Castaneda P., A finite strain model for anisotropic viscoplastic porous media: I - Theory. European Journal of Mechanics A/Solids 28 (2009), 387-401.

[93] Tvergaard,V., Material failure by void growth to coalescence. Advances in Applied Mechanics 27 (1990), 83-151.

[94] Benzerga A. and Leblond J-B., Ductile fracture by void growth to coalescence. Advances in Applied Mechanics 44 (2010), 169305.

[95] Banks-Sills L. and Budiansky B., On void collapse in viscous solids. Mechanics of Materials 1 (1982), 209-218.

[96] Nemat-Nasser S. and Hori M., Void collapse and void growth in crystalline solids. Journal of Applied Physics 62 (1987), 2746-2757.

[97] Lee B.J. and Mear M.E., Studies of the growth and collapse of voids in viscous solids. Journal of Engineering Materials and Technology 116 (1994), 348-358.

[98] Mohan R. and Brust F.W., On void growth in elastic-nonlinear viscous solids under creep and cyclic creep conditions. Journal of Engineering Materials and Technology 122 (2000), 283-293.

[99] Kim J., Gao X. and Srivastsan T.S., Modeling of void growth in ductile solids: effects of stress triaxiality and initial porosity. Engineering Fracture Mechanics 71 (2004), 379-400.

[100] Danas K. and Aravas N., Numerical modeling of elasto-plastic porous materials with void shape effects at finite deformations. Composites: Part B (2012), doi:10.1016/j.compositesb.2011.12.011.

[101] Danas K. and Ponte Castañeda P., Influence of the Lode parameter and the stress triaxiality on the failure of elasto-plastic porous materials. International Journal of Solids and Structures 79 (2012), 1325-1342.

[102] Gologanu M., Leblond J.B., Perrin G. and Devaux J., Theoretical models for void

coalescence in porous ductile solids. I. Coalescence “in layers, International Journal of Solids and Structures 38 (2001), 5581-5594.

[103] Gologanu M., Leblond J.B. and Devaux J., Theoretical models for void coalescence in porous ductile solids. II. Coalescence “in columns, International Journal of Solids and Structures 38 (2001), 5595-5604.

[104] Hutchinson J.W. and Neale K.W., Influence of strain-rate sensitivity on necking under uniaxial tension. Acta Metallurgica 25 (1977), 839-846.

[105] Hutchinson J.W. and Tvergaard V, Comment on ”Influence of the Lode parameter and the stress triaxiality on the failure of elasto-plastic porous materials” by K. Danas and P. Ponte Castañeda. International Journal of Solids and Structures 49 (2012), 3484-3485.

[106] Weibull W., A statistical distribution function of wide applicability. Journal of Applied Mechanics 18 (1951), 293-197.

[107] Reed R.C., Cox D.C. and Rae C.M.F., Damage accumulation during creep deformation of a single crystal superalloy at 1150 C. Materials Science and Engineering: A 448 (2007), 88-96.

[108] Chu C.C. and Needleman A., Void nucleation effects in biaxially stretched sheets. ASME Journal of Engineering Materials and Technology 102 (1980), 249-256.

[109] Pint B.A., DiStefano J.R. and Wright I.G., Oxidation resistance: One barrier to moving beyond Ni-base superalloys. Materials Science and Engineering: A 415 (2006), 255-263.

[110] Sarioglu C., Stinner C., Blachere J.R., Birks N., Pettit F.S. and Meier G.H., The control of sulfur content in nickel-base single crystal superalloys and its effect on cyclic oxidation resistance. Superalloys 1996, Edited by R. D. Kissinger, D. J. Deye, D. L. Anton, A. D. Cetel, M. V. Nathal, T. M. Pollock, and D. A. Woodford, The Minerals, Metals & Materials Society (1996), 71-80.

[111] MATLAB version 7.10.0., Natick, Massachusetts: The MathWorks Inc. (2010).

[112] Worswick M.J., Chen Z.T., Pilkey A.K., Lloyd D. and Court S., Damage characteri-

zation and damage percolation modelling in aluminum alloy sheet. Acta Materialia 49 (2001), 2791-2803.

[113] Mandelbrot B.B., Passoja D.E. and Paullay A.J., Fractal character of fracture surfaces of metals. Nature 308 (1984), 721-722.

[114] Bouchaud E., Lapasset G. and Planès J., Fractal dimension of fractured surfaces: A universal value? Europhys. Lett. 13 (1990), 73-79.

[115] Måløy K.J., Hansen A., Hinrichsen E.L. and Roux S., Experimental measurements of the roughness of brittle cracks. Phys. Rev. Lett. 68 (1992), 213-215.

[116] Bonamy D. and Bouchaud E., Failure of heterogeneous materials: a dynamic phase transition? Phys. Rep. 498 (2011), 1-44.

[117] Ponson L., Auradou H., Vié P. and Hulin J. P., Low self-affine exponents of fractured glass ceramics surfaces. Phys. Rev. Lett. 97 (2006), 125501.

[118] Bonamy D., Santucci S. and Ponson L., Crackling dynamics in material failure as the signature of a self-organized dynamic phase transition. Phys. Rev. Lett. 101 (2008), 045501.

[119] Schmittbuhl J., Roux S., Vilotte J.P. and Maloy K.J., Interfacial crack pinning: effect of nonlocal interactions. Phys. Rev. Lett. 74 (1955), 1787-1790.

[120] Koivisto J., Rosti J. and Alava M.J., Creep of a fracture line in paper peeling. Phys. Rev. Lett. 99 (2007), 145504.

[121] Demery V., Rosso A. and Ponson L., From microstructural features to effective toughness in disordered brittle solids. Condmat/arXiv:1212.1551 (2013).

[122] Rice J.R. and Johnson A., The Role of Large Crack Tip Geometry Changes in Plane Strain Fracture. Inelastic Behavior of Solids (eds. M. F. Kanninen, et al.), McGraw-Hill, N.Y. (1970), 641-672.

[123] Aravas N. and McMeeking R.M., Finite deformation analysis of crack-tip opening in elastic-plastic materials and implications for fracture. J. Mech. Phys. Solids 33 (1985), 25-49.

[124] Tvergaard V. and Hutchinson J., Two mechanisms of ductile fracture: void by void growth versus multiple void interaction. Int. J. Solids Struct. 39 (2002), 3581-3597.

[125] Afek I., Bouchbinder E., Katzav E., Mathiesen J. and Procaccia I., Void formation and roughening in slow fracture. Phys. Rev. E 71 (2005), 066127.

[126] Becker R., Needleman A., Suresh S., Tvergaard V. and Vasudevan A.K., An analysis of ductile failure by grain boundary void growth. Acta metall. 37 (1989), 99-120.

[127] Needleman A., Tvergaard V. and Bouchaud E., Prediction of ductile fracture surface roughness scaling. J. Appl. Mech. 79 (2012), 031015.

[128] Ponson L., Cao Y., Bouchaud E., Tvergaard V. and Needleman A., Statistics of ductile fracture surfaces: the effect of material parameters. Int. J. Fract., DOI 10.1007/s10704-013-9846-z.

[129] Tvergaard V. and Needleman A., Three dimensional microstructural effects on plain strain ductile crack growth. International Journal of Solids and Structures 43 (2006), 6165-6179.

[130] Pan J., Saje M. and Needleman A., Localization of deformation in rate sensitive porous plastic solids. International Journal of Fracture 21 (1983), 261-278.

[131] Gurson A.L., Plastic flow and fracture behavior of ductile materials incorporating void nucleation, growth and interaction. Ph.D. thesis, Brown University, Providence, RI (1975).

[132] Tvergaard V., Influence of voids on shear band instabilities under plane strain conditions. International Journal of Fracture 17 (1981), 389-407.

[133] Tvergaard V., On localization in ductile materials containing spherical voids. International Journal of Fracture 18 (1982), 237-252.

[134] Tvergaard V. and Needleman A., Analysis of the cup-cone fracture in a round tensile bar. Acta. Metall. 32 (1984), 157-169.

[135] Belytschko T., Chiapetta R.L. and Bartel H.D., Efficient large scale non-linear transient analysis by finite elements. Int. J. Numer. Methods Eng. 10 (1976), 579-596.

[136] Peirce D., Shih C.F. and Needleman A., A tangent modulus method for rate dependent solids. Comput. Struct., 18 (1984), 875-887.

[137] Tvergaard V., Influence of void nucleation on ductile shear fracture at a free surface. J. Mech. Phys. Solids 30 (1982), 399-425.

[138] Rice J., A path-independant integral and the approximate analysis of strain concentration by notches and cracks. J. Appl. Mech. 35 (1968), 379-386.

[139] Needleman A. and Tvergaard V., 1987. An analysis of ductile rupture modes at a crack tip. J. Mech. Phys. Solids, 35, 151-183.

[140] ASTM E1820-11, Standard Test Method for Measurement of Fracture Toughness, ASTM International (2011).

[141] Ponson L., Auradou H., Pessel M., Lazarus V. and Hulin J-P., Failure mechanisms and surface roughness statistics of fractured fontainebleau sandstone. Phys. Rev. E 76 ( 2007), 036108.

[142] Vernede S., Cao Y., Bouchaud J.P. and Ponson L., Extreme events and non-gaussian statistics of experimental fracture surfaces. (submitted for publication, 2013).

[143] Bonamy D., Ponson L., Prades S., Bouchaud E. and Guillot C., Scaling exponents for fracture surfaces in homogeneous glass and glassy ceramics. Phys. Rev. Lett. 97 (2006), 135504.

[144] Morel S., Bonamy D., Ponson L. and Bouchaud E., Transient damage spreading and anomalous scaling in mortar crack surfaces. Phys. Rev. E 78 (2008), 016112.

[145] Dalmas D., Lelarge A. and Vandembroucq D., Crack propagation through phase-separated glasses: Effect of the characteristic size of disorder. Phys. Rev. Lett. 101 (2008), 255501.

[146] Ramanathan S., Ertas D. and Fisher D.S., Quasistatic crack propagation in heterogeneous media. Phys. Rev. Lett. 79 (1997), 873-876.

[147] Ponson L., Bonamy D. and Bouchaud E., Two-dimensional scaling properties of experimental fracture surfaces. Phys. Rev. Lett. 96 (2006), 035506.